Dalitz Plot Analysis of the Charmless Threebody Decay $B^{\pm} \to K^{\pm}K^{\pm}K^{\mp}$ Utilising Data Recorded by the BABAR Experiment

Matthew Barrett

A thesis submitted for the degree of
Doctor of Philosophy

Particle Physics Group,
School of Physics and Astronomy,
University of Birmingham.

September 2006.

Abstract

The results from a Dalitz plot analysis of the charmless threebody decay $B^\pm \to K^\pm K^\pm K^\mp$ are presented. The analysis is carried out using data recorded with the *BABAR* detector. The data sample has an integrated luminosity of $210.6\,\mathrm{fb}^{-1}$, corresponding to 231.8 million $B\overline{B}$ pairs.

Branching fractions and CP asymmetries are presented for significant contributions to the mode $B^\pm \to K^\pm K^\pm K^\mp$. Modes found to be not significant, have an upper limit placed on their branching fraction.

No significant CP asymmetries are observed. The measured branching fractions and upper limits are:

$$
\begin{aligned}
\mathcal{B}(B^\pm \to K^\pm K^\pm K^\mp \text{ inclusive}) &= (35.1 \pm 1.3 \pm 2.1) \times 10^{-6}, \\
\mathcal{B}(B^\pm \to K^\pm K^\pm K^\mp \text{ non-resonant}) &= (18.6 \pm 3.4 \pm 1.8) \times 10^{-6}, \\
\mathcal{B}(B^\pm \to \phi(1020)K^\pm, \phi(1020) \to K^+ K^-) &= (4.3 \pm 0.6 \pm 0.3) \times 10^{-6}, \\
\mathcal{B}(B^\pm \to f_0(980)K^\pm, f_0(980) \to K^+ K^-) &= (8.7 \pm 3.1 \pm 1.4) \times 10^{-6}, \\
\mathcal{B}(B^\pm \to (KK)_0^0 K^\pm, (KK)_0^0 \to K^+ K^-) &= (3.3 \pm 1.1 \pm 0.7) \times 10^{-6}, \\
\mathcal{B}(B^\pm \to \chi_{c0}K^\pm, \chi_{c0} \to K^+ K^-) &< 2.9 \times 10^{-6}, \\
\mathcal{B}(B^\pm \to \phi(1680)K^\pm, \phi(1680) \to K^+ K^-) &< 1.5 \times 10^{-6}, \\
\mathcal{B}(B^\pm \to f_2(1270)K^\pm, f_2(1270) \to K^+ K^-) &< 1.1 \times 10^{-6}, \\
\mathcal{B}(B^\pm \to f_2'(1525)K^\pm, f_2'(1525) \to K^+ K^-) &< 2.4 \times 10^{-6}, \\
\mathcal{B}(B^\pm \to f_0(1710)K^\pm, f_0(1710) \to K^+ K^-) &< 3.3 \times 10^{-6}.
\end{aligned}
$$

Acknowledgements

I would like to thank...

PPARC and the University of Birmingham for allowing me to undertake the adventure that has been the last four years.

My supervisor, Chris Hawkes, for all his help over the course of my PhD, and for reading (and rereading) this thesis, through all its iterations. I also thank Alan Watson for his help and advice, and other members of the Birmingham *BABAR* group: Kelly, Sian, and Pablo.

Alistair Hart, with whom I carried out the analysis, for all his work, extensive knowledge of computing, and for his support through the whole of our time at Birmingham and SLAC.

Tamsin and Paul B, it seems a long time since Gleave road. You have both made the past four years memorable indeed.

Matt G and all the staff house physics crowd for many fine evenings of pool and informed debate.

Paul J and David H, who made sharing an office at SLAC a pleasure. Tom, Jim, Mitch, Will, and all the other UK *BABAR*ians who made my time in CA so enjoyable.

Pete, for your ongoing friendship through school days in Torquay, undergraduate years in Oxford, and onto postgraduate times.

The Birmingham Eagles for reminding me there is a world in Birmingham outside of physics.

Dave N for being the finest housemate/landlord anyone could wish for.

Declaration

I declare that no part of the work in this thesis has been previously presented at this, or any other, university to fulfil the requirements of a higher degree.

The data used in this analysis were recorded with the *BABAR* detector, by the *BABAR* collaboration, of which the author has been a member. The author has contributed to the collaboration by undertaking data taking shifts, and by being a member of the Data Quality Group, developing and maintaining monitoring software.

The selection of events described in chapter 4 uses standard tools available to the whole *BABAR* collaboration. More specific selection code was developed by members of the charmless threebody analysis working group.

The `Laura++` package was developed by Paul Harrison, John Back, Sian Morgan, and Tom Latham, with the author and Alistair Hart contributing to later development.

The Dalitz plot analysis was carried out by the Author and Alistair Hart. The optimisation of selection cuts (detailed in section 5.5.1) was carried out by John Back. The background determination (sections 5.5 and 5.6), study of multiple solutions (section 6.2), and fit bias study (section 6.6) were carried out by Alistair Hart. Study of Dalitz plot efficiency, self cross feed, and migration (sections 5.8 to 5.10), investigation of resolution effects (section 5.13), and the determination of the inclusive branching fraction (section 6.10) are the work of the author.

Contents

List of Tables

List of Figures

Chapter 1

Introduction

This chapter includes a brief overview of the Standard Model, and the particles that incorporate it, as an introduction to the theory of B mesons in chapter 2. An overview of the analysis described in this thesis concludes this short chapter.

1.1 The Standard Model

The study of the universe has uncovered increasingly smaller building blocks that make up the matter that is observed — the initial observation of the existence of the atom, was followed by the discovery of a much smaller nucleus, and then to the realisation that the nucleus itself was not fundamental, but composed of yet smaller particles called quarks, which thus far appear to be elementary. The other component of the atom, the electron also appears to be fundamental. It is one of a family of particles that share similar properties to the electron — the leptons. Together with these particles of matter, a number of forces have been discovered, which govern the interactions between these particles, holding them together, or pushing them apart.

The current best theory to explain the nature of these particles and forces is called the Standard Model (SM) of particle physics.

The matter particles — the quarks and the leptons — are found to obey Fermi–Dirac statistics, and are Fermions. The properties of the leptons are given in table 1.1;

Table 1.1: Properties of the leptons [1].

Particle Name	Particle Symbol	Spin ($\hbar$)	Charge (e)	Mass (MeV/c^2)	Antiparticle
electron	e^-	$\frac{1}{2}$	-1	0.511	e^+ (positron)
electron neutrino	ν_e	$\frac{1}{2}$	0	$< 3 \times 10^{-6}$	$\bar{\nu}_e$
muon	μ^-	$\frac{1}{2}$	-1	106	μ^+
muon neutrino	ν_μ	$\frac{1}{2}$	0	< 0.19	$\bar{\nu}_\mu$
tau	τ^-	$\frac{1}{2}$	-1	1780	τ^+
tau neutrino	ν_τ	$\frac{1}{2}$	0	< 18.2	$\bar{\nu}_\tau$

the values are taken from [1]. In addition to the six leptons there are also six antimatter equivalents of the leptons — the anti-leptons. Antimatter particles have identical masses to matter particles, but they have opposite charges and quantum numbers. The first antimatter particle to be discovered was the positron, the antimatter counterpart of the electron.

Like the leptons, quarks have been discovered with six distinct types or flavours. The properties of the quarks are given in table 1.2. For each quark there is also a corresponding antiquark. The antiquarks are denoted with a bar over the equivalent quark's symbol, e.g. u and $\bar{u}$. The most important difference between the quarks and the leptons is that the leptons are unaffected by the strong nuclear force, whereas the quarks do interact via this force. In addition to an electrical charge, quarks have a strong "colour" charge, which is analogous to the electrical charge, except, that there are three charge states (usually called red(r), green(g), and blue(b)), as opposed to one. Antiquarks carry anticolour charges; anti-red($\bar{r}$), anti-green($\bar{g}$) and anti-blue($\bar{b}$). These are occasionally referred to as cyan, magenta, and yellow.

No observations of free quarks have been made [2], and thus it is conjectured that quarks can only exist in bound states. Because of this, measurement of the properties of individual quarks, such as the mass, is difficult and subject to large uncertainties.

Quarks can only exist in colour neutral composite states. These are states where

Table 1.2: Properties of the quarks [1].

Particle Name	Particle Symbol	Spin ($\hbar$)	Charge (e)	Mass (GeV/c^2)
Down	d	$\frac{1}{2}$	$-\frac{1}{3}$	0.004 to 0.008
Up	u	$\frac{1}{2}$	$+\frac{2}{3}$	0.0015 to 0.004
Strange	s	$\frac{1}{2}$	$-\frac{1}{3}$	0.080 to 0.130
Charm	c	$\frac{1}{2}$	$+\frac{2}{3}$	1.150 to 1.350
Bottom	b	$\frac{1}{2}$	$-\frac{1}{3}$	4.100 to 4.400
Top	t	$\frac{1}{2}$	$+\frac{2}{3}$	$178.1^{+10.4}_{-8.3}$

either three quarks of different colours are bound together (rgb), such particles are called baryons, or there are particles consisting of quarks and antiquarks, where the colour and anticolour cancel out, e.g. ($r\bar{r}$), such particles are called mesons — details of mesons that contain a b quark are given in section 2.2.1. The third type of conglomeration is the anti-baryon, made of three anti-quarks.

The forces of nature are found to act as just a handful of fundamental forces — Electromagnetism, Gravity, the Weak Nuclear Force, and the Strong Nuclear Force. At high energies the Weak and the Electromagnetic forces act as a single force — the Electroweak force. It is possible that all four forces are just low energy manifestations of a single unified force, that is only evident at energies much higher than those that can currently be studied. Forces in the Standard Model are mediated by the (virtual) particles known as Bosons (they obey Bose–Einstein statistics). The properties of the force carrying bosons are given in Table 1.3.

The electromagnetic force is mediated by the photon, whereas the weak force is mediated by three particles, the W^+, W^-, and Z^0. There are eight types of gluon which govern the strong force; like quarks the gluons carry colour charge, and the eight distinct gluons each have differing combinations of colour/anticolour. The boson that transmits the force of gravity has been named the Graviton, but has as yet not been discovered.

3

Table 1.3: Properties of bosons [1]. The Higgs boson and Graviton have not (yet) been discovered, and thus there are no measurements of their properties — the values in parentheses are Standard Model predictions.

Particle Name	Particle Symbol	Spin ($\hbar$)	Charge (e)	Mass (GeV/c^2)
Photon	γ	1	0	$< 6 \times 10^{-26}$
Gluon	g	1	0	0 (predicted)
W	$W^{\pm}$	1	± 1	80.425 ± 0.038
Z	Z^0	1	0	91.188 ± 0.002
Higgs	$H^0, H^{\pm}$?	(0)	$(0, \pm 1)$	?
Graviton	G	(2)	(0)	?

In addition to these forces, there remains a phenomenon that does not fit naturally into this scheme of particle/force field interactions, that being that the particles have masses, whereas the theory only works for massless particles. The Higgs mechanism [3] is suggested to be the answer to this quandary. It proposes spontaneous symmetry breaking, together with a coupling to a new boson, the Higgs boson, which would couple more strongly to the particles observed with the highest masses. The Higgs boson has not yet been discovered, but searches using future experiments should reveal whether this particle does exist, and if so what properties it has.

There is another important observation about the nature of the universe which should also be discussed. This relates to the baryon asymmetry of the universe. Following the Big Bang, equal quantities of matter and antimatter should have been created from the energy of the fireball. As the universe cooled this matter and antimatter should have annihilated back to energy, leaving the universe rich with energy, but depopulated of (anti-)matter. However, the universe today shows an excess of matter, and no evidence for antimatter being present on macroscopic scales. As most of the visible matter in the universe is made up of baryons, there must have been some mechanism in the early universe that allowed this baryon asymmetry to develop.

Three conditions for this to occur were proposed by Andrei Dmitrievich Sakharov [4]. These conditions are:

- Baryon number non-conservation;

- CP-violation occurs;

- Universal departure from thermodynamic equilibrium.

The second of these criteria, that of CP-violation is discussed in greater detail in section 2.3. It can be noted however that the amount of CP-violation that is measured in the SM is insufficient to account for the observed universe [5]. This could imply that the current understanding of CP-violation is incomplete, and that there are sources of CP-violation that exist in new physics, beyond the Standard Model. Evidence of neutrino masses could suggest that CP-violation occurs in the lepton sector, which could account for part of the discrepancy.

The standard model is a very involved and complex set of theories, built up over many decades of research in the field of particle physics by worldwide collaborations of scientists, and as such the full details of the Standard Model are well beyond the scope of this document.

1.2 Overview of this Thesis

This thesis covers the analysis of the decay of a charged B meson into three charged kaons. This section serves to outline how the content of the thesis is presented in each of the chapters.

Chapter 2 of this thesis covers theoretical concepts associated with the analysis. The physics of B mesons is first shown, the combined symmetry CP is formally defined, and its manifestations in the study of B meson decays are noted. The CKM matrix is the mechanism by which CP violation is introduced into the Standard Model, and its assumed unitary nature leads to The Unitarity Triangle, measuring the parameters of

which is a major goal of B physics. Current measurements and constraints of Unitarity Triangle parameters are reported.

The motivation behind the study of the mode $B^{\pm} \to K^{\pm}K^{\pm}K^{\mp}$ is highlighted, and some processes contributing to this interaction are shown. The analysis is carried out using the Dalitz plot technique. This technique allows for the determination of any intermediate stages in the decay, due to the presence of short lived or "resonance" particles, such as the $\phi(1020)$, which would appear in the B meson decay as $B^{\pm} \to \phi(1020)K^{\pm}$, $\phi(1020) \to K^+K^-$.

Chapter 3 showcases the *BABAR* detector, and the PEP-II storage ring. The detector consists of a number of subdetectors, each of which has its own objectives. The detector triggering and data acquisition systems are also covered.

Chapter 4 covers the reconstruction of tracks and energy clusters, and the identification of particles. The criteria that are applied to data taken from the detector in order to produce data that can be used in this analysis are reported.

Chapter 5 details the analysis method itself. It covers the modelling of reconstruction efficiency across the Dalitz plot, the determination of expertimental backgrounds, from both continuum (light quark) production, and from decays of B mesons to states other than three charged kaons. Fitting the events that populate the Dalitz plot is described, together with factors that affect the fitting such as multiple solutions. A study attempting to model detector resolution effects within the fit is documented.

Chapter 6 details the results of the analysis. A model for the resonances that contribute to decay $B^{\pm} \to K^{\pm}K^{\pm}K^{\mp}$ is determined, and consists of:

- $\phi(1020)$,

- χ_{c0},

- $f_0(980)$,

- $(KK)_0^0$, a resonant structure with a mass of $\sim 1.5\,\mathrm{GeV}/c^2$,

- $\phi(1680)$,

- Non-resonant $B^\pm \to K^\pm K^\pm K^\mp$.

Other resonances, such as $f_2'(1525)$, and $f_0(1710)$ are also considered, and found not to be significant contributions. The fit is carried out separately for events arising from the decay of a B^+, and of a B^-. The total branching fraction for $B^\pm \to K^\pm K^\pm K^\mp$ is calculated. For each of the significant resonances a branching fraction and CP asymmetry are calculated. For less significant resonances a branching fraction upper limit is calculated.

Chapter 7 summarises the results and reviews them, with a comparison with other analyses of $B^\pm \to K^\pm K^\pm K^\mp$ that have been carried out. The thesis is concluded by a discussion of what has been achieved in this analysis, and what could potentially be achieved in a future analysis of $B^\pm \to K^\pm K^\pm K^\mp$.

Chapter 2

Theory

2.1 The Symmetries C, P and T

The development of physics has been aided by the realisation of the presence of certain symmetries in nature. The presence of a symmetry also implies the presence of a conserved quantity within a system. Two important symmetries in particle physics are those of parity (P) and charge conjugation (C). The effect of the operation of parity on a wavefunction is to reverse the spatial co-ordinates $\underline{r} \to -\underline{r}$. Momentum is also reversed $\underline{p} \to -\underline{p}$, while angular momentum, which is an axial-vector ($\underline{L} = \underline{r} \times \underline{p}$) is unchanged by the operation. Thus the intrinsic angular momentum of a particle, its spin, $\underline{\sigma}$, is unchanged under parity, but the particle's helicity ($\lambda = \underline{\sigma}.\underline{p}/|\underline{p}|$) will change sign. Since a repeated application of parity yields the initial state, parity can only take the eigenvalues $\eta_P = \pm 1$.

$$P|f(\underline{p})\rangle = \eta_P|f(-\underline{p})\rangle. \tag{2.1}$$

Charge conjugation acts on a wavefunction by interchanging particles with antiparticles, whilst leaving their physical properties such as momentum unchanged. Like parity, states which are eigenstates of charge conjugation can only take eigenvalues $\eta_c = \pm 1$. Because the operation of charge conjugation changes the particles involved only particles, or particle combinations, which have zero overall charge can

8

be eigenstates of C.

$$C|f(\underline{p})\rangle = \eta_C|\overline{f}(\underline{p})\rangle. \tag{2.2}$$

Parity was thought to be always conserved, and is observed to be conserved in strong and electromagnetic interactions. However observations made on the decays of Cobalt-60 nuclei in 1956/7 showed that parity was not conserved in weak interactions [6], and is in fact maximally violated.

It was then supposed that the combined operation CP was conserved in these decays.

$$CP|f(\underline{p})\rangle = \eta_{CP}|\overline{f}(-\underline{p})\rangle. \tag{2.3}$$

States which have an eigenvalue of CP of $+1$ are referred to as CP-even, and states with an eigenvalue of CP of -1 are referred to as CP-odd.

There is a third symmetry, that of time reversal T, which transforms $t \to -t$.

$$T|f(\underline{p})\rangle = \eta_T|f(-\underline{p})\rangle^*. \tag{2.4}$$

One of the predictions of quantum field theories is that the combined symmetry CPT is always conserved [7], thus if CP is violated, then T must also be violated, such that the overall CPT symmetry is preserved. Searches have been conducted to see whether CPT is violated, such as trying to find a difference between the masses of particles and their antiparticles, but no evidence of such has been found.

In 1964 the phenomenon of CP violation was observed in the decays of neutral kaons [8], and has since been observed in the decays of B mesons [9].

2.2 B Meson Physics

2.2.1 B mesons

The primary goal of the *BABAR* experiment is to study the properties of B mesons. There are eight distinct meson states that can be formed containing unique combinations of a b quark or $\overline{b}$ antiquark and a lighter (anti)quark. These are detailed in

Table 2.1: Complete family of weakly decaying B mesons. Higher B^* mesons omitted.

Particle	Quark content	Charge (e)	Mass (GeV/c^2)	Studied at $BABAR$
B^0	$\bar{b}d$	0	5.279	Yes
$\overline{B}^0$	$b\bar{d}$	0	5.279	Yes
B^+	$\bar{b}u$	+1	5.279	Yes
B^-	$b\bar{u}$	−1	5.279	Yes
B_s^0	$\bar{b}s$	0	5.370	No
$\overline{B}_s^0$	$b\bar{s}$	0	5.370	No
B_c^+	$\bar{b}c$	+1	6.4	No
B_c^-	$b\bar{c}$	−1	6.4	No

table 2.1. In addition, there are further excited states of B mesons, usually labelled B^*, that exist at higher energies(masses) but with identical quark content.

Those combinations that contain an s or c (anti)quark are too heavy to be produced at the operational beam energy used during the running of the $BABAR$ experiment. Thus only the combinations involving the two lightest quarks can be studied.

It should also be noted that the neutral particles listed here are the flavour eigenstates of the strong Hamiltonian. The weak/mass eigenstates are not the same, and will be discussed in the next section.

2.2.2 Mixing of Neutral B mesons

The phenomenon of mixing in neutral mesons was first observed in the decays of neutral kaons. These are created in strong interactions in two varieties — K^0 and $\overline{K}^0$. However they decay via the weak interaction as either K_S^0 or K_L^0, which have quite different lifetimes and preferentially decay via different modes. As the K^0 and $\overline{K}^0$ contain $\bar{s}$ and s quarks respectively they react differently when interacting with normal (baryonic) matter. For example when colliding a π beam with a stationary target, the threshold beam energy is lower for creating a K^0, than for creating a $\overline{K}^0$
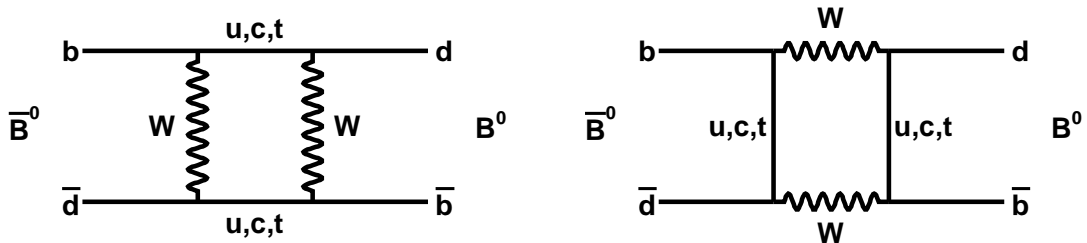
Figure 2.1: Oscillations between B^0 and $\overline{B}^0$ (and vice versa) mesons via box diagrams.

(due to the fact that strangeness -1 baryons can be created, but not strangeness $+1$). Thus it is possible to create a pure beam of K^0. However studying this beam at a later time reveals it to contain components of both $\overline{K}^0$ and K^0. Thus some of the neutral kaons have oscillated from one form into another during transit.

Such a phenomenon has not been observed with neutral D mesons, and the effect is predicted to be small.

The mixing for neutral B mesons is a measurable effect. Oscillations are possible for both B^0 and B^0_s mesons and each will have a different oscillation frequency. Only B^0 mesons are studied at BABAR, so only oscillations of these particles are discussed.

The mixing of neutral B mesons takes place via box diagrams. Two possible orientations of the box diagram are shown in figure 2.1. The box diagrams consist of two sides which have the propagation of a virtual W boson, and two sides which consist of one of the charge $+\frac{2}{3}e$ virtual u-type quarks. The two box diagrams shown correspond to either the W bosons or the u-type quarks being exchanged, between the b and d (anti)quarks. The total matrix element for this process has contributions from both diagrams, and also from all three of the u-type quarks. However, calculation leads to the amplitude of each contribution being proportional to the mass of the u-type quark, and thus the overall rate is dominated by the contribution of the t quark

11

boxes.

The B^0 and $\overline{B}^0$ mesons shown in the box diagrams are flavour eigenstates. However, when a B meson decays it is via a weak interaction, and the mass eigenstates need to be considered. It can be supposed that the mass eigenstates are linear combinations of the flavour eigenstates.

Taking a general particle state, that can be expressed as a superposition of two neutral B states, i.e.

$$|\Psi\rangle = \alpha|B^0\rangle + \beta|\overline{B}^0\rangle, \tag{2.5}$$

then the behaviour of this state is governed by the Schrödinger equation in its time dependent form:

$$i\frac{\partial}{\partial t}\Psi = H\Psi, \tag{2.6}$$

and the Hamiltonian, H, is given by:

$$H = M - i\frac{\Gamma}{2}, \tag{2.7}$$

where H is a 2×2 Hermitian matrix, as are M and Γ. The property of CPT invariance will ensure that $H_{11} = H_{22}$, and if CP invariance is assumed (the consequences of CP non-invariance in mixing processes are described in section 2.3.3) then $H_{12} = H_{21}$. The solution of the Schrödinger equation is then specified by two coupled modes, which can be expressed in terms of:

$$|\Psi_1\rangle = \sqrt{\frac{1}{2}}(|B^0\rangle + |\overline{B}^0\rangle), \tag{2.8}$$

$$|\Psi_2\rangle = \sqrt{\frac{1}{2}}(|B^0\rangle - |\overline{B}^0\rangle). \tag{2.9}$$

These states are in fact eigenstates of the CP operator:

$$CP|\Psi_1\rangle = +1|\Psi_1\rangle, \tag{2.10}$$

$$CP|\Psi_2\rangle = -1|\Psi_2\rangle. \tag{2.11}$$

The coupled equations are then:

$$i\frac{\partial}{\partial t}\Psi_{1,2} = M_{1,2}|\Psi_{1,2}\rangle - i\frac{\Gamma_{1,2}}{2}|\Psi_{1,2}\rangle, \tag{2.12}$$

to which the general solution can be written as:

$$|\Psi_{1,2}(t)\rangle = |\Psi_{1,2}(0)\rangle e^{-iM_{1,2}t}e^{-\Gamma_{1,2}t/2}, \qquad (2.13)$$

where the terms for mass, M, and width, Γ, are as follows:

$$M_{1,2} = Re(H_{11} \pm H_{21}), \qquad (2.14)$$

$$\Gamma_{1,2}/2 = Im(H_{11} \pm H_{21}). \qquad (2.15)$$

A state which is created initially to consist purely of B^0 mesons, would at some later time be a mixture of both B^0 and $\overline{B}^0$ mesons. The differences in masses and widths of the two states can be defined as:

$$\Delta m = |M_1 - M_2| \qquad (2.16)$$

$$\Delta\Gamma = |\Gamma_1 - \Gamma_2| \qquad (2.17)$$

Since the two states have different masses but similar widths, it is common to use a mass comparative naming scheme, thus $|\Psi_2\rangle \approx |B_H\rangle$ and $|\Psi_1\rangle \approx |B_L\rangle$, where the H and the L stand for Heavy and Light, and by definition $m_{B_H} > m_{B_L}$. The approximation symbol is used here because the treatment of the states $\Psi_{1,2}$ does not take into account any CP Violation in the mixing.

2.3 CP-Violation

2.3.1 CP Violation in B Meson Decays

There are three methods by which CP violation can manifest itself in the B meson sector. All three can be observed (at least in theory) in the behaviour of neutral B mesons, but only direct CP violation can occur in the decays of charge carrying mesons.

The three types are:

- Direct CP violation;

- CP violation in mixing;

- CP violation in interference between decay and mixing.

Decay amplitudes for the decay of an arbitrary B meson, or its CP conjugate $\bar{B}$, to final state f or $\bar{f}$, which are arbitrary CP eigenstates, can be defined as follows:

$$A_f = \langle f|H|B\rangle, \tag{2.18}$$

$$\bar{A}_f = \langle f|H|\bar{B}\rangle, \tag{2.19}$$

$$A_{\bar{f}} = \langle \bar{f}|H|B\rangle, \tag{2.20}$$

$$\bar{A}_{\bar{f}} = \langle \bar{f}|H|\bar{B}\rangle. \tag{2.21}$$

The states B_H and B_L, first introduced in section 2.2.2, can be described by an arbitrary superposition of B^0 and $\bar{B}^0$ mesons, thus:

$$|B_H\rangle = p|B^0\rangle - q|\overline{B}^0\rangle, \tag{2.22}$$

$$|B_L\rangle = p|B^0\rangle + q|\overline{B}^0\rangle, \tag{2.23}$$

where p and q are subject to the normalisation condition $|p|^2 + |q|^2 = 1$.

2.3.2 Direct CP Violation

Direct CP violation takes the form of a difference in the branching fraction of a B meson to a final state f, compared to the charge conjugate decay, that of a $\bar{B}$ to the final state $\bar{f}$. (The state f should not be accessible to decays of the $\bar{B}$, and the state $\bar{f}$ should likewise not be accessible to decays of the B if direct CP violation is the only one of the three to occur).

Therefore the definition of direct CP violation is:

$$\left|\frac{\bar{A}_{\bar{f}}}{A_f}\right| \neq 1. \tag{2.24}$$

Because the CP violation is only related to the decay of the B mesons, direct CP violation is also known as CP violation in the decay. As stated previously direct CP

violation can occur for both charged and neutral B mesons, and it is the only type that can occur for charged B mesons, as the other two types of CP violation require that the meson be capable of oscillation between different flavour eigenstates.

The amount of direct CP violation in a particular decay channel can be parametrised as:

$$A_{CP} = \frac{\Gamma(\bar{B} \to \bar{f}) - \Gamma(B \to f)}{\Gamma(\bar{B} \to \bar{f}) + \Gamma(B \to f)}. \tag{2.25}$$

2.3.3 CP Violation in Mixing

In section 2.2.2 the discussion of mixing assumed that the matrix H had the property that $H_{21} = H_{12}$, and that the superposition states given in equations (2.8) and (2.9) contained equal contributions from B^0 and $\bar{B}^0$. In general this is not the case, and the consequence is CP violation during the mixing of the neutral B mesons.

From equations (2.6) and (2.7), and equations (2.22) and (2.23):

$$\frac{|q|^2}{|p|^2} = \frac{|M_{12}^* - \frac{i}{2}\Gamma_{12}^*|}{|M_{12} - \frac{i}{2}\Gamma_{12}|}. \tag{2.26}$$

Since CP conservation requires that $M_{12} = M_{12}^*$ and that $\Gamma_{12} = \Gamma_{12}^*$, then it can be seen that a condition for CP violation to occur is:

$$\left|\frac{q}{p}\right| \neq 1. \tag{2.27}$$

Sometimes this type of CP violation is called *indirect CP* violation.

2.3.4 CP Violation in the Interference between Decays and Mixing

This final type of CP violation can occur only in decays of neutral mesons, where both the state B, and its conjugate $\bar{B}$, can decay to the same final state f. Then there are two decay paths by which a particle B could decay to that final state:

- Directly: $B \to f$

- Indirectly: $B \to \bar{B} \to f$

The quantity λ is defined such that:

$$\lambda = \frac{q}{p} \frac{\bar{A}_f}{A_f}. \tag{2.28}$$

The parameter λ has a physically significant phase that is independent of any particular chosen phase convention. If $\lambda \neq \pm 1$ then CP violation is observed. The conditions for direct and indirect CP violation are enough to ensure that λ can be different from unity. However, if CP violation has occurred in the interference between the decay path without mixing, and the decay path with mixing, then:

$$Im(\lambda) \neq 0. \tag{2.29}$$

If $|q/p| = 1$, and $\Delta\Gamma = 0$, which is a good approximation in B decays, then A_{CP} can be written in a useful way:

$$A_{CP} = \frac{2Im\lambda}{1 + |\lambda|^2} \sin(\Delta mt) - \frac{1 - |\lambda|^2}{1 + |\lambda|^2} \cos(\Delta mt), \tag{2.30}$$

or

$$A_{CP} = S_{CP} \sin(\Delta mt) - C_{CP} \cos(\Delta mt). \tag{2.31}$$

S_{CP} and C_{CP} are very commonly quoted parameters in CP violation measurements in neutral B decays.

2.3.5 The CKM matrix

The flavour eigenstates of the quarks — those involved in strong and electromagnetic decays — are not the same as the weak eigenstates, which are involved in weak decays, the only decays that can change the flavour of the quarks. In the simplified case of four quark flavours the relationship between the flavour eigenstates and weak eigenstates, can be represented by the Cabibbo matrix:

$$\begin{pmatrix} d' \\ s' \end{pmatrix} = \begin{pmatrix} \cos\theta_c & \sin\theta_c \\ -\sin\theta_c & \cos\theta_c \end{pmatrix} \begin{pmatrix} d \\ s \end{pmatrix}. \tag{2.32}$$

16

In this case the mixing between the states is defined by a single parameter — the Cabibbo angle θ_c [10]. The fact that the mixing is described to occur between the d and s quarks rather than the u and c quarks is an arbitrary choice, and purely a matter of convention.

The two-generation case was extended to three generations by Kobayashi and Maskawa [11], and is described by the Cabibbo-Kobayashi-Maskawa (CKM) matrix:

$$
\begin{pmatrix} d' \\ s' \\ b' \end{pmatrix} = \begin{pmatrix} V_{ud} & V_{us} & V_{ub} \\ V_{cd} & V_{cs} & V_{cb} \\ V_{td} & V_{ts} & V_{tb} \end{pmatrix} \begin{pmatrix} d \\ s \\ b \end{pmatrix}.
\tag{2.33}
$$

In general a matrix with n rows and n columns will possess $n(n-1)/2$ real parameters, and $(n-1)(n-2)/2$ phase parameters. So a 3×3 matrix will have $3+1$ parameters, whereas a 2×2 matrix will have just 1 $(1+0)$ parameter. The CKM matrix indeed has four free parameters, rather than just one (θ_c) for the Cabibbo matrix, and these can vary, depending on which representation is chosen.

The CKM matrix can be parametrised in a number of ways. The parametrisation favoured by the PDG is [12]:

$$
\begin{aligned}
V &= \begin{pmatrix} 1 & 0 & 0 \\ 0 & c_{23} & s_{23} \\ 0 & -s_{23} & c_{23} \end{pmatrix} \begin{pmatrix} c_{13} & 0 & s_{13}e^{-i\delta_{13}} \\ 0 & 1 & 0 \\ -s_{13}e^{i\delta_{13}} & 0 & c_{13} \end{pmatrix} \begin{pmatrix} c_{12} & s_{12} & 0 \\ -s_{12} & c_{12} & 0 \\ 0 & 0 & 1 \end{pmatrix} \\
&= \begin{pmatrix} c_{12}c_{13} & s_{12}c_{13} & s_{13}e^{-i\delta_{13}} \\ -s_{12}c_{23} - c_{12}s_{23}s_{13}e^{i\delta_{13}} & c_{12}c_{23} - s_{12}s_{23}s_{13}e^{i\delta_{13}} & s_{23}c_{13} \\ s_{12}s_{23} - c_{12}c_{23}s_{13}e^{i\delta_{13}} & -c_{12}s_{23} - s_{12}c_{23}s_{13}e^{i\delta_{13}} & c_{23}c_{13} \end{pmatrix}.
\end{aligned}
\tag{2.34}
$$

where the shorthand notations $c_{ij} = \cos\theta_{ij}$ and $s_{ij} = \sin\theta_{ij}$ are used. The angles are θ_{13}, θ_{12}, and θ_{23} which describe the couplings between two different generations of quarks, and the phase δ_{13}. This parametrisation is favoured, since for the case where the third generation is decoupled, i.e. $\theta_{13} = 0$ and $\theta_{23} = 0$, the matrix simply becomes the Cabbibo matrix, as given in equation (2.32).

A parametrisation of the CKM matrix that is particularly used in B physics is that

17

first suggested by Wolfenstein [13]. This parametrisation is chosen to emphasise the hierarchy of terms within the matrix.

The Wolfenstein parametrisation is as follows:

$$V = \begin{pmatrix} 1 - \lambda^2/2 & \lambda & A\lambda^3(\rho - i\eta) \\ -\lambda & 1 - \lambda^2/2 & A\lambda^2 \\ A\lambda^3(1 - \rho - i\eta) & -A\lambda^2 & 1 \end{pmatrix} + \mathcal{O}(\lambda^4). \qquad (2.35)$$

It expands the terms of the CKM matrix in terms of the parameter λ (a different parameter to that used in equation (2.28)), which is equal to the magnitude of V_{us}, or alternatively $\lambda = \sin(\theta_c) = 0.22$. The parameters A, ρ, and η are all real numbers, that were each intended to be of order one. As λ is small, the diagonal elements of the matrix are all of order unity.

Current values from the Particle Data Group [14] give the magnitudes of the CKM matrix elements as:

$$V_{CKM} = \begin{pmatrix} 0.9739 \to 0.9751 & 0.221 \to 0.227 & 0.0029 \to 0.0045 \\ 0.221 \to 0.227 & 0.9730 \to 0.9744 & 0.039 \to 0.044 \\ 0.0048 \to 0.014 & 0.037 \to 0.043 & 0.9990 \to 0.9992 \end{pmatrix}. \qquad (2.36)$$

These values are calculated based on only tree-level contributions (see section 2.5), and are quoted at the 90% confidence level.

2.3.6 The Unitarity Triangle

The CKM matrix should be unitary, and by enforcing the unitarity condition, certain constraints are forced onto the elements V_{ij} of the matrix. Taking products of different rows and columns in the unitarity condition equation $V^\dagger V = I$ (where I is the identity matrix), gives nine relations among the elements of the matrix, of the form:

$$V_{ud}V_{us}^* + V_{cd}V_{cs}^* + V_{td}V_{ts}^* = 0 \qquad (2.37)$$

18

or

$$V_{ud}V_{ud}^* + V_{us}V_{us}^* + V_{ub}V_{ub}^* = 1. \tag{2.38}$$

Six of these contain three complex numbers summing to zero and can hence be represented as triangles in the complex plane. Most of the triangles that can be formed are very narrow, involving angles close to $180°$ and $0°$. However:

$$V_{ud}V_{ub}^* + V_{cd}V_{cb}^* + V_{td}V_{tb}^* = 0 \tag{2.39}$$

is predicted to have sides of the same order magnitude. This can be demonstrated by expanding the equation in terms of λ from the Wolfenstein parametrisation given in equation (2.35). This equation is very important in B physics. When plotting this equation as the sum of three numbers in the complex plane, the resulting triangle formed is known as The Unitarity Triangle — this is shown in figure 2.2

It is common to plot The Unitarity Triange in the $\bar{\rho} - \bar{\eta}$ plane, where $\bar{\rho}$ and $\bar{\eta}$ are defined as:

$$\begin{aligned} \bar{\rho} &= \rho(1 - \lambda^2/2), \\ \bar{\eta} &= \eta(1 - \lambda^2/2), \end{aligned} \tag{2.40}$$

and to normalise the length of the bottom edge of the triangle to 1, by dividing all the sides, by the length of this side. The apex of The Unitarity Triangle is given by $(\bar{\rho}, \bar{\eta})$

There are five properties of the triangle that are of interest, the lengths of the two other sides, and the angles. With the bottom side defined as 1, then the remaining two sides are given by the ratios:

$$\frac{V_{ud}V_{ub}^*}{|V_{cd}V_{cb}^*|}, \quad \frac{V_{td}V_{tb}^*}{|V_{cd}V_{cb}^*|}. \tag{2.41}$$

The three angles are conventionally given the names α, β, and γ, and are defined as follows:

$$\alpha \equiv \arg\left[-\frac{V_{td}V_{tb}^*}{V_{ud}V_{ub}^*}\right], \tag{2.42}$$

$$\beta \equiv \arg\left[-\frac{V_{cd}V_{cb}^*}{V_{td}V_{tb}^*}\right], \tag{2.43}$$

$$\gamma \equiv \arg\left[-\frac{V_{ud}V_{ub}^*}{V_{cd}V_{cb}^*}\right]. \tag{2.44}$$

19
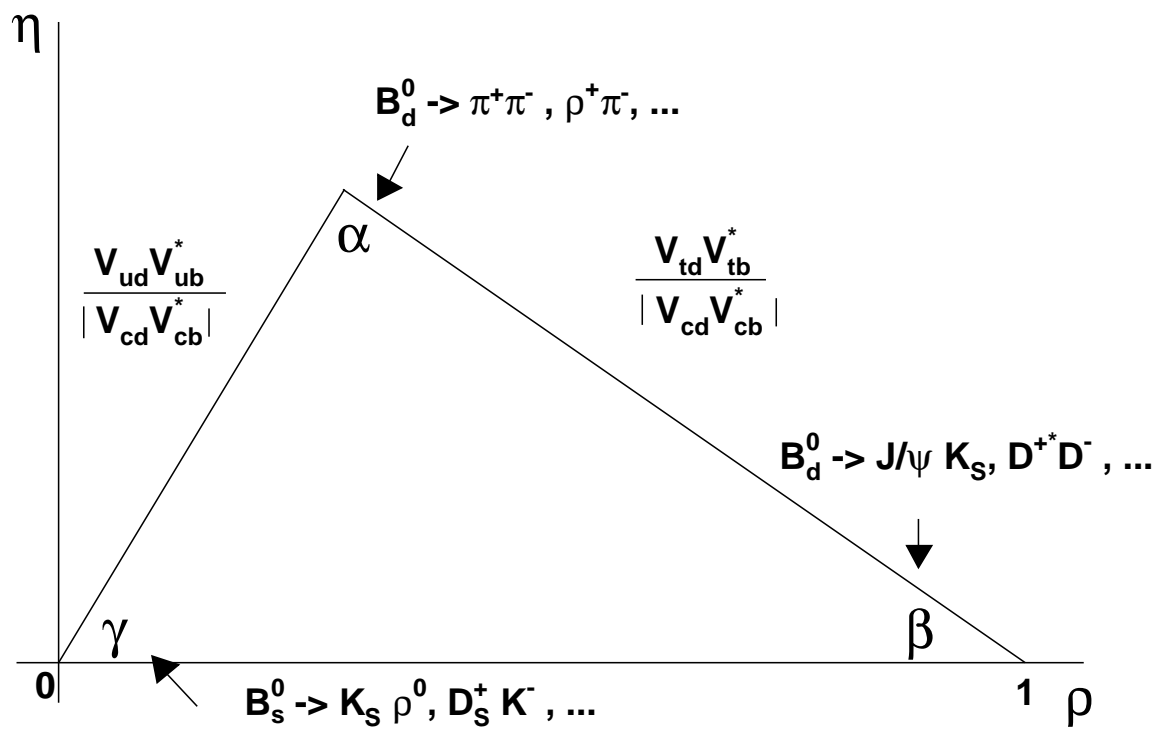
Figure 2.2: The Unitarity Triangle. Some of the decay modes which can be used to determine α, β, and γ are listed by each of the angles.

Many decay modes are sensitive to one of the angles of The Unitarity Triangle, such as the decay $B^0 \rightarrow J/\psi K_S^0$, which is used to measure β. Analyses of these modes cannot unambiguously measure the value of the angles, but instead measure such quantities as $\sin 2\beta$, or $\sin 2\alpha$, *etc.* It is only when combining such measurements with other constraints that the angles themselves can be established.

It is important to note that the CKM matrix, and hence The Unitarity Triangle, only describes Standard Model physics. Thus if the sides and angles of the Unitarity Triangle are all measured and do not form a triangle then this is a sign of physics beyond the Standard Model.

2.3.7 Current constraints on the Unitarity Triangle

The CKMfitter group [15] has produced a software package that performs a combined fit to results relating to measurements of CKM matrix parameters. They produce plots showing the current world-best constraints on the parameters, which are updated following major conferences. The plots in the $\bar{\rho} - \bar{\eta}$ plane demonstrate how well experimental measurements agree with each other and with the expectations of the unitarity triangle. The results given in this section are those updated following the FPCP 06 conference, held in Vancouver, Canada.

The Unitarity Triangle in the $\bar{\rho} - \bar{\eta}$ plane together with these constraints is shown in figure 2.3. Figure 2.4 shows the same information as the previous figure, but focuses on the area immediately surrounding the Unitarity triangle, and allows for more detailed inspection of the permitted region of the vertex at which the angle α lies.

The inputs to the fit are a series of measurements, and parameters associated with the CKM matrix are extracted. The chosen inputs and results are periodically updated, and the following values are taken from the latest online version.

Firstly the bounds on some of the input parameters are shown in the diagrams:

- The oscillation frequency for B^0 mesons: $\Delta m_d = 0.502 \pm 0.006 \text{ps}^{-1}$ — this constraint is shown as a yellow annulus.

21
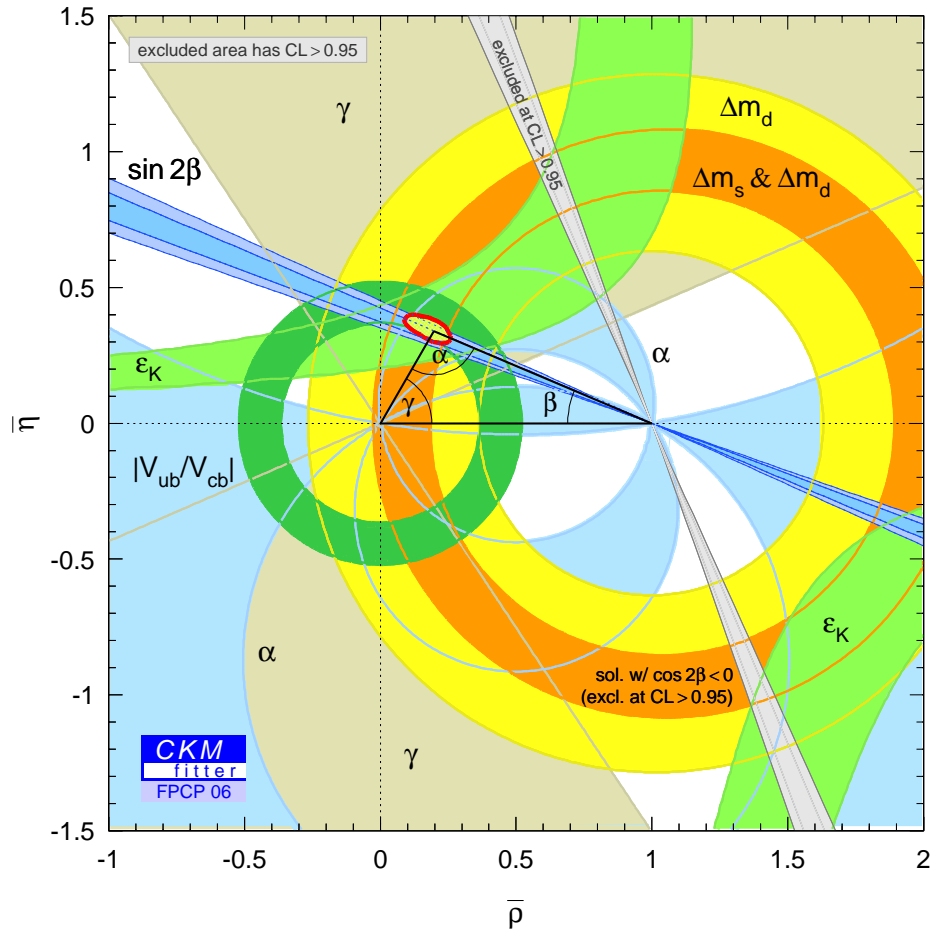
Figure 2.3: Constraints on The Unitarity Triangle produced by the CKMfitter group [16].
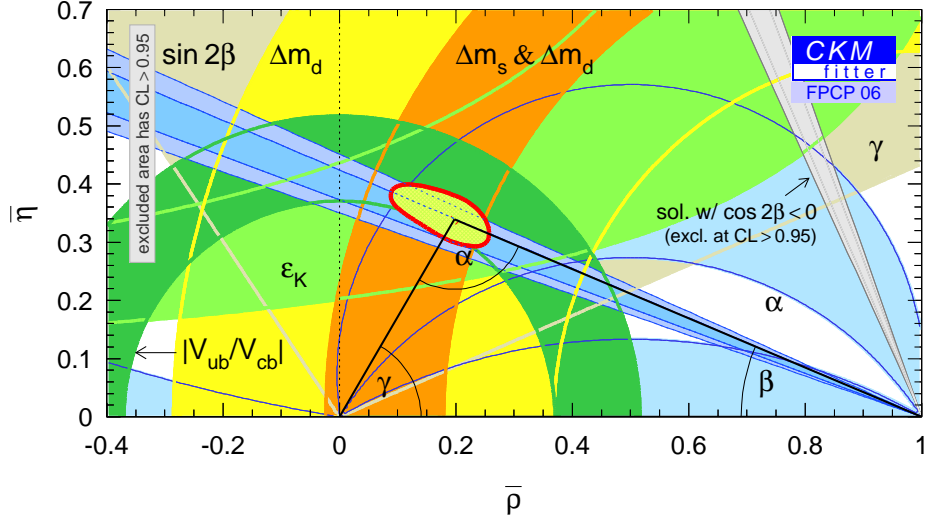
Figure 2.4: Constraints on The Unitarity Triangle, focusing on the α vertex in the $\bar{\rho} - \bar{\eta}$ plane [17].

- The oscillation frequency for B_s^0 mesons: Δm_s: The input for this parameter uses the amplitude spectrum and CDF experiments likelihood fit. A measured value of this parameter has now been published by the CDF and D0 collaborations [18]. The constraint is shown as an orange annulus.

- $|\epsilon_K| = (2.221 \pm 0.008) \times 10^{-3}$ — CP-violation parameter in the kaon system. The constraint is shown as light green bands in complex plane diagram.

- $\sin 2\beta = 0.687 \pm 0.032$ — where this value is taken solely from B decay modes to charmonium final states.

- $|V_{ub}| = (4.45 \pm 0.23 \pm 0.39) \times 10^{-3}$ from inclusive measurements and $|V_{ub}| = (3.94 \pm 0.28 \pm 0.51) \times 10^{-3}$ from exclusive measurements. These are measured from semileptonic B decays. For the inclusive measurement, the process $b \to u\ell\bar{\nu}$ is used, measuring the lepton energy spectrum above the $b \to c\ell\bar{\nu}$ end point. The exclusive measurements look at specific modes such as $B \to \pi\ell\bar{\nu}$ or $B \to \rho\ell\bar{\nu}$

- $|V_{cb}| = (41.70 \pm 0.70) \times 10^{-3}$ from inclusive measurements, and $|V_{cb}| = (41.18 \pm$

$1.71) \times 10^{-3}$ from exclusive measurements. Exclusive measurements are based on studying the decays $B \to D^{(*)}\ell\bar{\nu}$. Inclusive measurements are based on the semileptonic width, which requires both B lifetimes and the branching fraction $\mathcal{B}(B \to X_c\ell\bar{\nu})$ to be measured.

The major sources for the input parameters are the Particle Data Group (PDG), and the Heavy Flavour Averaging Group (HFAG) [19].

There are a number of different parameters given in the results, corresponding to different parametrisations of the CKM matrix, and to the angles of The Unitarity Triangle. Firstly, in the Wolfenstein parametrisation, fit results for the four free parameters are given:

- $\lambda = 0.2272^{+0.0010}_{-0.0010}$

- $A = 0.809^{+0.014}_{-0.014}$

- $\bar{\rho} = 0.197^{+0.026}_{-0.030}$

- $\bar{\eta} = 0.339^{+0.019}_{-0.018}$.

The Unitarity Triangle has its angles fitted in a constrained fit, and also its area $(J/2)$ is measured to be $J = 3.05^{+0.18}_{-0.18} \times 10^{-5}$. The Jarlskog parameter, J, [20] is proportional to the area of all SM unitarity triangles (including The Unitarity Triangle), and its value is also a measure of the magnitude of CP-violation that exists in the SM.

The relevant measurements for the angles are:

- $\sin 2\alpha = -0.25^{+0.17}_{-0.15}$

- $\sin 2\beta = 0.716^{+0.024}_{-0.024}$

- $\alpha = (97.3^{+4.5}_{-5.0})°$

- $\beta = (22.86^{+1.00}_{-1.00})°$

- $\gamma = (59.8^{+4.9}_{-4.1})°$.

These values are those returned from the constrained fit, and the calculated uncertainties on the values are lower than the uncertainties on the angles from any direct measurements. The aim of all these tests is to overconstrain the unitarity triangle, and thus establish any deviation from the unitarity condition, which would show that the CP-violation observed in the associated processes is at least partially derived from sources beyond the standard model. The measurements of the angles of the triangle are constrained to 180° in the fit, and still still have large associated errors. But current fit results are good, and are consistent with the unitarity condition being fulfilled.

2.4   Weak and Strong Phases in Meson Decays

The decay amplitude A_f as defined in section 2.3.1 is a sum of complex quantities each consisting of a magnitude and a phase. The phase however can be further split into two, and A_f may be written as:

$$A_f = \sum_i A_i e^{i(\delta_i + \phi_i)}, \tag{2.45}$$

where A_i is the amplitude of each component to A_f, δ_i is the strong phase, and ϕ_i the weak phase for each component. The CP conjugate of A_f is given by:

$$\bar{A}_{\bar{f}} = \sum_i A_i e^{i(\delta_i - \phi_i)}. \tag{2.46}$$

Any complex parameters of a Lagrangian [21] that contribute to the amplitude will appear as their complex conjugates in the CP conjugate amplitude, and thus the sign of the phase will be reversed. Such phases occur only in weak decays (which incorporate the CKM matrix), and are thus referred to as "weak phases". The second type of phase occurs with decays which are described by a real Lagrangian. There is no change of sign when operated on by CP, and thus they appear the same in both A_f and $\bar{A}_{\bar{f}}$. The dominant source of these phases is strong interactions, and thus they are called "strong phases".

Equation (2.24) can be written in terms of the decay amplitudes of equations (2.45) and (2.46) thus:

$$\left| \frac{\bar{A}_{\bar{f}}}{A_f} \right| = \left| \frac{\sum_i A_i e^{i(\delta_i - \phi_i)}}{\sum_i A_i e^{i(\delta_i + \phi_i)}} \right| . \tag{2.47}$$

Therefore the condition for direct CP-violation, that this quantity is not equal to unity, is fulfilled by having different weak phases. However, writing the difference between the amplitudes squared for the decay and the conjugate decay gives:

$$|A|^2 - |\bar{A}|^2 = -2 \sum_{i,j} A_i A_j \sin(\phi_i - \phi_j) \sin(\delta_i - \delta_j). \tag{2.48}$$

Thus at least two terms with different weak phases must also have different strong phases in order for CP-violation to occur.

The value of weak and strong phases is dependent on how they and related terms are defined. The difference between two phases though is independent of the definition of terms, and thus has some physical meaning. It is the phase differences rather than the actual phases that will be measured in experiments.

The separation of weak and strong phases is experimentally challenging in charmless decays due to the low branching fractions for these processes. The analysis described in this document makes no attempt to separate these phases, and measures only a single combined phase for each component. It would be a goal of a future analysis of this type with a much larger number of signal events to try to separate these two types of phase.

2.5 Trees and Penguins

It is possible to divide particle decays into two categories based on their Feynman diagram topology. These categories are:

- Tree Diagrams — For weak deacys, these are processes where a quark emits a virtual $W^{\pm}$ boson, converting into a lighter quark in the process, and the $W^{\pm}$ then decays to two new particles. Tree diagrams involve no internal loops.
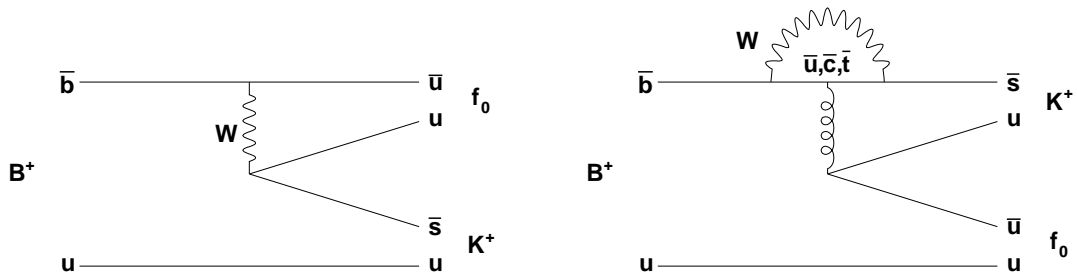
Figure 2.5: Two Feynman Diagrams for the decay $B^+ \rightarrow f_0 K^+$. The left hand diagram shows a tree level decay, and the right hand diagram shows a penguin decay.

- Penguin Diagrams — these processes involve an internal loop in which a virtual $W^{\pm}$ boson splits from and then reconnects with a quark line. In order to conserve energy/momentum a particle must be emitted from the loop. If this is a gluon, the penguin is called a gluonic penguin; if the particle is a photon or a virtual Z^0 boson, the penguin is called an electroweak penguin.

Figure 2.5 shows an example of a tree level process and a penguin level process. Both are shown for the decay $B^+ \rightarrow f_0 K^+$. Both tree and penguin diagrams can contribute to the decay process $B^{\pm} \rightarrow K^{\pm} K^{\pm} K^{\mp}$. Further discussion of the importance of these processes in decays of this type can be found in section 2.6.

2.6   The Decay $B^{\pm} \rightarrow K^{\pm} K^{\pm} K^{\mp}$

Due to its high mass, and hence large phase space for decays, there are a plethora of final states to which a B meson can decay. These many decay channels are subdivided into several general categories sharing similar characteristics — such categories may be: charmless decays, charmed decays, charmonium decays; or two-body decays, quasi-two-body decays, etc. Subdividing in this way allows physicists working on similar analyses, to share knowledge and resources as part of analysis working groups. Similar

modes of decay also share physics goals, and are often sensitive to the same physical parameters, such as an angle of The Unitarity Triangle.

The analysis reported in this thesis is of a charmless three-body decay of a B meson. The following section details why charmless three-body decays are of interest, and what can (potentially) be learned from them. The section will then examine what features the charmless three body decay $B^{\pm} \to K^{\pm}K^{\pm}K^{\mp}$ has that are interesting, and what the motivation to study this decay mode is.

2.6.1 Charmless Decays

The most dominant decays of B mesons are those to charmed states, such as D mesons, where the heavy b quark decays to the next heaviest c quark. Such a decay is a tree level process. The b quark can also decay at tree level to a u quark, however as can be seen from the elements of the CKM matrix (equation (2.36)) this is highly suppressed relative to the $b \to c$ transition. Decays of the b quark to s and d quarks can only take place via penguin loop diagrams, such as those shown in figure 2.7. These processes are also far less frequent than the tree level $b \to c$ decay. Hence charmless decays are much less frequent than charmed or charmonium decays, and can have branching fractions of 10^{-4} to 10^{-6} or even less.

Charmless decays can be dominated by penguin decays; for example the decay $B^{\pm} \to \phi(1020)K^{\pm}$ is dominated by the contribution from $b \to s\bar{s}s$ penguin diagrams. This provides the opportunity to study penguin processes, which can lead to new insight. Greater knowledge of penguins may aid in the analysis of "penguin polluted" decays — those in which the relative amounts of tree and penguin contributions are unknown. It is also possible with many more data that new contributions to penguin diagrams may be observed, which could be a signature of new physics occurring in the loops, such as new heavy bosons, or supersymmetric particles in place of the $W^{\pm}$ and quarks of established penguin processes.

The angle β of the unitarity triangle was the first to be measured, in the measurement of $\sin 2\beta$ from the channel $B^0 \to J/\psi K_S^0$. New analyses are being carried out of

$\sin 2\beta$ from charmless decays, such as $B^0 \to \phi K_S^0$, to determine whether the value of $\sin 2\beta$ is the same in charmless decays as it is in charmonium decays. Early results were inconclusive. Some charmless decays are also sensitive to $\sin 2\alpha$, because they depend on the CKM matrix element V_{ub}.

2.6.2 Three-body decays

There are a large number of three-body states into which a B meson can decay, more so than two-body states. The analysis of a three-body decay allows a full treatment of interference effects between different decay paths (as explained in section 2.8), which can allow the extraction of phases between the different decays (section 2.4 goes into more detail of phases). Analyses in terms of (quasi-)two-body decay modes are unable to measure interference phases, and have to treat the effects of interference on amplitude or branching fraction measurements as a systematic uncertainty.

2.6.3 Possible Contributions to the mode $B^\pm \to K^\pm K^\pm K^\mp$

Figure 2.6 shows some possible Feynman diagrams for the process $B^\pm \to K^\pm K^\pm K^\mp$, and figure 2.7 shows some Feynman diagrams for the decay $B^\pm \to \phi(1020)K^\pm$, which can result in a three charged kaon final state upon the further decay $\phi \to K^+K^-$.

In figure 2.6, the top left subfigure shows an annihilation diagram, where the constituent quarks of the meson annihilate to form a W, which decays back into two quarks, which then hadronise into three kaons. (The formation of intermediate resonant states would also be possible in an annihilation diagram.) The top right subfigure shows a non-resonant tree diagram, whereby the decay leads directly to three kaons with no resonant substructure; the bottom left subfigure shows the formation of a resonant state, which is composed of u and $\bar{u}$ quarks, that then decays to two kaons; the bottom right diagram is a more speculative process showing the possible formation of a glueball (a hypothetical exotic particle composed only of gluons), that decays to two kaons.
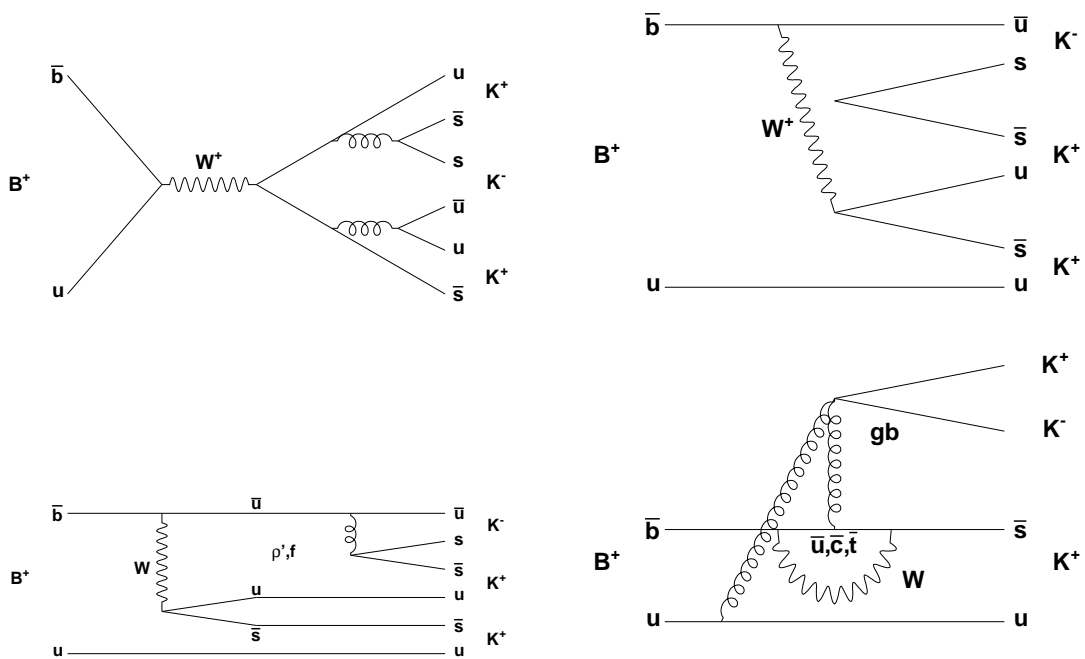
Figure 2.6: Four possible Feynman diagrams for the process $B^\pm \to K^\pm K^\pm K^\mp$ — clockwise from top left — Annihilation diagram; Non-resonant tree diagram; Speculative process involving a glueball (labelled gb); Tree level decay of a $u\bar{u}$ meson.
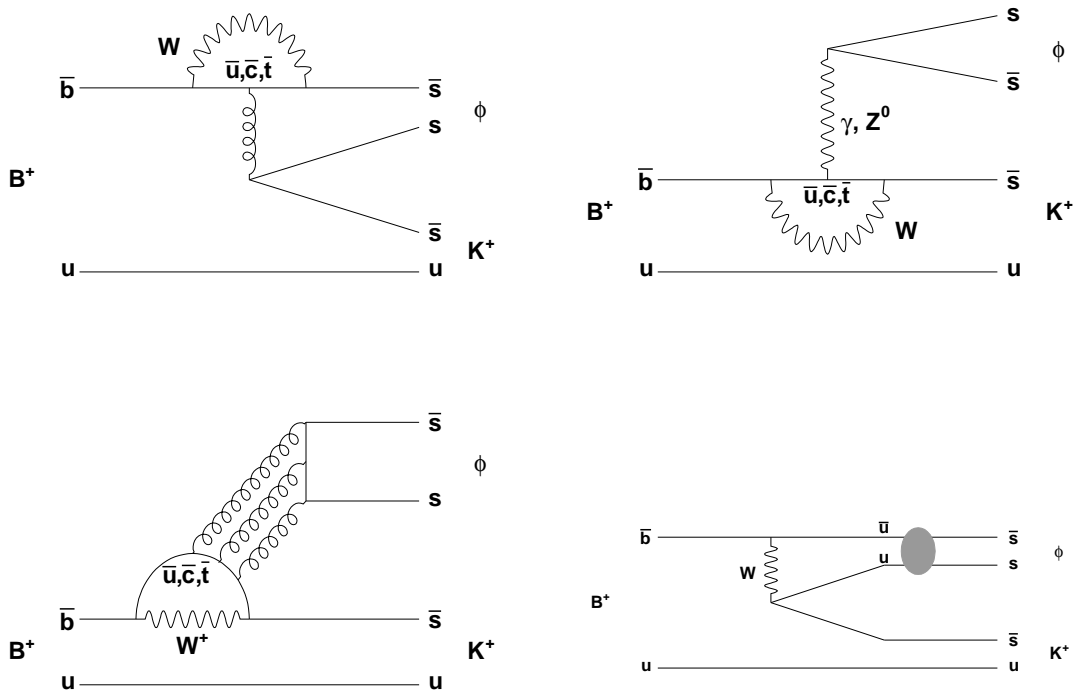
Figure 2.7: Four possible Feynman diagrams for the process $B^{\pm} \to \phi(1020)K^{\pm}$ — clockwise from top left — Internal penguin diagram; Electroweak penguin diagram; Rescattering diagram; Flavour singlet penguin diagram.

Figure 2.7 shows possible diagrams for the decay $B^{\pm} \to \phi(1020)K^{\pm}$ — the top left subfigure shows an internal penguin diagram; the top right subfigure shows an electroweak penguin diagram, with a photon or Z^0; the bottom left subfigure shows a flavour singlet penguin diagram; the bottom right subfigure shows a rescattering diagram, where a $u\bar{u}$ meson is formed, but undergoes an internal interaction that converts it to an $s\bar{s}$ state.

2.6.4 Other Analyses of $B^{\pm} \to K^{\pm}K^{\pm}K^{\mp}$

The first *BABAR* analysis of the decay mode $B^{\pm} \to K^{\pm}K^{\pm}K^{\mp}$ [22] was based on $81.8\,\text{fb}^{-1}$ of data. It did not include a full amplitude analysis of the Dalitz plot. The interference between different components was not modelled, but was accounted for as a systematic uncertainty. The $\phi(1020)$ was the only resonance noted (the χ_{c0} region was vetoed, as well as the D^0 region). The measured branching fraction from this analysis was:

$$\mathcal{B}(B^{\pm} \to K^{\pm}K^{\pm}K^{\mp}) = (29.6 \pm 2.1 \pm 1.6) \times 10^{-6}. \tag{2.49}$$

The results also included a CP asymmetry for this decay mode. This was measured to be:

$$A_{CP}(B^{\pm} \to K^{\pm}K^{\pm}K^{\mp}) = 0.02 \pm 0.07 \pm 0.03. \tag{2.50}$$

The *BABAR* collaboration has also published papers detailing the measurements of the two body branching fractions for the modes $B^{\pm} \to \phi(1020)K^{\pm}$ [23] [24] and $B^{\pm} \to \chi_{c0}K^{\pm}$ [25].

The measured branching fraction for $B^{\pm} \to \phi(1020)K^{\pm}$ was:

$$\mathcal{B}(B^{\pm} \to \phi(1020)K^{\pm}) = (10.0^{+0.9}_{-0.8} \pm 0.5) \times 10^{-6}, \tag{2.51}$$

and the asymmetry on this mode was:

$$A_{CP}(B^{\pm} \to \phi(1020)K^{\pm}) = 0.04 \pm 0.09 \pm 0.01. \tag{2.52}$$

The analysis of $B^\pm \to \chi_{c0} K^\pm$ calculates a branching fraction for the case where the χ_{c0} decays to two charged kaons:

$$\mathcal{B}(B^\pm \to \chi_{c0} K^\pm) \times \mathcal{B}(\chi_{c0} \to K^+ K^-) = (1.49^{+0.36}_{-0.34} \pm 0.11) \times 10^{-6}. \qquad (2.53)$$

Dalitz Analyses

More recent analyses have been full Dalitz plot analyses. These have been carried out by the *BABAR* [26] and Belle [27] collaborations. A comparison of these publications with the results of this analysis is carried out in section 7.2.

2.6.5 Other Analyses Related to $B^\pm \to K^\pm K^\pm K^\mp$

The Decay $B^\pm \to K^\pm \pi^\pm \pi^\mp$

The *BABAR* analysis [28] of this mode was carried out using a similar method to that described in this thesis, using the `Laura++` fitting package (section 5.1). Of particular note is the treatment and measurement of the $f_0(980)$ resonance. This resonance can decay to both $\pi^+ \pi^-$ and $K^+ K^-$, and is seen in both $B^\pm \to K^\pm \pi^\pm \pi^\mp$ and $B^\pm \to K^\pm K^\pm K^\mp$ channels. The mass of the $f_0(980)$ resonance is slightly less than the mass of a pair of kaons, which distorts the lineshape to a Flatté or coupled channel Breit–Wigner form (section 2.9.3). The shape of the $f_0(980)$ is more like a conventional Breit–Wigner in the decay $B^\pm \to K^\pm \pi^\pm \pi^\mp$, and it is easier to distinguish the resonant structure in the plot (allowing for overlap from the ρ). The Flatté parameters could thus be tested in this mode, and were found to be in broad agreement with those measured by the BES collaboration [29]. The observation of this resonance in the $B^\pm \to K^\pm \pi^\pm \pi^\mp$ Dalitz plot was a useful guide in determining the presence of the $f_0(980)$ resonance in the $B^\pm \to K^\pm K^\pm K^\mp$ Dalitz plot.

The Decay $B^0 \to K^0_S K^\pm K^\mp$

This mode featuring three kaons, has a lower branching fraction than $B^\pm \to K^\pm K^\pm K^\mp$, and it is more difficult to reconstruct the K^0_S compared to a charged

kaon. Consequently, the *BABAR* analysis of $B^0 \to K^0_S K^{\pm} K^{\mp}$ [30] had fewer signal events than the mode containing three charged kaons, despite using a larger data sample.

A resonant structure is observed at $\sim 1.5\,\mathrm{GeV}/c^2$ in $B^{\pm} \to K^{\pm}K^{\pm}K^{\mp}$ analyses, and is also seen in the K^+K^- invariant mass spectrum of $B^0 \to K^0_S K^{\pm} K^{\mp}$. However no such structure is observed in the $K^0_S K^+$ or $K^0_S K^-$ spectra, which would indicate that the resonance has no charged counterparts, and therefore favours an (isospin = 0) f resonance designation, as opposed to an (isospin = 1) a resonance designation. Thus this resonant structure cannot be identified with the established $a_0(1450)$ resonance. The observation of such a resonant structure in this analysis is noted in section 6.1.1.

2.7   Nature of Resonant Components

The analysis detailed in this thesis involves modelling the potential resonant content in the decay mode $B^{\pm} \to K^{\pm}K^{\pm}K^{\mp}$. Whilst many resonances are well established particles, there remains a lot of uncertainty about the identification of some other resonances, and in the scalar resonance sector in particular it is often not possible to identify distinct resonances.

Even resonances that are well established, seen in several experiments with different techniques, can still have uncertainties surrounding their composition. Mesons that are formed from states other than $q\bar{q}$ have been postulated. Scalar resonances which overlap and interfere with each other lead to the situation where it has not been possible to determine the quark composition of these particles, even within the $q\bar{q}$ regime.

Two resonances that are modelled in this analysis are examples of the confusion of scalar resonances that exists — the $f_0(980)$, and a scalar resonance with a mass of $\sim 1.5\,\mathrm{GeV}/c^2$, which is referred to as $(KK)^0_0$ (the reasons for this arbitrary resonance being studied are given in section 6.1).

Studies by the LASS collaboration [31] on the $K^0_S K^0_S$ system in the reaction $K^- p \to$

$K_S^0 K_S^0 \Lambda$ showed the $f_2'(1525)$ to be the major contribution to the resonant spectrum. However they also presented some evidence for an s-wave structure lying in the region of 1.5 to 1.6 GeV/c^2, and a similar structure is seen in an analysis that replaces the $K_S^0 K_S^0$ pair with a $K^+ K^-$ pair. Though the uncertainties of the LASS analysis are large, their s-wave fits are at least four standard deviations different from a zero s-wave hypothesis. They conclude that the structure they see "may correspond to a 0^{++} mainly $s\bar{s}$ state approximately degenerate with the $f_2'(1525)$".

2.7.1 Theoretical predictions of (possible) resonant contributions in the $K^+ K^-$ Spectrum

Some theoretical papers make predictions about resonances that may occur decaying to $K^+ K^-$ pairs. Some of these are considered in this section.

The paper of Furman, Kamiński, Leśniak, and Loiseau [32] looks at $\pi\pi$ and $K\bar{K}$ pairs interacting in an isospin zero s-wave state, at energies up to 1.2 GeV. It is noted that some theoretical predictions for $\mathcal{B}(B^\pm \to f_0(980)K^\pm)$ are much too small, due to penguin amplitudes interfering destructively.

Long range contributions from "charming penguins" are considered, which are constructions with enhanced charm quark loops, such as B decays to intermediate $D_s^{(*)} D^{(*)}$ where $c\bar{c}$ annihilations lead to a final state of $f_0(980)K$. These contributions act as an enhancement to predictions that are too low, to bring them closer to experimental results.

The two models presented make predictions of $(1.8\pm0.4)\times10^{-6}$ and $(1.7\pm0.7)\times10^{-6}$ for the branching fraction $B^\pm \to (K^+ K^-)_S K^\pm$, where the S signifies the kaons are in an s-wave state. The predictions are in better agreement with experimental results, and agree well with Belle results [27], but are still below measurements from *BABAR* [26].

The paper by Cheng, Chua, and Yang [33] looks at the nature of light scalar mesons, arising from the study of charmless hadronic B decays. They include a section on the

35

$B^- \to f_0(980)K^-$ decay. There are several different predictions for the composition of the $f_0(980)$ resonance discussed: the two quark predictions are $s\bar{s}$ or a superposition of $s\bar{s}$ and $(u\bar{u} + d\bar{d})/\sqrt{2}$, and a four quark prediction is $|f_0(980)\rangle = |s\bar{s}(u\bar{u} + d\bar{d})/\sqrt{2}\rangle$, though further four-quark possibilities arising from mixing with a four-quark σ resonance are also suggested.

It is noted from measurements of the decays $J/\psi \to f_0\omega$ and $J/\psi \to f_0\phi$ that the f_0 clearly has both strange and non-strange content.

The predictions of the authors based on QCD factorisation give a branching fraction of order 10^{-5} for $B^- \to f_0K^-$, based on a two quark model. Extending this to a four quark model would result in a lower branching fraction based on extending the penguin diagrams for the two quark states to four quark states. However there are two extra diagrams for four quark states, which are nonfactorisable, and thus the calculation of a predicted branching fraction cannot be performed. Thus, the observation of the branching fraction for $B^- \to f_0K^-$ cannot be used to distinguish between a two quark and a four quark assignment.

Minkowski and Ochs [34] look at the decays of B mesons into light scalars and glueballs, motivated by the search for the lightest glueball. This glueball is expected to be a scalar with $J^{PC} = 0^{++}$. Some predictions of its mass give a range of 1000-1800 MeV/c^2.

They discuss different classifications for the light scalar mesons to highlight where such a glueball may appear. The $f_0(980)$ could occur as the lightest member of a nonet comprising particles such as the $f_0(1500)$ and $K_0^*(1430)$. Or it could be the heaviest member of a nonet featuring such particles as the κ and σ; such an arrangement could lead to two nonets below $1.8\,\text{GeV}/c^2$.

They also comment on the observation of the $f_0(1500)$ resonance in $B^\pm \to K^\pm K^\pm K^\mp$, but not in $B^\pm \to K^\pm \pi^\pm \pi^\mp$. They construct a model attributing this observation to the constructive and destructive interference in these modes with a broad glueball state. The presence and possible identification of the $f_0(1500)$ in the analysis of $B^\pm \to K^\pm K^\pm K^\mp$ detailed in this thesis are discussed in section 6.1.

2.8 Kinematics of three body decays

In the decay of a particle of mass M and momentum $\mathbf{P}$ into three daughter particles with momenta and masses $(\mathbf{p_1}, m_1)$, $(\mathbf{p_2}, m_2)$, $(\mathbf{p_3}, m_3)$, and with the invariant masses of the three possible pairs of particles:

$$m_{ij}^2 = p_{ij}^2 = (\mathbf{p}_i + \mathbf{p}_j)^2 \tag{2.54}$$

for $i, j = 1, 2, 3$; then:

$$M^2 + m_1^2 + m_2^2 + m_3^2 = m_{12}^2 + m_{13}^2 + m_{23}^2. \tag{2.55}$$

Since the squares of the invariant masses of the three pairs of particles are linearly dependent, any choice of two pairs can be used to specify the kinematics of a decay. It can be shown that the decay rate, $d\Gamma$, is proportional to [35]:

$$d\Gamma \propto |\bar{\mathcal{M}}|^2 dm_{13}^2 dm_{23}^2 \tag{2.56}$$

where $\mathcal{M}$ is the matrix element for the decay process. The general form $\bar{\mathcal{M}}$ is averaged over spin states for the decaying particle. Thus for a decay with constant $|\bar{\mathcal{M}}|^2$ then the decay events will be distributed uniformly across phase space (within a certain kinematic boundary).

A scatter plot of m_{13}^2 against m_{23}^2 is called a Dalitz plot. When $\mathcal{M}$ is not constant across phase space then features of interest may appear within the Dalitz plot. This can arise when a three body decay proceeds via an intermediate resonance, for example $B^\pm \to \phi(1020)K^\pm$, $\phi(1020) \to K^+K^-$. In this case $\mathcal{M}$ is enhanced for values $m_{ij}^2 = m_{resonance}^2$, leading to the formation of resonance bands within the plot.

Where there are multiple resonances present it is possible for interference to occur, as the individual contributions to the matrix element are summed before the matrix element is squared leading to cross/interference terms.

Figure 2.8 shows an example of a Dalitz plot for the decay $B^\pm \to K^\pm K^\pm K^\mp$ composed of simulated events. (The generation of simulated or Monte Carlo events is discussed in section 4.1.1). This plot contains several generated resonances that could
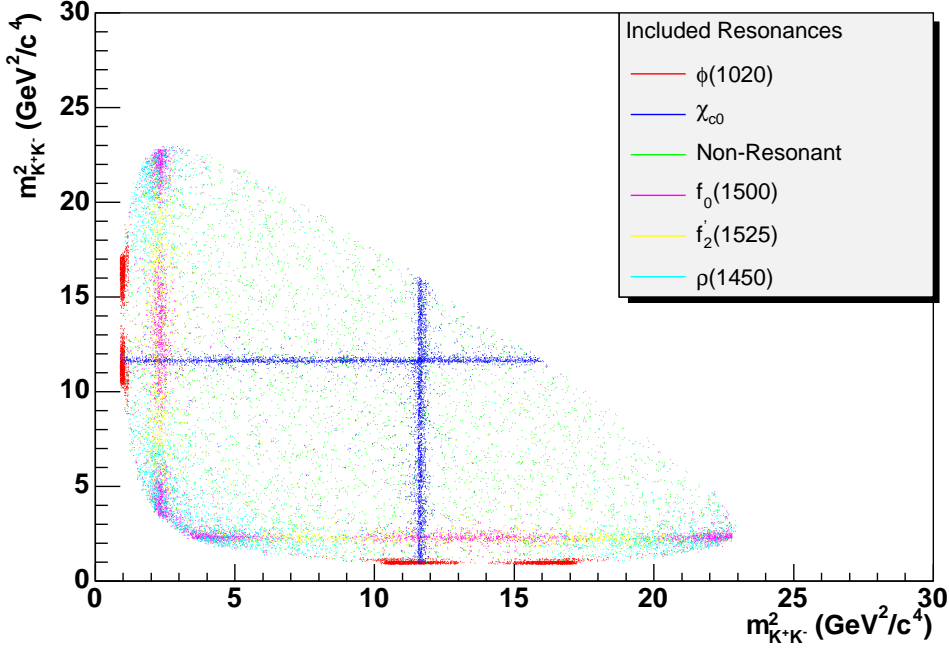
Figure 2.8: Toy Monte Carlo simulation of $B^{\pm} \to K^{\pm}K^{\pm}K^{\mp}$.

contribute to the overall decay mode, which have been highlighted to demonstrate the way in which individual resonance bands populate the Dalitz plot. Note — in order to keep the resonance assignment of each generated event unambiguous, interference effects were not modelled for the purposes of this plot.

Each resonance in the Dalitz plot is represented by both a dynamical term (related to the lineshape, described in section 2.9), and an angular distribution, T, which is defined in terms of Zemach Tensors [36] [37] as follows:

$$L = 0 : T = 1 \tag{2.57}$$

$$L = 1 : T = -2\vec{p}.\vec{q} \tag{2.58}$$

$$L = 2 : T = \frac{4}{3}\left[3(\vec{p}.\vec{q})^2 - (|\vec{p}||\vec{q}|)^2\right] \tag{2.59}$$

where the terms are used for the decay of a spin 0 particle, and L is the orbital angular momentum between daughter particles. The vectors $\vec{p}$ and $\vec{q}$ are measured in the rest

frame of the decaying resonance, and are the momentum of the bachelor particle (the particle that was created from the decay of the B meson, i.e. not involved in the decay of the intermediate resonance), and the momentum of the daughter particle of the resonance with an electric charge identical to that of the bachelor particle.

The angular distribution above can be observed as a function of a helicity angle, which can be defined for each of the pairs of particles in a three body decay, in a similar way to the definition of invariant masses. The helicity angle, θ_{ij} can be defined in terms of the invariant mass of another pair of particles as:

$$\theta_{ij} = \frac{(m_{jk}^2)_{max} + (m_{jk}^2)_{min} - 2m_{jk}^2}{(m_{jk}^2)_{max} - (m_{jk}^2)_{min}}. \qquad (2.60)$$

The resonance bands in a Dalitz plot show information about the spin of the resonance involved, in terms of the helicity angle, a spin zero resonance (e.g. χ_{c0}) will be flat across the Dalitz plot band; a spin one resonance (e.g. $\phi(1020)$) will be distributed according to $\cos^2 \theta_{ij}$; and a spin two resonance (e.g. $f_2'(1525)$) distributed by $|3\cos^2 \theta_{ij} - 1|^2$. This can be seen in the resonance bands in figure 2.8. These distributions are contained within the Zemach Tensor formalism.

2.8.1 Kinematic boundaries of a Dalitz plot

The area of the Dalitz plot is determined by the available phase space, and the boundaries of the plot are determined by the kinematic constraint on the particles, that is, when one of the particles has no momentum, in the decay rest frame.

The boundary of the Dalitz plot is described in terms of two of the Dalitz plot coordinates. It can be plotted from two curves for the upper and lower edges, as there are two possible values of the boundary for every permitted value of the abscissa.

Using m_{12}^2 as the abscissa, and m_{23}^2 as the ordinate, the value of the upper and lower boundaries can be specified as [35]:

$$(m_{23}^2)_{max} = (E_2^* + E_3^*)^2 - \left(\sqrt{E_2^{*2} - m_2^2} - \sqrt{E_3^{*2} - m_3^2}\right)^2 \qquad (2.61)$$

$$(m_{23}^2)_{min} = (E_2^* + E_3^*)^2 - \left(\sqrt{E_2^{*2} - m_2^2} + \sqrt{E_3^{*2} - m_3^2} \right)^2, \qquad (2.62)$$

where E_2^* and E_3^* are the energies of particles 2 and 3, and the $*$ signifies that they are given in the m_{12} rest frame, as follows:

$$E_2^* = \frac{m_{12}^2 - m_1^2 + m_2^2}{2m_{12}} \qquad (2.63)$$

$$E_3^* = \frac{M^2 - m_{12}^2 - m_3^2}{2m_{12}}. \qquad (2.64)$$

The absolute minimum value that can be taken for m_{12}^2 is $(m_1 + m_2)^2$, and the maximum value is $(M - m_3)^2$. For m_{23}^2 the corresponding values are $(m_2 + m_3)^2$, and $(M - m_1)^2$.

In the case of $B^\pm \to K^\pm K^\pm K^\mp$ these expressions simplify to a minimum of $(m_K + m_K)^2 = 4m_K^2 = 0.975\,\text{GeV}^2/c^4$ and a maximum of $(m_B - m_K)^2 = 22.9\,\text{GeV}^2/c^4$ in both cases.

2.9 Lineshapes

This section describes the shapes of resonance phenomena in the invariant mass spectra. These parametrisations are used to define the resonances when fitting the Dalitz plot.

2.9.1 Breit–Wigner

The Breit–Wigner lineshape is the most common used for parametrising resonance shapes. Further details can be found in, for example [38]. The time dependent wave function of a particle, R, of mass m_R and width Γ_R can be written as:

$$\psi(t) = \psi(0)e^{-im_R t}e^{-\Gamma_R t/2}. \qquad (2.65)$$

Taking the Fourier transform of this wave function leads to an expression for the amplitude of this particle state as a function of energy, E:

$$\chi(E) = \int \psi(t)e^{iEt}dt \propto \frac{1}{E - m_R + i\Gamma_R/2}. \qquad (2.66)$$

To find the cross section for observing the decay of such a particle, then the square of the amplitude is taken:

$$\sigma(E) = \chi^*(E)\chi(E) \propto \frac{1}{(E - m_R)^2 + \Gamma_R^2/4}. \tag{2.67}$$

This equation is known as the Breit–Wigner formula.

2.9.2 Relativistic Breit–Wigner

The Breit–Wigner formula can be extended in order to make it relativistically invariant. In this form, the cross section is expressed in terms of the relativistic variable s, which is the square of the centre of mass energy. The form of the relativistic Breit–Wigner is as follows:

$$\sigma(s) \propto \frac{1}{(s - m_R^2)^2 + \Gamma_R^2 m_R^2}. \tag{2.68}$$

An additional relativistic consideration is that the width of the resonance is expected not to be a constant, but instead to vary as a function of energy. This can be accounted for using the Blatt–Weisskopf parametrisation [39], which is given as:

$$\Gamma_R(s) = \Gamma_R(m_R^2) \left(\frac{q}{q_0}\right)^{2j+1} \frac{m_R}{\sqrt{s}} \frac{F_j^2(q)}{F_j^2(q_0)}. \tag{2.69}$$

Here q represents the momentum of one of the daughter particles of the decay, measured in the rest frame of the particle R. The parameter q_0 is the value of q at $s = m_R^2$. The function $F_j(q)$ describes the variation of the width due to the spin of the resonance, and is given for particles of spin 0, 1, and 2 as:

$$F_0(q) = 1 \tag{2.70}$$

$$F_1(q) = \sqrt{\frac{1}{R_b^2 q^2 + 1}} \tag{2.71}$$

$$F_2(q) = \sqrt{\frac{1}{R_b^4 q^4 + 3R_b^2 q^2 + 9}} \tag{2.72}$$

The barrier radius, R_b, is taken to have a value of $4.0(\,\mathrm{GeV}/c)^{-1}$.

2.9.3 Flatté — Coupled Channel Breit Wigner

The Flatté lineshape [40] is used to represent resonances that occur near the threshold for a particular decay mode. Of particular interest for this analysis is the decay of the $f_0(980)$, which has two notable decay modes:

- $f_0(980) \to \pi^+\pi^-$,

- $f_0(980) \to K^+K^-$.

The nominal mass of the $f_0(980)$ is slightly less than the mass of a pair of charged kaons. The Flatté distribution takes into account both the $\pi^+\pi^-$ decay and the opening of the K^+K^- decay, thus:

$$\chi(s) \propto \frac{1}{m_R^2 - s - im_R(\Gamma_{\pi\pi} + \Gamma_{KK})}. \tag{2.73}$$

The two width terms describe the contributions from the two decay channels, and are given hence:

$$\Gamma_{\pi\pi} = g_\pi \sqrt{s - 4m_\pi^2} \tag{2.74}$$

$$\Gamma_{KK} = g_K \sqrt{s - 4m_K^2}. \tag{2.75}$$

Accordingly for $s < 4m_K^2$, the width parameter Γ_{KK} will be imaginary, and so the term $im_R\Gamma_{KK}$ will contribute to the real part of the denominator.

This parametrisation of the Flatté distribution is that favoured by the BES collaboration, and the values of the parameters are also taken from those published by this collaboration [29]. The particular parameter values used in this analysis are:

- $g_\pi = 0.138 \pm 0.010$,

- $g_K/g_\pi = 4.45 \pm 0.25$.

2.9.4 Non-Resonant

Any decays that do not proceed via an intermediate resonance are termed non-resonant. If these events are distributed according to the phase space distribution then they

should uniformly populate the Dalitz plot. However it is possible that any variations in the matrix element will lead to a non uniform non-resonant component. Some resonant components may be included in the non-resonant contribution where resonant behaviour is not observed. Examples include very wide scalar resonances, and virtual resonances which exist outside the kinematic limits of the Dalitz plot.

There are theoretical predictions as to the nature of a non uniform non-resonant component. Experimentally it may be very difficult to distinguish between these models given the limited amount of data available, and simple parametrisations of the non-resonant component have been suggested to attempt to model any non-uniformity.

The Belle collaboration [27] suggested this parametrisation for the amplitude of the non-resonant component:

$$A_{NR} \propto e^{-\alpha s} + e^{-\alpha t} \tag{2.76}$$

where α is a parameter to be determined, and s and t are the conventionally defined Mandelstam variables. An alternative parametrisation was suggested by a *BABAR* physicist [41], motivated by taking a Taylor expansion of a theoretical model, with only a linear term retained. This leads to the following parametrisation:

$$A_{NR} \propto 1 + \alpha \frac{(s+t)}{m_B^2} \tag{2.77}$$

where again the parameter α is used to represent a free parameter in the fit, and s and t are defined as before. The inclusion of the mass of a B meson, m_B, ensures that α is a dimensionless quantity.

Both of these parametrisations were investigated in this analysis.

Chapter 3

BABAR and PEP-II

The Stanford Linear Accelerator Center (SLAC), the home of the *BABAR* experiment, was founded in 1962, near Stanford University in Menlo Park, California, USA. The linear accelerator which gives SLAC its name is about 3km long and started running in 1966 [42].

The Positron Electron Project (PEP) which commenced operations in 1980 was a symmetric e^+e^- storage ring, which is about 800m in diameter, or 2200m in circumference [43] , where amongst other research, early measurements of the B-lifetime were made.

In 1993 the collaboration which was to become *BABAR* was created. Part of the design proposal for the new b-factory called for the existing PEP ring to become an asymmetric ring, colliding electrons and positrons at energies of 9.0 and 3.1 GeV respectively. This iteration of the storage rings was known as PEP-II.

PEP-II collides electron and positron beams together at a single interaction region, which is where the *BABAR* detector is situated. The PEP-II ring and the *BABAR* detector are described in detail in this chapter.

Table 3.1: Cross sections at a centre of mass energy of 10.58 GeV, corresponding to the mass of the $\Upsilon(4S)$ [44].

Mode	Cross-section $e^+e^- \to$ mode / nb
$B\bar{B}$	1.05
$q\bar{q}$ $(q = u, d, s, c)$	3.2
$\tau^+\tau^-$	0.94
$\mu^+\mu^-$	1.16
e^+e^-	~ 40

3.1 B-Factories and the $\Upsilon(4S)$ resonance

B mesons provide a useful tool to study CP violation, and can also give hints of new physics. But in order to investigate B mesons, and their decays (some of which may have branching fractions of the order 10^{-6} or less), then these particles will need to be produced in large quantities.

The idea of a machine able to produce a large number of B mesons is made possible due to the useful properties of the $\Upsilon(4S)$ resonance. The $\Upsilon(4S)$ is a meson composed of a b quark, and the anti-quark $\bar{b}$. It has a mass of 10.58 GeV/c^2. Its mass is just above the threshold for the production of B and $\bar{B}$ mesons (produced as either B^+ and B^- or as B^0 and $\bar{B}^0$, in an approximate 50:50 ratio). A consequence of this is that at least 96% of decays of the $\Upsilon(4S)$ are to $B\bar{B}$ pairs [1].

By tuning the energy of the electron-positron collisions to the mass of the $\Upsilon(4S)$ the production of $B\bar{B}$ pairs can be optimised. A machine operating at such an energy is termed a B factory. Table 3.1 shows the cross-sections for selected e^+e^- channels at a centre of mass energy of 10.58 GeV. Thus B factories offer an ideal chance to study B mesons, with relatively low backgrounds from light quark production, and additionally allow for the study of charmed particles (such as D mesons) and the τ lepton.

Because the energy in the beams is only just above the threshold for production of $B\overline{B}$ pairs, these mesons are produced almost at rest in the centre of mass frame. In order to have the B mesons move a measurable distance in the detector, the beams are chosen to be asymmetric. An approximate ratio of 3:1 was found to be optimal, and the high energy beam (e^-) has an energy of 9.0 GeV and the low energy beam (e^+) has an energy of 3.1 GeV to give the required centre of mass energy of 10.58 GeV. This gives a relativistic boost in the laboratory frame of $\beta\gamma = 0.56$.

3.2 PEP-II

The Linear Accelerator (Linac) at SLAC is used to provide electrons and positrons. Firstly electrons are fired from an electron gun down the linac, and accelerated to energies of 9.0 GeV before being injected into the PEP-II High Energy Ring (HER). Additionally some electrons are diverted from the linac, and are collided with a stationary target. From the products of these collisions, a magnetic field is used to separate positrons. Bunches of positrons thus formed are then accelerated by the Linac to energies of 3.1 GeV before they in turn are injected into the Low Energy Ring (LER). A schematic view of the linac and the PEP-II ring is shown in Figure 3.1.

Once the electrons and positrons have been injected, the PEP-II ring acts as two storage rings, one for the electrons and the other for the positrons. These maintain the particles at their injected energies as they traverse their circular paths. At one point in the ring – the Interaction Region (IR), the HER and LER beams are brought together, so that electrons and positrons within the bunches may collide. A diagram of the interaction region is shown in Figure 3.2. The beams pass each other with no crossing angle, and thus the beams have to be brought to colinearity, allowed to cross, and then moved back to different paths before collisions between bunches one bunch removed from the colliding bunch can occur.

All of the magnets labelled as QD or QF are quadrupole magnets. Two sets
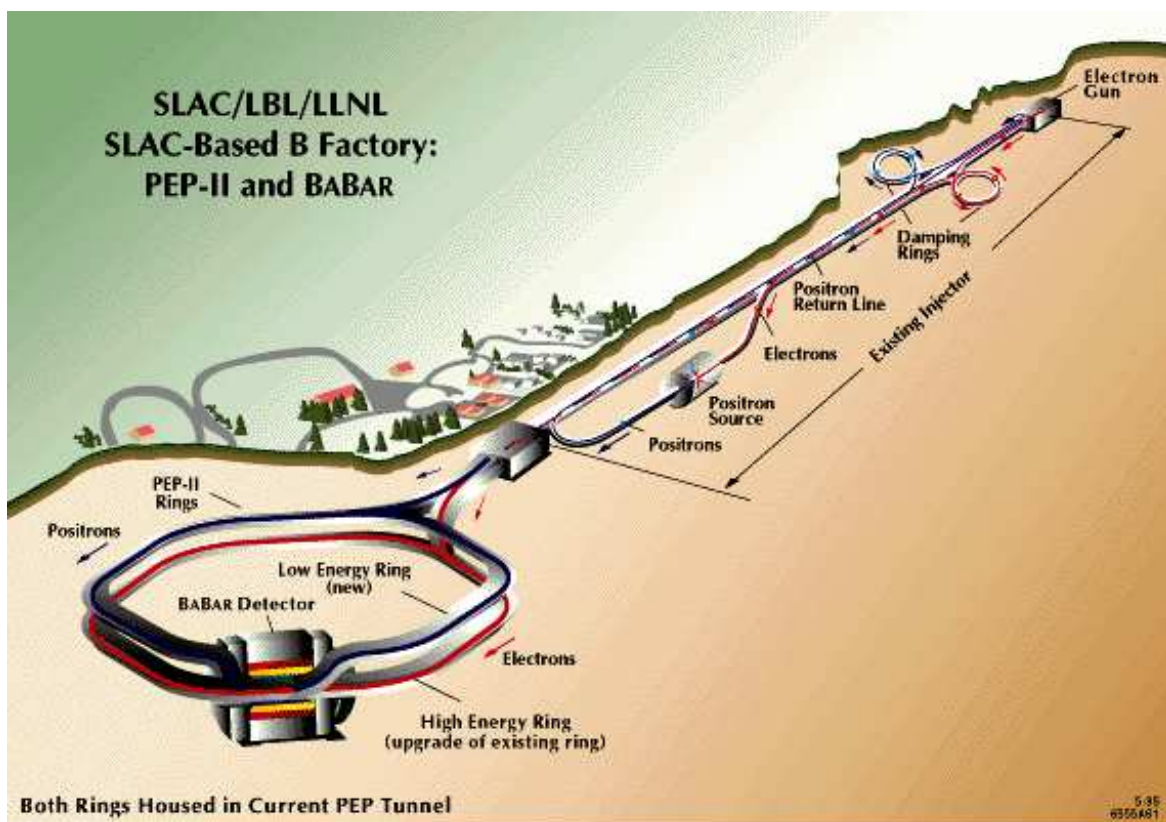
Figure 3.1: The Linear Accelerator and PEP-II

Interaction Region
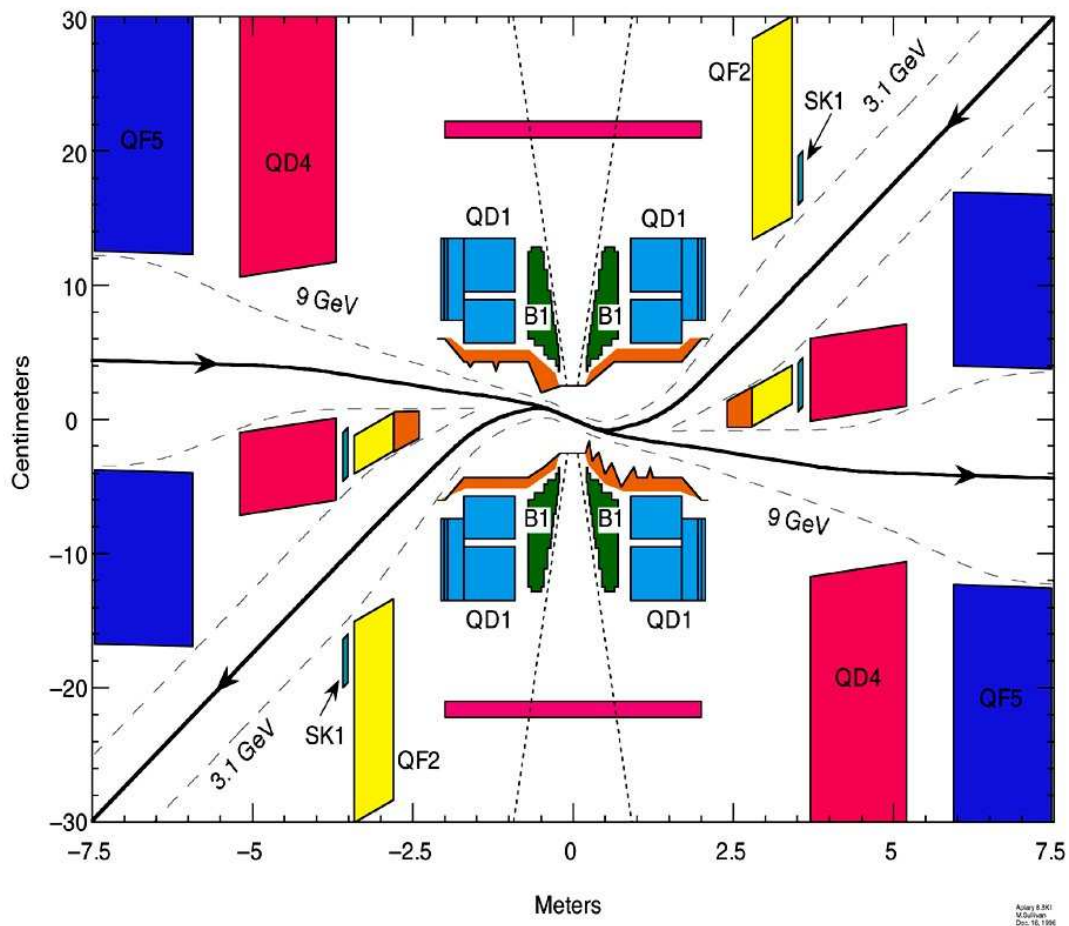
Figure 3.2: The Interaction Region

of quadrupoles are responsible for focusing the higher energy beam, these are QF5 and QD4, whereas only a single set of quadrupoles, QF2, perform the equivalent focusing for the lower energy beam. The final quadrupole is within the magnetic field of the detector, and this implements final focusing for both beams. The final bringing together of the beams is obtained using a dipole magnet, labelled B1.

One of the advantages of an electron positron collider as operated at PEP-II, as compared to the Tevatron at Fermilab (a proton/antiproton collider) or the future Large Hadron Collider (LHC) at CERN (a proton/proton collider) is that e^+e^- collisions have a much lower background than colliding (anti-)protons which are composite particles. This arises as there are many quarks and gluons around the interaction area that can produce large hadronic backgrounds for events of interest, and can greatly reduce the efficiency for reconstructing events.

Some relevant performance indicators for $B\overline{B}$ events produced at PEP-II are [44]:

- Final states involving photons and π^0s can be fully reconstructed.

- The signal to background ratio is high — $\sigma_{b\bar{b}}/\sigma_{TOT} \approx 0.28$.

- The charged particle multiplicity is ≈ 11.

- A low rate of ~ 10Hz for recording physics events.

3.2.1   Trickle Injection

When the experiment started running, the method used to obtain usable beams was that the storage rings were filled with electrons and positrons, until the desired beam current was reached. These beams would slowly diminish in current during a period of data taking. After some time (several hours typically) data taking would be suspended, and more electrons and positrons would be injected, to bring the beams back to full currents. Data taking would then resume.

In order to remove this "dead time", when no data taking was possible, a new system was implemented called Trickle Injection. This involves small quantities of

Table 3.2: PEP-II performance

	Design	Best Achieved
HER current (A)	0.75	1.9
LER current (A)	2.14	2.995
Bunches	1658	1722
Luminosity (10^{33}cm^{-2}s^{-1})	3	12.069

positrons and electrons being continually injected into the beams to keep them at or about full current during a data taking period.

3.2.2 PEP-II performance

PEP-II has been supplying electron and positron beams for the *BABAR* detector since 1999. During this time there have been 5 data taking periods, called "Runs". Between Runs the detector has been shut down to allow for maintenance and upgrades.

Figure 3.3 shows the total integrated luminosity delivered by PEP-II during Runs 1-5, together with the integrated luminosity recorded by the *BABAR* detector, and integrated luminosity taken during off-peak running.

Table 3.2 shows the design parameters of PEP-II and *BABAR*, together with the best achieved to date. The figures are correct at the end of Run 5 in August 2006. The peak luminosity of 12.069×10^{33}cm^{-2}s^{-1} was achieved with 1722 bunches, and beam currents of 2900mA in the LER and 1875mA in the HER.

3.3 The *BABAR* Detector

A full description of the *BABAR* detector is given in [46]. The *BABAR* detector is designed to make precision measurements of the decays of B mesons and associated daughter particles, and also particles such as τ leptons, and charmed particles such as D mesons. The detector covers the whole 4π solid angle around the interaction point

09/12/2006 04:23
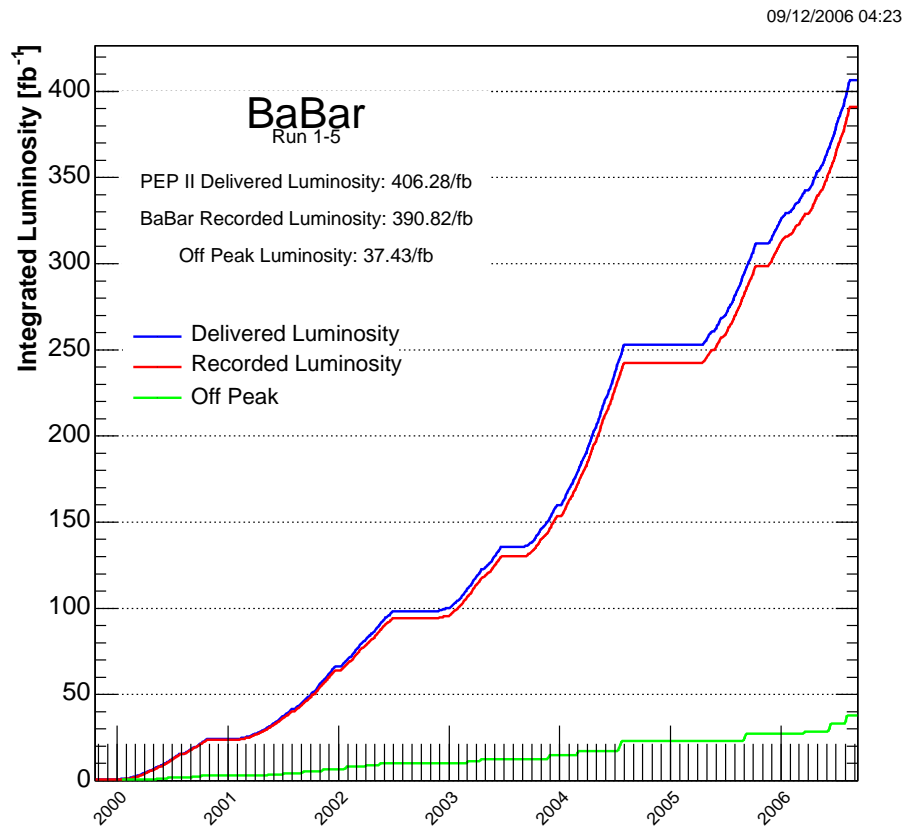
Figure 3.3: PEP-II delivered integrated luminosity, *BABAR* recorded integrated luminosity, and off-peak integrated luminosity [45].

(excepting the beam line). Due to the asymmetric nature of the beams, the detector itself is asymmetric in design. The *BABAR* detector must meet a number of design goals in order to reach the physics potential for which it was intended. A number of these design goals are:

- For charged particles: Good momentum resolution in the range $60\,\mathrm{MeV}/c$ to $4\,\mathrm{GeV}/c$.

- For neutral particles: Good angular resolution, and good energy resolution in the range $20\,\mathrm{MeV}$ to $4\,\mathrm{GeV}$.

- Excellent separation of particle identities, particularly for $e^\pm$, $\mu^\pm$, $K^\pm$, $\pi^\pm$, p, $\bar{p}$, covering a large range of momenta.

- Vertex resolution must be able to measure differences in the B decay times. This is also required for vertexing τ and charm events.

- A triggering system is required that will select important physics events, and thus reduce the rate of events that need to be recorded by discarding uninteresting events.

- The detector must be able to operate under conditions of high radiation without detriment to performance.

- The large amount of data which is taken by the detector must be rapidly read out and stored, with little dead time.

The detectors actual performance in quantitative terms is discussed in later sections of this chapter.

The *BABAR* detector is shown in Figure 3.4.

The detector is made up of a number of subdetectors, which are:

- SVT — Silicon Vertex Tracker: Used for vertexing short lived particles such as B mesons.
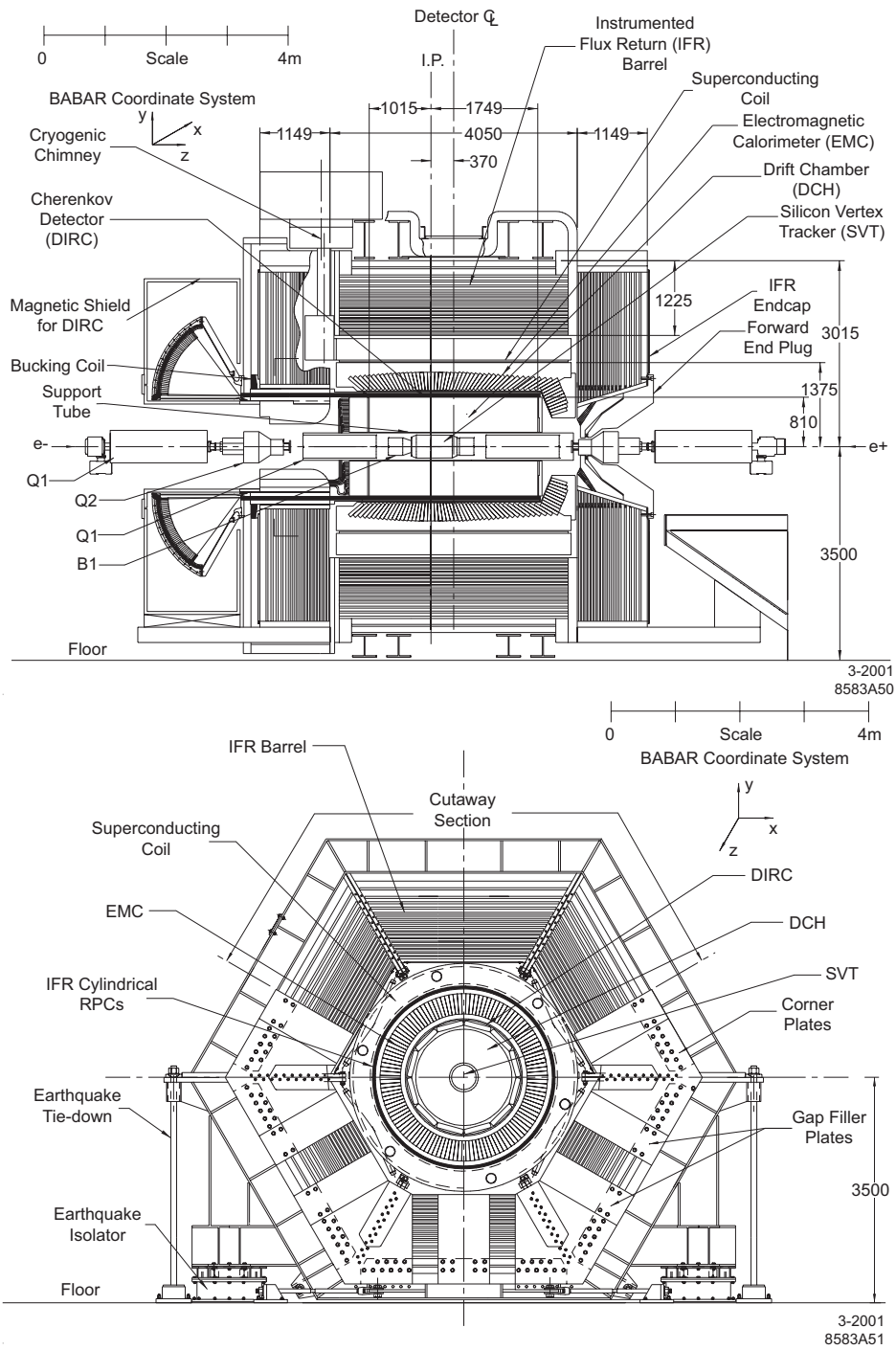
Figure 3.4: The BABAR detector [46].

- DCH — Drift Chamber: The primary tracking system.

- DIRC — Detector of Internally Reflected Cherenkov radiation: Used for particle identification.

- EMC — Electromagnetic Calorimeter: Used for particle energy determination.

- 1.5T Magnet. Used to curve the path of charged particles, allowing for momentum based particle identification.

- IFR — Instrumented Flux Return: Used for detecting muons and neutral hadrons.

Each of these subdetectors are described in detail in the subsequent sections. The terms used to name and describe the subsystems involve a lot of three letter acronyms. Appendix A provides a glossary of these and other related terms.

3.3.1   The *BABAR* Coordinate System

The *BABAR* detector has a well defined coordinate system. Firstly, the z axis is defined as the direction of the drift chamber axis. This is very slightly different from the direction of the electron beam, by 20mrad. The y axis points upwards, and the x axis is horizontal, with the positive x direction being defined as that which points away from the PEP-II ring.

When describing the asymmetric nature of the detector, the forward region is that which lies in the $+z$ direction, and the backward region that which lies in the $-z$ direction.

When discussing particle tracks within the detector, there are five parameters used to characterise them. Each parameter is calculated at the point of closest approach to the z axis:

- z_0 - the distance between the track and the origin along the z axis,

- d_0 - the distance between the origin and the track in the $x - y$ plane,

- ϕ_0 - the azimuthal angle of the track,

- ω - the track curvature, which in terms of the component of the track momentum transverse to the z axis is given by $\omega = 1/p_T$,

- $\tan \lambda$ - The dip angle, λ, is measured with respect to the $x - y$ plane.

The reconstruction of tracks is detailed in section 4.3.1.

3.4   SVT - Silicon Vertex Tracker

The Silicon Vertex tracker is the innermost of the detector subsystems. It is the only subsystem capable of vertexing the tracks originating from the decays of short lived particles, most notably B mesons, but also D mesons and τ leptons. For particles with momenta less than $120 \, \text{MeV}/c$, the SVT provides the only tracking information available, as such particles cannot be reliably recorded with any other subdetectors. The presence of the beam pipe, bending magnets, and cooling systems limits the coverage of the SVT. In terms of the polar angle, it is restricted to between $20.1°$ and $150.2°$, with the better coverage in the forward region. The SVT has to be built of minimal material, to allow particles to pass through to subsequent detectors, whilst still providing excellent tracking. The SVT must also be very radiation hard, as it will be exposed to a lot of radiation, when the machine is operating at high luminosities.

Five layers of silicon strips comprise the SVT. These are shown in Figure 3.5.

Each of the silicon strip detectors is double sided, with the strips on opposite sides running perpendicular to each other, in order to allow measurement of both the ϕ angle, and the z-position. The outer strips of each layer run parallel to the direction of the beam, and it is these that are used for ϕ determination, whilst the inner strips are used to determine z.

The first three layers are each organised into six modules. The two outer layers have more modules. The fourth layer has sixteen modules, and layer five has the most, with eighteen modules. Furthermore, these two outer layers are divided into a and b
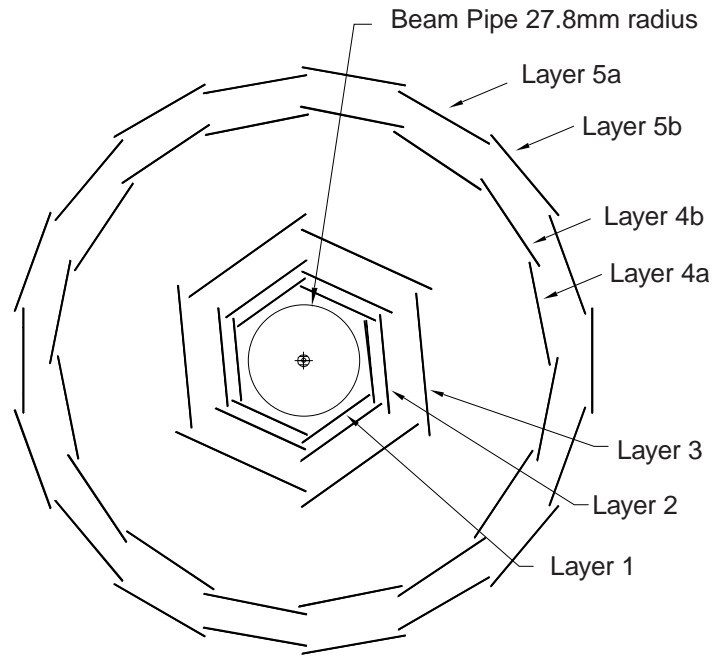
Figure 3.5: Schematic of the SVT as viewed along the *BABAR* *z*-axis [46].
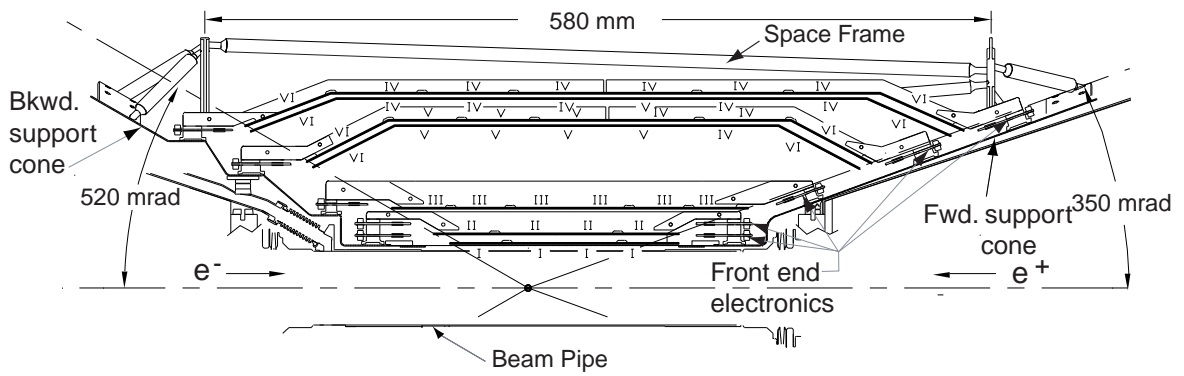
Figure 3.6: The SVT viewed along the *BABAR* *x*-axis [46].

sections, as shown in the figure. These have slightly different radii, and are designed to overlap to cover the maximum solid angle available.

A view of the SVT viewed from the x-axis of the BABAR detector is shown in Figure 3.6.

The alignment of the SVT is very important, because of the precision measurements that need to be made. This is carried out by aligning tracks from dimuon events with the tracks produced in other subsystems, particularly the Drift Chamber. Alignments are also carried out using cosmic rays during global calibration.

In order to study time-dependent CP-violation, precise measurements of the B-vertex need to be made. The resolution required on such measurements was determined to be 80μm from Monte Carlo studies [44]. The actual resolution in the detector is better than 70μm.

The information from the SVT and the DCH are together used for tracking. Tracking performance for both subdetectors is discussed in the following section. Track reconstruction is discussed in section 4.3.1.

3.5 DCH - Drift Chamber

The drift chamber is the principal tracking system for charged particles of the BABAR detector. The tracking data from the drift chamber can be combined with that of the SVT to yield extra information on particle tracks. The DCH can also aid with particle identification by yielding energy loss (dE/dx) information.

The drift chamber is situated outside the SVT. It forms a cylinder of length 2.8m and radius 0.809m, the inner radius (in which the SVT sits) is 0.236m. The cross section of the drift chamber is shown in Figure 3.7. The centre of the cylindrical volume that the drift chamber occupies does not correspond with the interaction point. This is due to the asymmetric nature of the beams, and the drift chamber is shifted in the direction of the beam boost (in the positive z direction).

It is made up of 40 hexagonal cell layers providing spatial and ionisation information
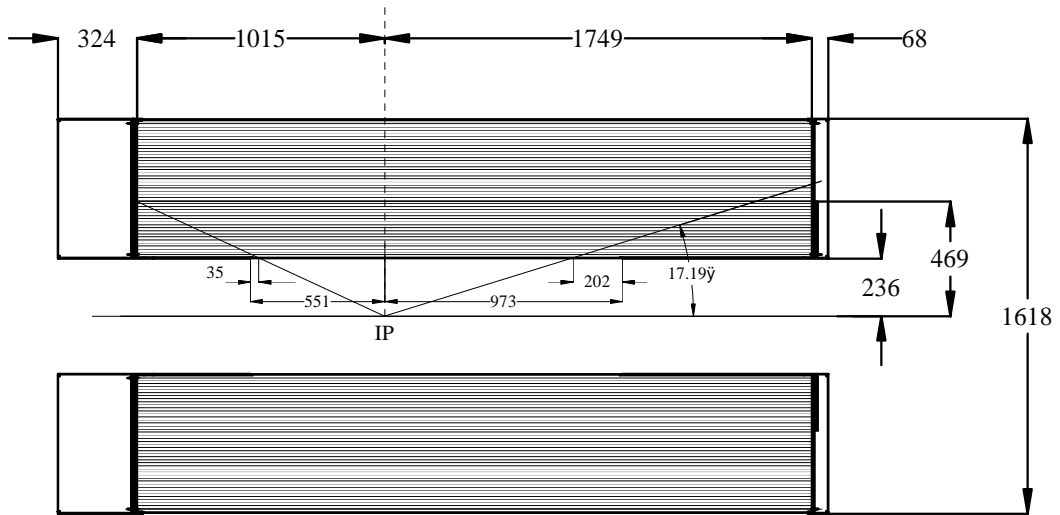
Figure 3.7: Drift Chamber Cross-section — view from along x-axis [44]. Lengths are given in mm.
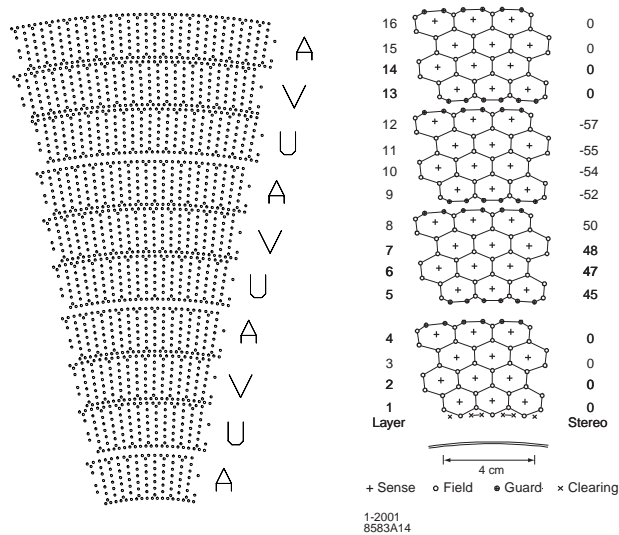
Figure 3.8: (a) The arrangement of layers in the Drift Chamber [44]. (b) The layout of the first four superlayers [46]. Stereo angles are given in mrad.
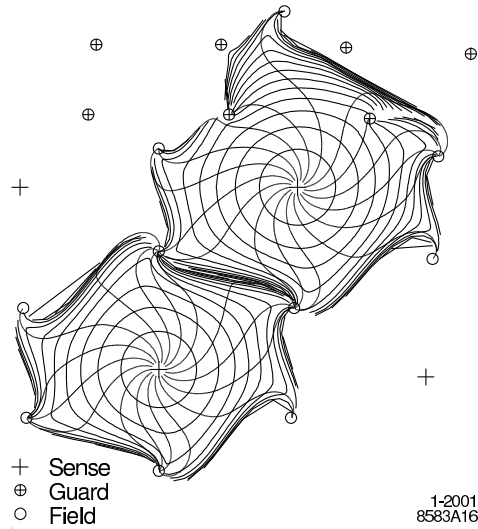
Figure 3.9: Equal drift time contours in the DCH. Contours correspond to 100ns intervals [46].

on charged particles. These can provide up to 40 spatial measurements per track. It contains wires placed at small angles relative to the z-axis, in 24 of the 40 cells, in order to provide longitudinal information.

The 40 layers are divided into 10 superlayers, each consisting of 4 layers. The layers are shown in Figure 3.8(a). The different types of superlayers are axial (A), and stereo (U and V), which are ordered AUVAUVAUVA as shown. Figure 3.8(b) shows the first four of the superlayers in more detail. Here it can be seen that the wires in superlayers 2 and 3 are at a small angle, whereas those in (axial) superlayers 1 and 4 are not. The stereo angle of the wires is shown in the right hand column of numbers, and given in mrad. The stereo angles increase in magnitude from ±45 mrad in superlayer two, up to ±76 mrad in the ninth superlayer.

The drift chamber itself is filled with a gas of helium-isobutane, with a 4:1 composition ratio. This mixture has a very long radiation length (the whole system of both gas mixture and wires gives an aggregate 0.28% of a radiation length for normally incident particles), which helps to prevent multiple scattering. In addition a small
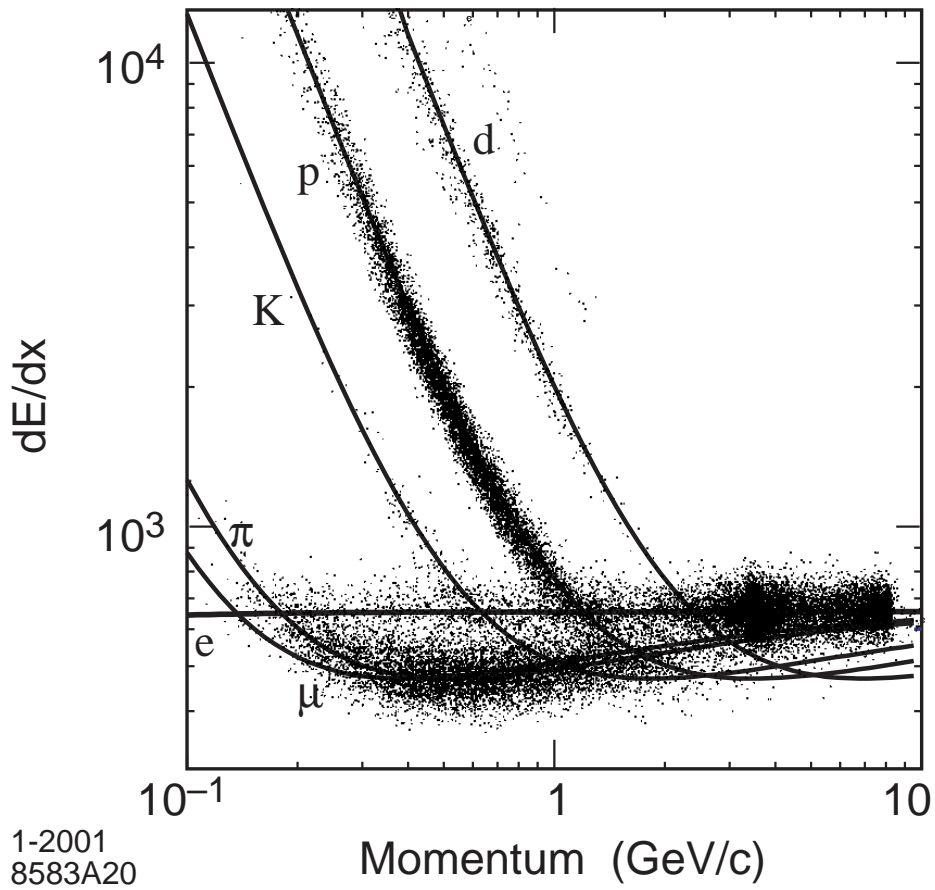
Figure 3.10: dE/dx distributions for electrons, muons, pions, kaons, protons, and deuterium, with superimposed Bethe-Bloch functions [46]. The vertical scale is given in arbitrary units.
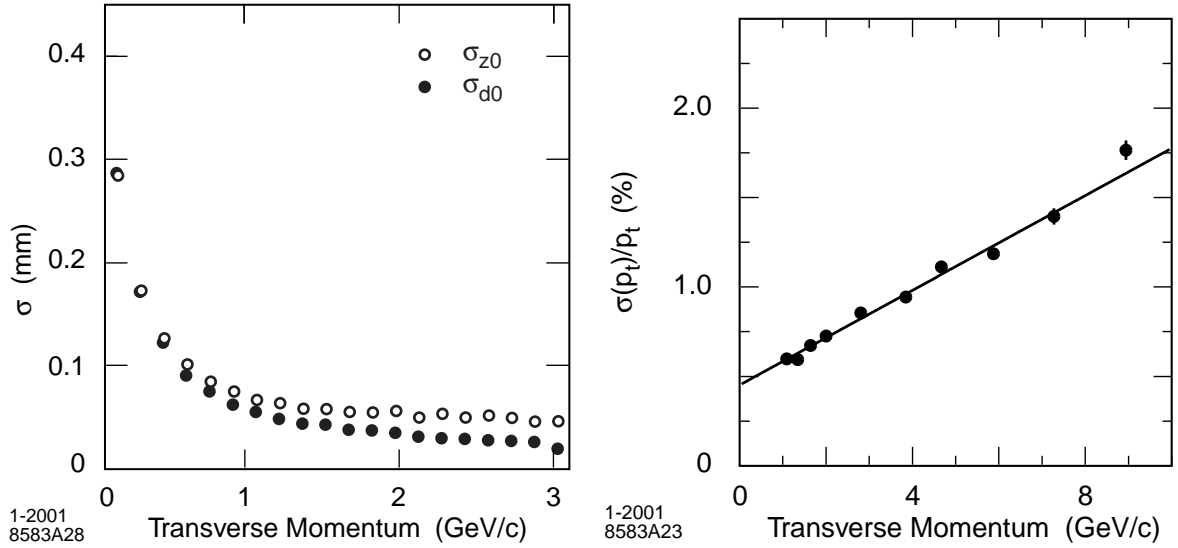
Figure 3.11: Tracking performance as a function of transverse momentum [46]. The left hand plot shows the resolution of z_0 and d_0; the right hand plot shows the resolution of p_T.

amount of water vapour (amounting to about 0.3%) is included in this mixture — this will help to increase the active lifetime of the drift chamber.

The hexagonal cells that make up each layer are shown in Figure 3.9. They consist of a sense wire in the centre, which is surrounded by six field wires, which are grounded. The sense wires are 20μm in diameter, and are made of a gold plated tungsten-rhenium compound. The field wires have diameters of either 80μm or 120μm, and they are composed of gold plated aluminium. The sense wires carry a high voltage — typically 1960V.

Upon passage of a charge carrying particle through the gas, ionisation is caused. The electrons liberated are then accelerated towards the sense wire by the field, which in turn creates an avalanche of charge. At an operating voltage of 1960V the gain is of the order of 5×10^4. The leading edge of the charge avalanche is used to determine the drift time, which has a resolution of 1ns, and this can be used to extract position information. In addition the total charge deposited on the sense wires is used to

determine the energy loss (dE/dx) as the particles traverse the drift chamber.

Figure 3.10 shows the dE/dx distributions for various particles traversing the drift chamber. This plot also has the expected Bethe–Bloch [1] functions plotted. Of particular note is the excellent separation of kaons and pions at lower momenta.

Calibration of the exact relation between drift times and particle properties is determined from dimuon events, and also electron-positron events. The average resolution that can be achieved with a single cell is about 125μm.

The DCH and SVT combine to form the tracking system for *BABAR*. Figure 3.11 shows the resolutions that can be obtained from this tracking system, as a function of particle transverse momentum (p_T). The left hand plot shows the resolution on the track parameters, z_0 and d_0, and the right hand plot shows the resolution of p_T. This is calculated from tracks from cosmic ray muons which traverse both the DCH and SVT.

3.6 DIRC - Detector of Internally Reflected Cherenkov radiation

The main function of the DIRC is in particle identification (PID). It is particularly important in identifying charged hadrons, and provides excellent separation between kaons and pions.

Cherenkov radiation is produced by particles moving faster than the speed of light in a particular medium. The velocity of a particle may be expressed in terms of the standard relativistic variable $\beta = p/E$. For a material with refractive index n, the condition for emission of Cherenkov radiation becomes $\beta > 1/n$. The Cherenkov radiation is emitted at an angle to the momentum vector of the superluminal particle. The cosine of this angle is given by $\cos\theta_C = 1/\beta n$. As many individual photons are emitted from a single particle, these build up a cone of Cherenkov light around the direction the particle traversed.

A cross sectional view of the DIRC is shown in Figure 3.12. The material chosen
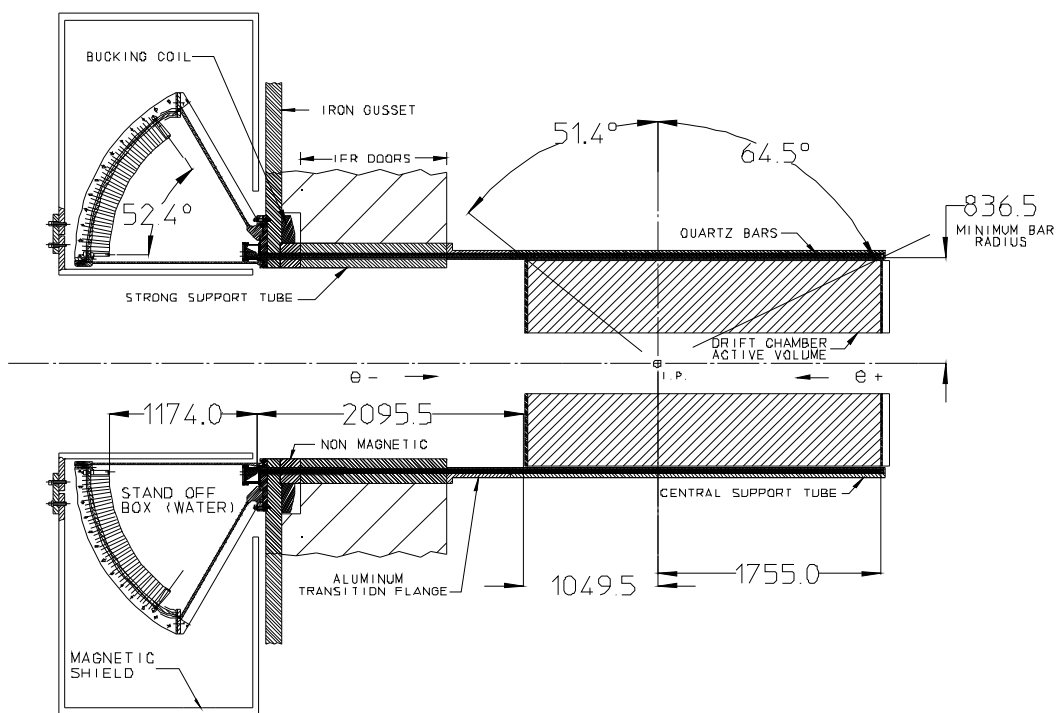
Figure 3.12: Cross sectional view of the DIRC [46]. Lengths are given in mm.
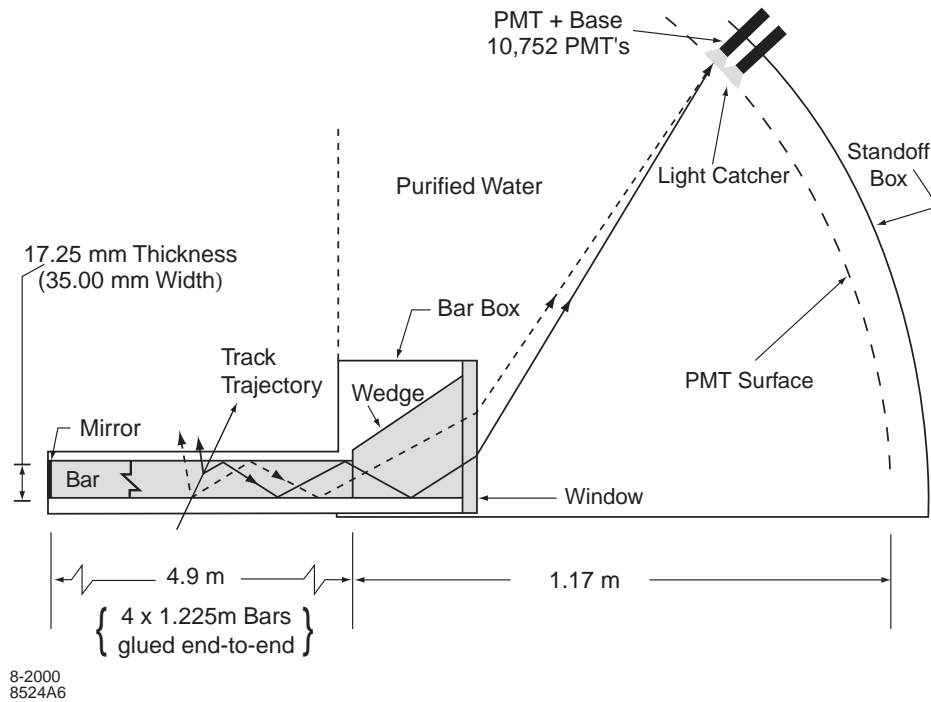
Figure 3.13: Diagram showing DIRC principles of operation [46].

as the medium in which Cherenkov photons will be produced is synthetic fused silica quartz, which has a refractive index $n = 1.472$. A total of 144 bars of this quartz are used, and they are arranged into a dodecagonal barrel surrounding the DCH. The overall thickness of the DIRC resides in only 8cm of radial space between the DCH and the EMC. This corresponds to approximately 17% of a radiation length.

Advantage was taken of the asymmetric nature of the detector, by only placing photodetectors at one end of the detector, this being the backward end of the detector, as this end has less occupancy from other subdetector systems.

Cherenkov light is totally internally reflected within the quartz bars, and thus propagates along the bars to arrive at the detection apparatus. Light which propagates in the forward direction is reflected back by a mirror. Consequently all light will proceed to the DIRC detector, at the backward end of the detector.

When the light has completed its journey through the quartz it enters the Stand

64
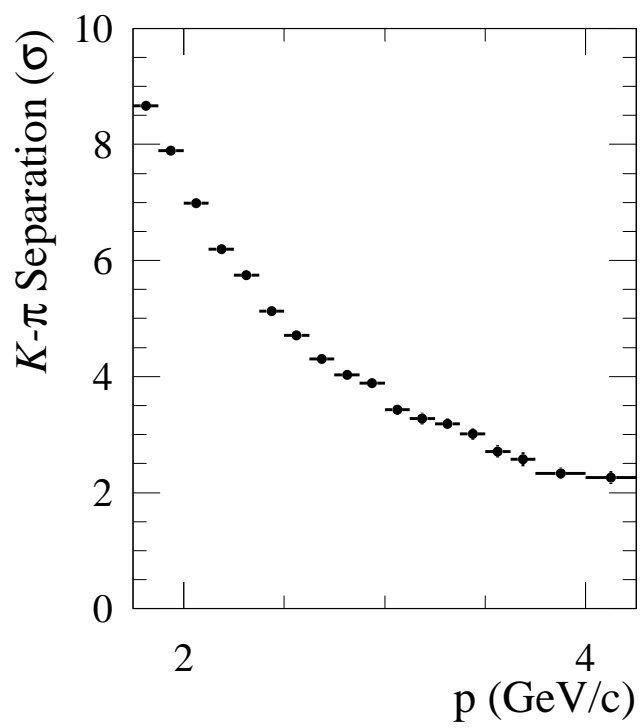
Figure 3.14: Kaon-Pion separation with the DIRC, as a function of momentum.

Off Box (SOB). This is filled with 6,000 litres of ultra-pure water. The water has a refractive index which is close enough to that of the quartz to ameliorate any complication from internal reflection at the interface. Within the water is a fused silica wedge. This will reflect photons which enter the SOB at large angles, and thus reduce the area that needs to be instrumented.

Figure 3.13 shows a schematic view of the DIRC, together with an illustrative path for a typical photon.

The far surface of the SOB is lined with an array of Photomultiplier Tubes (PMTs). These are able to detect photons in the visible and near-UV spectra. Each PMT has a hexagonal light catcher in front of it, to increase the effective active surface area to approximately 90%. Each of the twelve regions of the DIRC contains 896 PMTs, totalling 10752 PMTs in the whole subdetector. Each PMT has diameter of 28.2mm.

Between the SOB, and the main detector body, there is a bucking coil. This is composed of a ten-layered coil of copper, which is water cooled. This, combined with a steel shield that surrounds the SOB, curtails the magnetic field around the PMTs.

The Cherenkov angle information is preserved during the photons' passage, and can be calculated from the signal that is detected by the PMTs (to within a sixteen-fold ambiguity). This information can then be combined with particle tracks, and momentum information, to yield the particle mass. Figure 3.14 shows the separation that can be achieved between kaons and pions using the DIRC. This is dependent on the momentum of the particle, but it can be seen that at momenta of around $3\,\mathrm{GeV}/c$ a separation of 4 standard deviations (σ) is achieved. The important role played by the DIRC in particle identification (PID) is outlined in section 4.4.

3.7   EMC - Electromagnetic Calorimeter

It is necessary for BABAR to measure the energy of photons over a very large range of energies. Many interactions will involve π^0s, which can decay into low energy photons. There are also processes such as $e^+e^- \rightarrow e^+e^-\gamma$ which involve photons with high
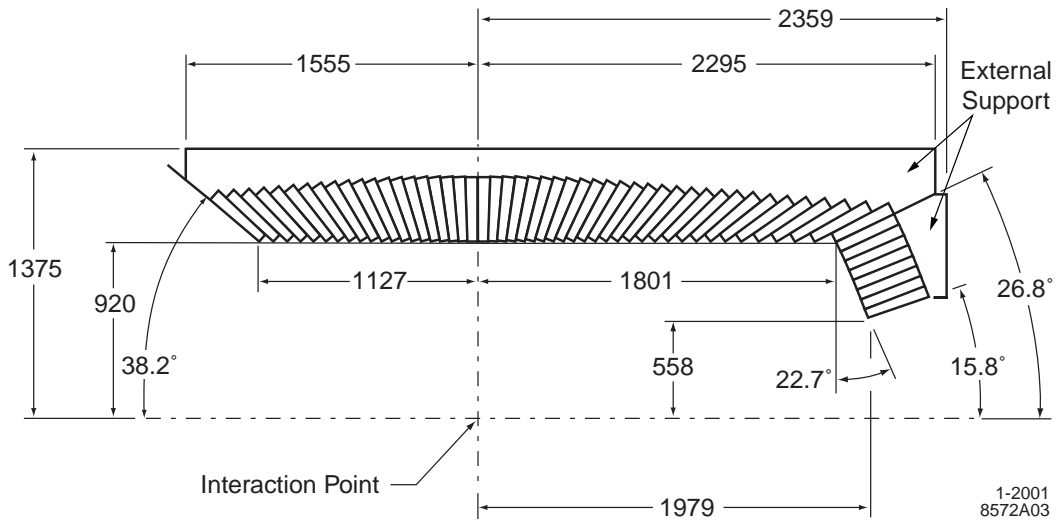
Figure 3.15: EMC geometry [46]. Lengths are given in mm.

energies. For these reasons the Electromagnetic Calorimeter (EMC) was designed to be sensitive to photon energies over the large range from 20 MeV up to 9 GeV. The calorimeter is also used for electron identification and measurements.

The EMC is made from 6580 Thallium doped Caesium Iodide crystals, CsI(Tl). The choice of CsI(Tl) was made because it has a small Molière radius, and also a high light yield, which are ideal for providing the necessary resolution. The layout of these crystals is shown in Figure 3.15. The crystals form a barrel section, and also a forward endcap — no backward endcap is used, or required, due to the asymmetric nature of the colliding beams.

The barrel consists of 5760 crystals, which are arranged in 48 rings, each comprising 120 individual crystals. The end cap is made up of 8 rings. These vary in size from 120 crystals in the outer 3 rings, 100 in the next two, and finally 80 crystals in the innermost 2 rings, to account for the remaining 820 crystals. Figure 3.16 shows how the crystals in the barrel fit together.

The structure of the crystals themselves is shown in Figure 3.17. The crystals vary in height between 29.6cm and 32.4cm, corresponding to between 16 and 17.5
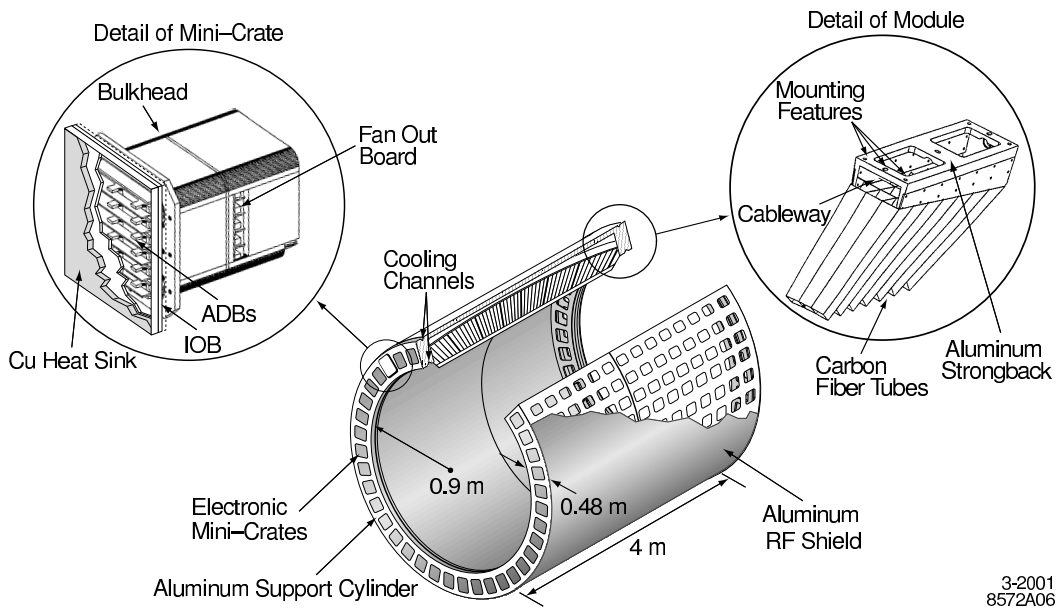
Figure 3.16: EMC structure [46].

radiation lengths, so that an electromagnetic shower will be mostly contained within the crystals. The crystals have silicon diodes at the top which read out the signal, and pass it on to further electronics.

Most electromagnetic showers will cover several crystals, as many charged particles make up an electromagnetic shower. The crystals scintillate upon passage of charged particles. The signals from crystals are added together to form clusters, marking the energy deposition from a single shower. Crystals must have an energy deposition of greater than $1 \, \text{MeV}$ to be included in the clustering algorithms.

Clusters can then be related to tracks recorded in the inner subdetectors, with those clusters that do not correspond to any of the observed tracks assumed to arise from the passage of neutral particles.

The calibration of the energy measurements and resolution is done using ^{16}N, which is a radioactive element that emits photons with an energy of $6.1 \, \text{MeV}$. Bhabha events are used to provide the calibration at higher energies.

It is usual to parametrise the energy resolution via the function:
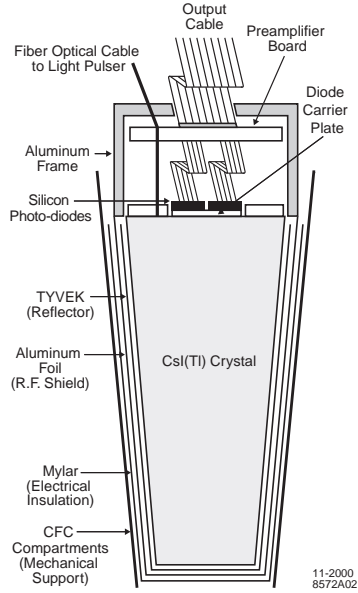
Figure 3.17: Schematic diagram of a CsI(Tl) crystal [46].

$$\frac{\sigma_E}{E} = \frac{a}{\sqrt[4]{E}} \oplus b \tag{3.1}$$

where $a = (2.32 \pm 0.30)\%$, $b = (1.85 \pm 0.12)\%$, and the quantities are added in quadrature. The energy is measured in GeV.

In addition the angular resolution is modelled as:

$$\sigma_\theta = \sigma_\phi = \frac{c}{\sqrt{E}} + d \tag{3.2}$$

where $c = 3.87 \pm 0.07$ mrad, and $d = 0.00 \pm 0.04$ mrad, and E is again measured in GeV.

Figure 3.18 shows the energy and angular resolutions of the EMC, as a function of photon energy, measured using $\pi^0 \rightarrow \gamma\gamma$, and other processes. The solid curves are the the fits to the above equations, and the dashed curves are MC. The energy resolution plot also has curves representing the RMS of the fit.
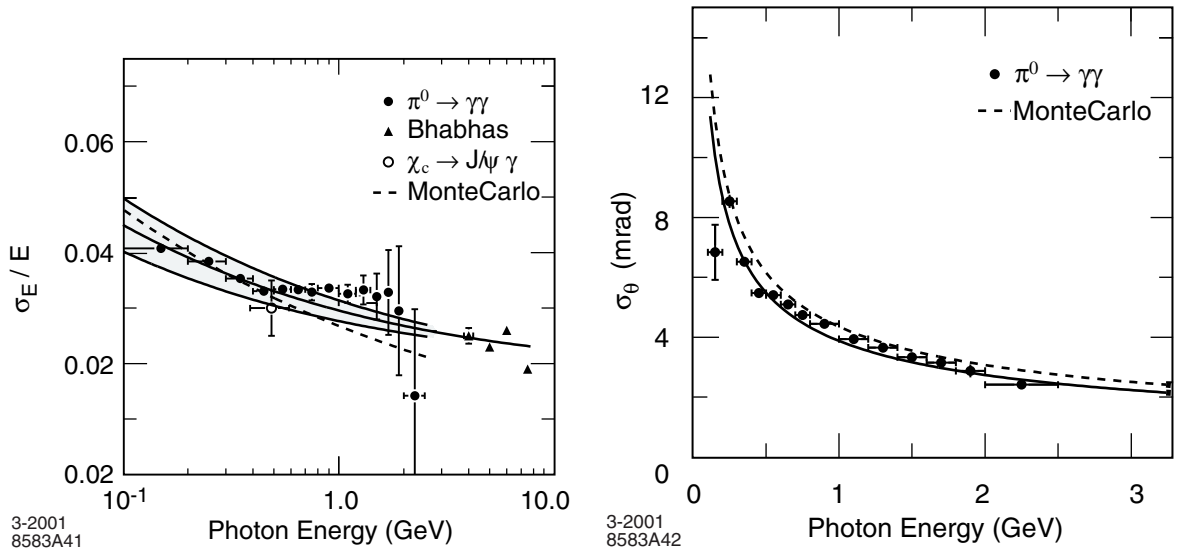
Figure 3.18: EMC performance as a function of photon energy [46]. The left hand plot shows the energy resolution; the right hand plot shows the angular resolution.

3.8 Solenoid

Between the EMC and the Instrumented Flux Return is a superconducting solenoidal magnet. This is used to produce a 1.5T magnetic field along the z axis. It is required for particle identification and momentum measurements, due to the curvature it induces in the paths of charged particles.

3.9 IFR - Instrumented Flux Return

Sitting outside the magnet, the IFR is the outermost of the detector subsystems. In addition to its particle detection mandate, it serves as a flux return for the Solenoid, and also forms part of the *BABAR* support structure.

The IFR is the primary detector for identifying muons, which play an important role in identifying decays such as $B^0 \rightarrow J/\psi\, K_s^0$, where the J/ψ decays to $\mu^+\mu^-$. The IFR is also used to identify neutral hadrons, such as K_L^0.

The structure of the IFR is shown in Figure 3.19. The particle detection in the IFR
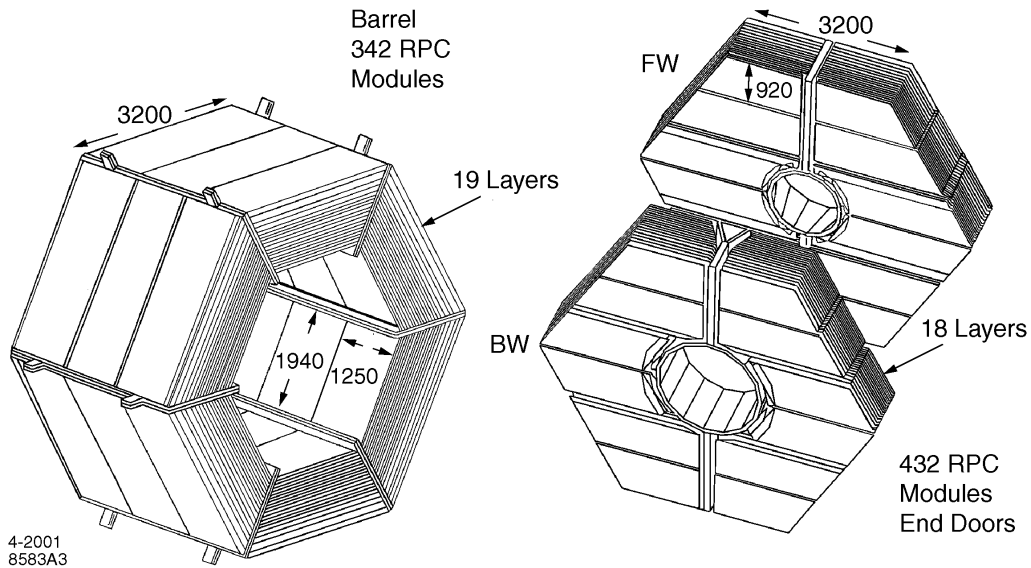
Figure 3.19: IFR structure [46]. FW is the forward end door, and BW is the backward end door. Lengths are given in mm.

is performed by Resistive Plate Chambers (RPCs). Differently shaped RPCs are used in different places around the IFR, which forms a barrel, and forward and backward endcaps.

There are 18 layers of RPCs in the endcaps. In the barrel there are 19 RPC layers, plus there are two supplementary layers of RPCs placed between the EMC and the magnet — these aid in matching tracks between the EMC and the IFR itself.

Figure 3.20 shows the layout of one of the RPCs. There are two graphite electrodes, one of which if held at a voltage of 8kV, whilst the other is grounded. Inside these there are two 2mm thick sheets of Bakelite, and between these there is a 2mm thick volume, filled with a gas mixture, comprising 57% Argon, 39% Freon-134a, and 4% Isobutane, which is non-flammable.

Figure 3.21 shows the IFR performance, in terms of muon detection efficiency and the probability of misidentification of pions as muons. This is shown as a function of particle momentum, and of polar angle. The performance of the IFR is measured
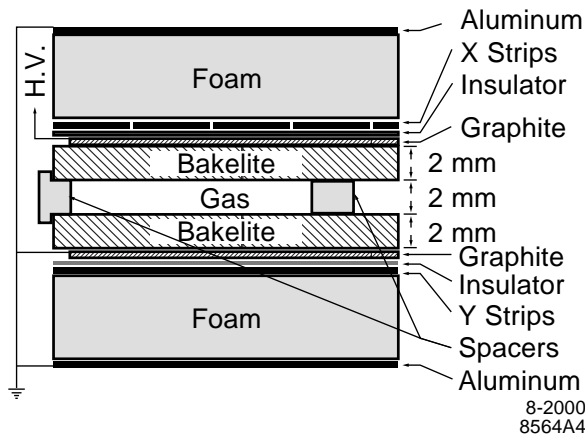
Figure 3.20: Structure of one of the IFR RPCs, and the high voltage (HV) connection [46].

using muons originating from cosmic rays. The initial performance of the RPCs was very good with most achieving efficiencies of over 90%. However the performance of the RPCs has deteriorated over time, with many of the RPCs now being classified as dead (efficiency less than 10%).

3.9.1 LSTs - Limited Streamer Tubes

Due to the deteriorating performance of the IFR RPCs, replacement was necessary, as the existing RPCs would not last the lifetime of the experiment. A new system of Limited Streamer Tubes (LSTs) was designed, and these will eventually replace all the RPCs. The installation of all the LSTs is planned to be completed during a shut-down period in the second half of 2006.
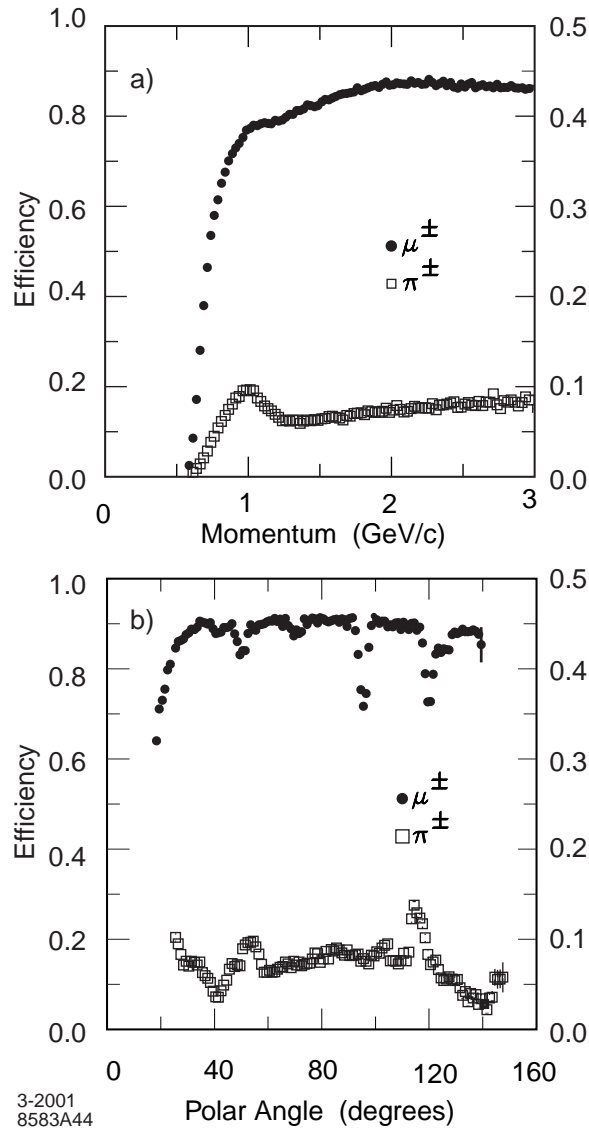
Figure 3.21: IFR muon efficiency (left scale) and pion misidentification probability (right scale) [46]. These quantities are plotted as functions of: a) momentum in the laboratory frame; b) polar angle for particles with momentum $1.5 < p < 3.0\,\mathrm{GeV}/c$.

3.10 Trigger

The *BABAR* trigger is important for reducing the rate at which data are produced by the detector to a level where they can all be accurately recorded, whilst at the same time ensuring that as many events as possible of physical interest are preserved.

There are two aspects to the trigger. The first is the level 1 trigger, which is hardware based, and the level 3 trigger is based on software.

3.10.1 Level 1 Trigger

The level 1 trigger (L1T) is the first of the *BABAR* triggers, and its decision making is enacted by hardware for efficiency reasons. The typical rate of events output by the L1T is 1kHz. The trigger is divided into several triggers from different subsystems, these are the Drift Chamber Trigger (DCT), the Electromagnetic Calorimeter Trigger (EMT), and the IFR Trigger (IFT). Information from the SVT cannot be processed rapidly enough to be used in this trigger system.

Each of these Triggers will send trigger primitives to a higher level trigger. These primitives tell higher level triggers if a certain criterion has been passed. For the DCT there are three trigger criteria: Short tracks with $p > 120\,\mathrm{MeV}/c$, reaching DCH superlayer 5; Long tracks with $p > 180\,\mathrm{MeV}/c$ reaching DCH superlayer 10; and high p_T tracks: $p_T > 800\,\mathrm{MeV}/c$. The EMT uses five trigger primitives, these are derived from towers, which are groups of crystals. The threshold energy for towers to trigger is adjustable. Two of the triggers relate to specific parts of the detector geometry, one to the forward endcap, and one to the backward barrel. The IFT is used for triggering $\mu^+\mu^-$ pairs, and for cosmic rays.

The signals from these triggers are combined into a trigger line, by the Global Trigger (GLT). If the GLT receives an accept from a trigger primitive from the subdetector triggers, then the GLT gives an L1 accept, and the subdetectors output their data to buffers, where it is available for the level 3 trigger.

The DCT and EMT receive raw data 2 μs after a collision. They take 4-5 μs

processing the raw data, and GLT takes a further $\sim 3\mu$s of processing time, before it can send an L1 accept to the readout modules (ROMs), taking 1 μs to reach them. This all takes place within the 12.8 μs Front End Electronics (FEE) buffer capacity limit.

It is also possible for L1 accepts to be triggered by the Fast Control and Timing System (FCTS), which can ensure that a prescaled number of events are passed by the L1T, and it can also omit individual subdetector triggers from the decision making process.

3.10.2   Level 3 Trigger

The Level 3 trigger (L3T) further reduces the data rate from 1kHz to around 120Hz, and any events that pass this trigger are read out and permanently stored for physics analysis.

Unlike the L1T, the L3T has access to information from all the subdetector systems, including the output of the L1T processors. Track finding and clustering algorithms are run, and events can be selected or rejected based on track momenta and/or the energy of clusters. Some events consistent with Bhabha events may also be rejected, even if they fulfil other criteria.

The L3T takes an average processing time of 8.5 ms per event per computer used. The output rate for interesting physics events is 16Hz, which comprises hadronic events, and τ and μ pair production. Background events arising from, for example, Bhabha events take the total accepted rate for physics events to 73Hz. The total used for calibration and diagnostics is 49Hz. These figures are calculated for a luminosity of 2.6×10^{33}cm^{-2}s^{-1}. The total rate is limited to about 120Hz by the processing capacity and writing data to storage. Events which receive an L3T accept, are written out from the buffers and stored permanently.
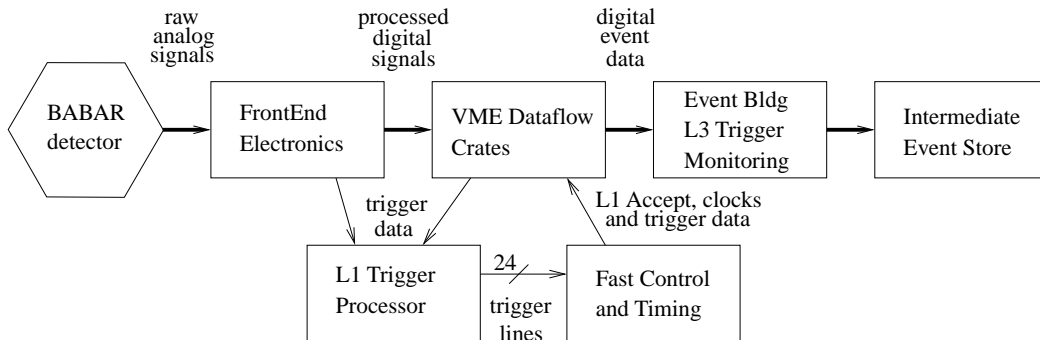
Figure 3.22: Schematic diagram of the *BABAR* DAQ system [46].

3.11 DAQ — Data Acquisition

The Data Acquisition (DAQ) system is the means by which the detector, the triggering system, and the *BABAR* analysis computing structure are linked.

The organisation of the DAQ is shown in Figure 3.22. The DAQ system starts with the readouts from the front end electronics, which pass data onto the L1T, and assuming the trigger is activated, the data pass through the data flow crate buffers to the L3T, where upon being selected, the data are all written to disk and recorded in the event store. The DAQ system can also interface with the trigger systems to enable calibration and testing to take place. The conditions of the detector are also measured and stored. These can include luminosities and beam currents, gas supply purity, the status of the high voltage supply, etc. These are stored in the conditions database and can be associated with the events taken at that time. The conditions are also used in the generation of Monte Carlo simulated events (section 4.1.1).

3.12 Online Prompt Reconstruction and Data Quality

The data that are written out to disk are then processed by the Online Prompt Reconstruction (OPR) Software. This takes the raw data, such as subdetector hits, and

converts them into physical quantities to be used in analysis, such as particle energies and momenta.

OPR is divided into two stages — the first is Prompt Calibration (PC), and the second is Event Reconstruction (ER).

PC is the first stage of processing the data go through. There are four computer farms dedicated to PC, all of which are based at SLAC. ER is the subsequent processing of the data. Ten computer farms are used in ER, which are split between SLAC, and Padova, Italy. PC takes a subset of data to reconstruct, to check for any obvious problems, and calibration is also carried out. The ER process takes longer to complete, and reconstructs every event in the sample. In both PC and ER, the data quality is monitored, by the Data Quality Group (DQG). This group consists of experts on each of the subsystems, who check that the event distributions within each system, such as mean energy deposition within calorimeter crystals, are within acceptable bounds, and that data have not been lost due to detector failures, or distorted by high backgrounds, or other factors. When the *BABAR* reconstruction software is modified or rewritten the data are reprocessed in PC and ER, and each processing has to be checked by the subsystem experts of the DQG. Only data that are passed as Usable For Physics by the DQG are used in physics analyses.

Chapter 4

Particle Identification, Event Reconstruction and Selection

4.1 Data Sample

The data used in this analysis are those collected during Runs 1-4 of the _BABAR_ experiment, between 1999 and the summer of 2004. These data amount to an integrated luminosity of $210.6\,\mathrm{fb}^{-1}$ collected when running at a centre of mass energy of $10.58\,\mathrm{GeV}$, corresponding to the mass of the $\Upsilon(4S)$. Such data are termed on-resonance, and contain approximately 232 million pairs of $B\overline{B}$ mesons [47], amongst many other particles.

In addition to this, $21.6\,\mathrm{fb}^{-1}$ of data were collected while running at a centre of mass energy $40\,\mathrm{MeV}$ below the $\Upsilon(4S)$ mass. These off-resonance data should not contain $B\overline{B}$ pairs, and are thus used for studying the potential backgrounds encountered. The off-resonance data are composed of events arising from the processes $e^+e^- \to q\bar{q}$ (where $q = u, d, s, c$), $e^+e^- \to l^+l^-$ (where $l = e, \mu, \tau$), and subsequent evolution of such processes (for example, hadronisation and emission of photons). The on-resonance data contain all of these processes, but also include the important (for B physics) process $e^+e^- \to \Upsilon(4S) \to B\overline{B}$. Backgrounds arising from processes that

do not involve the $\Upsilon(4S)$ resonance (or equivalently B mesons) are called continuum backgrounds.

Extensive use is also made of Monte Carlo (MC) event samples. Large samples of simulated data are generated for generic decays, and also exclusive samples for all decay modes that have to be examined in any analysis.

4.1.1 Monte Carlo Simulation

In order to test the analysis procedures used by *BABAR* it is necessary to make use of simulated or Monte Carlo events. Two types of MC will be discussed in this document:

- Full MC

- Toy MC

Full MC events are generated on a collaboration-wide basis at the many *BABAR* computing centres. They include a comprehensive simulation of the physical processes that take place, and of the detector's capabilities in recording and reconstructing these events. To simulate the decays of B mesons the `EvtGen` package [48] [49] is used, and `JETSET`[50] is used for simulation of continuum events. These generators produce an output in the form of 4-momentum vectors for each simulated particle, and also include the decay vertices for all particle decays. This output is then used as input into a `GEANT4` [51] simulation, which includes the detector geometry, and the efficiencies of the various subsystems. This involves modelling how the 4-momentum of a particle will be transformed by its passage through matter (the detector), and how the kinetic energy of a particle will be deposited into the various subsystem elements. Thus the detector simulation will produce an output in the form of hits, and energy deposition clusters, that can be used as input to reconstruction software, in the same manner as are data.

The MC events that are reconstructed are stored in exactly the same format as are data, with the addition that MC events also include "truth" information. This

includes information from the generator about the properties with which particles were generated, before the modelling of detector effects.

In order that the detector is accurately modelled during its entire operational period the simulation is performed using running conditions and configuration settings taken from the BABAR detector, which change temporally. A number of working groups undertake validation tests of the MC [48], comparing it to data, and noting any discrepancies and corrections that should be made.

Toy MC is not a full physics simulation. Instead it uses the distributions expected to be observed (Gaussian, Breit–Wigner etc) to generate events. Three-body events are generated as a pair of invariant mass squared values (e.g. m_{13}^2, m_{23}^2) within the Dalitz plot phase space. An amplitude for such an event is then calculated, from the lineshapes used, resonances implemented, and background distributions and fractions. This amplitude will vary depending on the position of the event within the Dalitz plot, and the values chosen for the magnitudes and phases of each resonant (or non resonant) contribution.

The generated event is then accepted or rejected based on the comparison of the calculated amplitude with a maximum amplitude parameter. This parameter can be tuned for efficiency of generation. If it is lower than the amplitude values that can arise from generated events, then the toy MC will be biased, and cannot be used. If it is too high then a very large number of potential events will be rejected, and the generation is inefficient.

The generation of events continues until a pre-set number of events have been accepted. Toy MC is significantly faster to generate than Full MC, and thus a wide range of different models for possible experimental configurations can be tested. Toy MC is also useful for fit validation and investigation of any potential fit biases.

4.2 m_{ES} and ΔE

Extensive use is made in *BABAR* analyses of B meson decays of two kinematic variables that assist in identification of B candidates — they are named the beam energy-substituted mass (m_{ES}) and the energy difference ΔE. These are defined as follows:

$$m_{\mathrm{ES}} = \sqrt{\frac{s}{4} - p_B^{*2}} \tag{4.1}$$

$$\Delta E = E_B^* - \frac{\sqrt{s}}{2} \tag{4.2}$$

where E_B^* is the energy of the B candidate, and p_B^* is the momentum of the B candidate, both calculated in the centre of mass frame, and $\sqrt{s}/2$ is the beam energy, also in the centre of mass frame.

For real B events ΔE is expected to peak at 0, and the m_{ES} distribution would be expected to peak around the B mass, $m_B = 5.279\,\mathrm{GeV}/c^2$. There is only a small correlation between the two variables. Plots of the ΔE-m_{ES} plane are useful for demonstrating the presence of signal events against background events. Such a plot is shown in section 5.3.

4.3 Track and Cluster Reconstruction

4.3.1 Track Reconstruction

The reconstruction of tracks is performed using information from the two innermost sub-detectors, the SVT and the DCH. The first track finding algorithm is performed by the L3T. This is used as an input to the more complex tracking algorithms used during OPR. There are five parameters used to characterise tracks, listed in section 3.3.1.

Tracks found by the level 3 trigger are refitted in OPR, and more hits in the DCH that could belong to one of these tracks, can be added at this stage. In addition a fit is carried out on remaining hits — this is to find tracks which fail to traverse the width of the DCH, or tracks which do not emanate from the interaction point.

Following DCH track reconstruction, information from the SVT sub-detector is used. The extrapolation of DCH tracks into the SVT volume is performed, and any consistent SVT hits are combined with these tracks. Any tracks from low momentum particles which did not reach the DCH are found by a final track fit to the remaining SVT hits.

4.3.2   Energy Cluster Reconstruction

Measurements of the energy of EM particles are made using the EMC. The shower of particles caused by the passage of a charged particle will deposit energy in many different detector crystals. The cluster finding algorithms attempt to group the many individual crystal depositions into clusters of hits deriving from a single shower. The first stage is to find crystals that have a large amount of energy deposited in them (over 10 MeV), and then combine these with neighbouring energised crystals. Further crystals are added until no cluster candidate crystals remain.

An algorithm is then run to find whether a cluster derives from one particle shower, or could have derived from more than one. Where this is the case, a calculation is made of the most likely separation of the showers. Energy clusters can then be matched up with tracks from the SVT and DCH. Any clusters that are not associated with a track are postulated to have arisen from neutral particles.

4.3.3   Vertexing

Vertexing refers to the process that reconstructs the decay vertex of a particle, from the properties of the daughter particles. The very short lived particles known as resonances (such as $\phi(1020)$, χ_{c0}) do not live long enough to travel a distance that can be measured, and hence their decay vertices are not distinguishable from the decay vertices of their parents.

Vertexing is carried out for particles that are stable enough to travel a distance that can be measured before decay. It is primarily used for B mesons. Charged B mesons

have a mean lifetime $\tau_{B^{\pm}} = (1.671 \pm 0.018) \times 10^{-12}$ s [1], which gives $c\tau = 501\mu$m. For a B meson at rest in the centre of mass frame the relativistic boost in the $+z$ direction gives $\beta\gamma c\tau = 280\mu$m in the lab frame, as an estimate of how far a B meson will travel.

Vertexing is used for other short lived particles, such as D mesons, and for neutral particles, such as K_S^0, which can travel far enough to decay within the tracking sections of the detector, but leave no track themselves.

The vertexing algorithms initially estimate the vertex as the primary interaction point. The algorithms have a convergence radius of a few cm, so this works well for B decays, but requires refinement for longer lived particles. BABAR uses a vertexing algorithm called `GeoKin` [52], which uses a generalised least squares method using the Lagrange Multiplier technique. `GeoKin` fits involve both a geometric component, and a kinematic component, which involves ensuring that tracks arising from the same vertex, conserve momentum at the vertex.

The reconstructed properties of daughter particles are affected by the detector's resolution. For a three body B meson decay, this can lead to events where the calculated invariant masses of pairs of daughters lie outside the kinematic boundary (section 2.8.1) of the allowed phase space of the Dalitz plot. This can also be caused by final state radiation (FSR). To ameliorate this effect, and to improve the resolution, the vertex fit is run again, with the constraint that the invariant masses must sum to the mass of a B meson.

4.4 Particle Identification

Particle Identification (PID) is carried out after track and cluster reconstruction. It uses these sources, together with measurements of dE/dx and information from the DIRC to identify the most likely identity of a particle. BABAR has physics tools groups that have developed standard selectors for PID [53]. Five types of particle have associated PID selectors, these are: muons, electrons, pions, kaons, and protons.

The selectors of principal interest in this analysis are the kaon selectors, in particular `KaonSMSSelector` [54], for which there are five levels of selection, each of which has a different efficiency for identifying signal, with lower efficiency selections resulting in higher purity (better signal to background ratio). The five different selection levels are `VeryTight`, `Tight`, `NotAPion`, `Loose`, `VeryLoose`.

The kaon selectors make use of measurements from the DIRC, SVT, DCH, and dE/dx. The DIRC is a very important tool for separation of pions and kaons. Use is made of both the observed Cherenkov angle, and of the number of Cherenkov photons recorded.

In order for Cherenkov radiation to be emitted due to the passage of a charged particle, the particle must have a minimum momentum given by:

$$p > \frac{m}{\sqrt{n^2 - 1}}, \tag{4.3}$$

where m is the mass of the particle, and n is the refractive index of the material. The refractive index of the quartz used in the DIRC is $n = 1.473$, which gives a kaon threshold momentum of $p = 0.46 \, \text{GeV}/c$.

The expected number of photons emitted by the passage of a particle is stored in a look-up table. The number is a function of the type of particle, its charge, momentum and polar angle, and also through which quartz bar it passed.

The momentum of a particle determines which subdetectors provide the best separation. The following ranges of momenta are used by the `KaonSMSSelector`, using the `Tight` mode.

- SVT: $0.025 < p < 0.7 \, \text{GeV}/c$.

- DCH: $0.090 < p < 0.7 \, \text{GeV}/c$.

- DIRC: $0.6 < p < 10 \, \text{GeV}/c$.

Thus for low momentum particles dE/dx information from the SVT and DCH is the only source of PID, and for high momentum particles the DIRC is the source of PID.

For each particle that passes through the detector a likelihood is calculated for it to be one of five species (e, μ, π, K, p). The pion likelihood, l_π, and the kaon likelihood, l_K, are of principal use in the criteria for selection in this analysis.

The DIRC likelihood is composed of two parts, which are mostly uncorrelated. The first part is a Gaussian. The expected Cherenkov angle is known for different species, and the observed probability density function for a given species is a Gaussian centred on the expected angle. Thus a probability g_i can be calculated for each particle hypothesis. The ratio of probabilities can then be used as a criterion to separate species. For example $g_K/g_\pi > r$ would be used to separate kaons and pions, where r is a parameter to be chosen, to give different purities for the selection.

The second part of the likelihood is a Poisson probability distribution, p_i, which is calculated based on the number of photons observed and the number of photons expected from the look-up tables. The total likelihood is given by the product of these two likelihoods: $l_i = g_i p_i / \sum g_j p_j$, where the sum is over all five species.

The likelihood cuts used by `KaonSMSSelector` in `Tight` mode are:

- $p < 2.7\,\text{GeV}/c$: $l_K > l_\pi$.

- $p > 2.7\,\text{GeV}/c$: $l_K > 80 l_\pi$.

- $0.5 < p < 0.7\,\text{GeV}/c$: $l_K > 15 l_\pi$.

- Proton likelihood cut: $l_K > l_p$.

These criteria are optimised to obtain a mis-identification rate below 5% for particle momenta up to $4\,\text{GeV}/c$. The kaon-pion separation achieved by the DIRC is shown in figure 3.14.

4.5   Preselection of Events

The first level of selection for the $B^\pm \to K^\pm K^\pm K^\mp$ candidates uses very general criteria to select events of interest.

Firstly any tracks that may be used to make up an event must pass the predetermined `GoodTracksLoose` criteria. These are:

- The momentum of the track must be no more than $10\,\mathrm{GeV}/c$.

- The transverse component of the momentum, p_T, must be at least $0.1\,\mathrm{GeV}/c$.

- The Distance Of Closest Approach (DOCA) of the track to the z axis, d_0, in the $x - y$ plane of the detector must be no greater than 1.5 cm.

- In the direction of the $z-$axis the DOCA, z_0, must not be in excess of 10.0 cm.

- The number of hits in the drift chamber used in the track reconstruction must be at least 12.

For each reconstructed candidate for B meson status, these conditions are required:

- The number of tracks in the event must be 4 or greater, which is a necessary and sufficient condition to ensure that the counterpart $\bar{B}$ of the candidate B meson, has at least one track arising from its decay.

- As a very basic check, the total energy of the whole event is required to amount to less than $20\,\mathrm{GeV}$.

- The value of m_{ES} is required to be within $0.1\,\mathrm{GeV}/c^2$ of m_B.

- The value of ΔE must lie between $-0.45\,\mathrm{GeV}$ and $0.45\,\mathrm{GeV}$.

- The total charge of the candidate B must equal either $+1$ or -1.

4.6 Further Selection

The `NonCharm3BodyUser` [55] package is used to process the preselected events, and produce data files in a format that can be analysed using the `Root` [56] analysis programme. The output from `NonCharm3BodyUser` is suitable for analysing all of the

charged decay modes $B^\pm \rightarrow h^\pm h^\pm h^\mp$, where $h = \pi, K$. `NonCharm3BodyUser` uses many standard *BABAR* analysis tools to apply a number of selection criteria:

- ΔE and m_{ES} are recalculated following the vertexing of possible candidate B mesons.

- Vertexing of candidates is then performed for a second time, with the B mass constraint applied (section 4.3.3).

- PID selectors are run for all tracks. The Kaon selector is explained in section 4.4.

- Parameters based on the topology of the events are calculated — these event shape variables are discussed in section 5.5.

- The magnitude of ΔE must have a maximum value of $0.35\,\mathrm{GeV}$. This requirement is fulfilled if it is true for any candidate in the event.

- A cut is placed on the angle between the B candidate's thrust axis, and the thrust axis of the rest of the event (section 5.5). The absolute value of the cosine of this angle must not be greater than 0.95.

4.7   Final Selection

The output data files from `NonCharm3BodyUser` are then further refined using the `CharmlessFitter` [57] package, a `RooFit` [58] based fitting package, used to apply the final selection criteria. This takes data that are general for all $B^\pm \rightarrow h^\pm h^\pm h^\mp$ modes, and produces data files containing only data for use in the $B^\pm \rightarrow K^\pm K^\pm K^\mp$ analysis.

The selection criteria applied by `CharmlessFitter` are:

- The candidate must have a valid Kinematic fit for a $K^\pm K^\pm K^\mp$ track hypothesis.

- All tracks must pass kaon selectors run in `Tight` mode.

- All tracks must fail electron selectors in `Tight` mode.

- A cut is placed on the thrust angle (section 5.5): $|\cos\theta_T| < 0.9$.

- A cut is placed on the Fisher discriminant (section 5.5.1): $\mathcal{F} > -0.71$.

- The value of m_{ES} must be less than the energy of the beam, $\sqrt{s}/2 = 5.29\,\mathrm{GeV}$.

- A width for the ΔE cut is chosen to be approximately 3σ of the ΔE distribution. The 3σ window corresponds to $\pm 0.06\,\mathrm{GeV}$. A study was made with a control sample of $B^+ \to \overline{D}^0\pi^+$ events, which found a shift of $-8.3\,\mathrm{MeV}$, which is applied to the selection window to give a ΔE cut of:
  $$-0.0683 < \Delta E < 0.0517\,\mathrm{GeV}.$$

- If there are multiple candidates for a single event, one is chosen at random.

- The background from the D meson decay; $B^+ \to \overline{D}^0 K^+$, $\overline{D}^0 \to K^+ K^-$ is vetoed by rejecting all events in the invariant mass range:
  $$1.80 < m_{K^+K^-} < 1.90\,\mathrm{GeV}/c^2.$$

The data files that are produced by `CharmlessFitter` are then used for the Dalitz plot analysis described in chapter 5. During the analysis, the dataset is divided into two. Events which were reconstructed as three kaon tracks with a total charge of $+1$ are termed the B^+ sample. Those where the combined charge is -1 form the B^- sample.

Chapter 5

Analysis

5.1 `Laura++`

`Laura++` [59] [60] (Likelihood Analysis Unbinned Reconstruction of Amplitudes) is a software package designed for the full analysis of Dalitz plots. It is general to any mother and daughter particles of a three body decay, though it was designed particularly for the decays of B mesons into kaons and pions (both charged and neutral). `Laura++` is used to both fit sets of data or MC events, and also to generate sets of toy MC events. The `Laura++` programme is implemented in the C++ programming language, incorporating classes from the `Root` analysis framework [56] class library. The fitting aspect is performed using TMinuit, the `Root` interface to the `Minuit` [61] [62] numerical fitting routine. It is carried out by means of a maximum likelihood fit, whereby the value of the following likelihood function is maximised (the actual fitter minimises the negative natural logarithm of this value to give the same effect) by varying the values of the free parameters, until the maximum is reached. The values of these parameters at the maximum value are then taken to be the values that best represent the data sample.

The likelihood function is given by:

$$
\begin{aligned}
\mathcal{L}_n(x,y) \;=\; & (1 - f_{q\bar{q}} - f_{B\bar{B}}) \, \frac{|\sum_{i=1}^{N} a_i g_i(x,y)|^2 \varepsilon(x,y)}{\int \int_{DP} |\sum_{i=1}^{N} a_i g_i(x,y)|^2 \varepsilon(x,y) \; dxdy} \\
& + f_{q\bar{q}} \, \frac{Q(x,y)}{\int \int_{DP} Q(x,y) \; dxdy} \\
& + f_{B\bar{B}} \, \frac{B(x,y)}{\int \int_{DP} B(x,y) \; dxdy} .
\end{aligned}
\tag{5.1}
$$

The three terms represent the signal contributions to the Dalitz plot, the continuum background, and the backgrounds arising from B related decays.

- The variables x and y refer to the position of the event in the Dalitz plane, *i.e.* $x = m_{13}^2$ and $y = m_{23}^2$, as defined in section 2.8. The DP appearing as the integration limit indicates that the integration in these variables is to be carried out over the entire Dalitz plot space.

- $\varepsilon(x,y)$ is the efficiency of reconstruction of events, which is dependent on the Dalitz plot position.

- N is the number of contributions that are being fitted for in the amplitude fit, which includes both resonant and non-resonant components.

- a_i is the complex coefficient for each contribution. This corresponds to two fitted parameters — the amplitude and the phase.

- g_i refers to the dynamics associated with each of the contributions, including the choice of lineshape, and the angular distribution, due to the spin of the decaying resonance.

The continuum background is described by:

- $Q(x,y)$ is the amount of continuum background at the Dalitz plot location of the event, calculated from a lookup histogram.

- $f_{q\bar{q}}$ is the fraction of continuum background that is expected to populate the signal box. The signal box is defined in section 5.3.

90

In a similar way the $B\bar{B}$ background is detailed by:

- $B(x, y)$ is the amount of this background, calculated from its respective histogram.

- $f_{B\bar{B}}$ is the fraction of this background in the signal box.

The `Laura++` fitter estimates the values of the complex coefficient $a_i = c_i e^{i\theta_i}$, where c_i is the magnitude for resonance i, and θ_i is the phase for the same resonance. Only relative phases can be measured, and similarly without an absolute scale for magnitude, the fitted magnitudes only have meaning relative to another magnitude. Since only relative quantities can be measured, one phase and one magnitude are arbitrary, and can be used for comparison with the other parameters. Typically the reference magnitude is set to 1, and the reference phase to 0.

The magnitude is convention dependent, and thus not normally comparable between different analyses using different conventions. In order to allow comparison of results, amplitudes are not shown in the final results, but instead fit fractions are presented. The fit fraction is defined as:

$$F_i = \frac{\int \int_{DP} |a_i g_i(x, y)|^2 dx dy}{\int \int_{DP} |\sum_j a_j g_j(x, y)|^2 dx dy}, \tag{5.2}$$

where the terms are defined as before. Due to interference between overlapping resonances, the sum of all fit fractions need not sum to 100%.

The fit fraction for each resonance can be multiplied by the inclusive branching fraction for $B^\pm \to K^\pm K^\pm K^\mp$ to give the partial branching fraction for that resonant mode. These are presented in section 7.1.

5.2 The Dalitz Plot and Projection Plots

Events which lie within the signal box, defined in section 5.3, are used to form the Dalitz plot, and as input to the `Laura++` fitting package. Figure 5.1 shows all the signal box events plotted in the Dalitz plot.
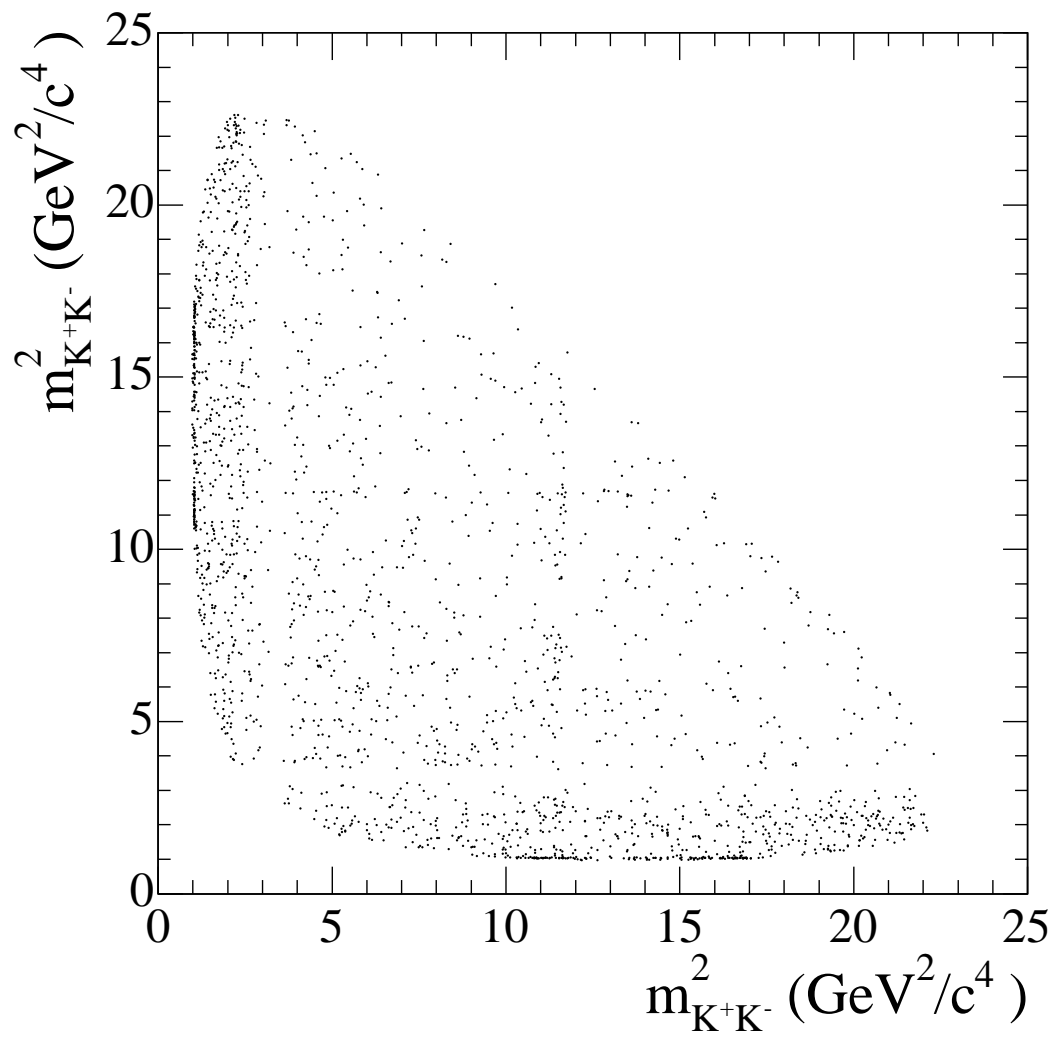
Figure 5.1: The Dalitz plot for $B^{\pm} \to K^{\pm}K^{\pm}K^{\mp}$, comprising 2067 events.
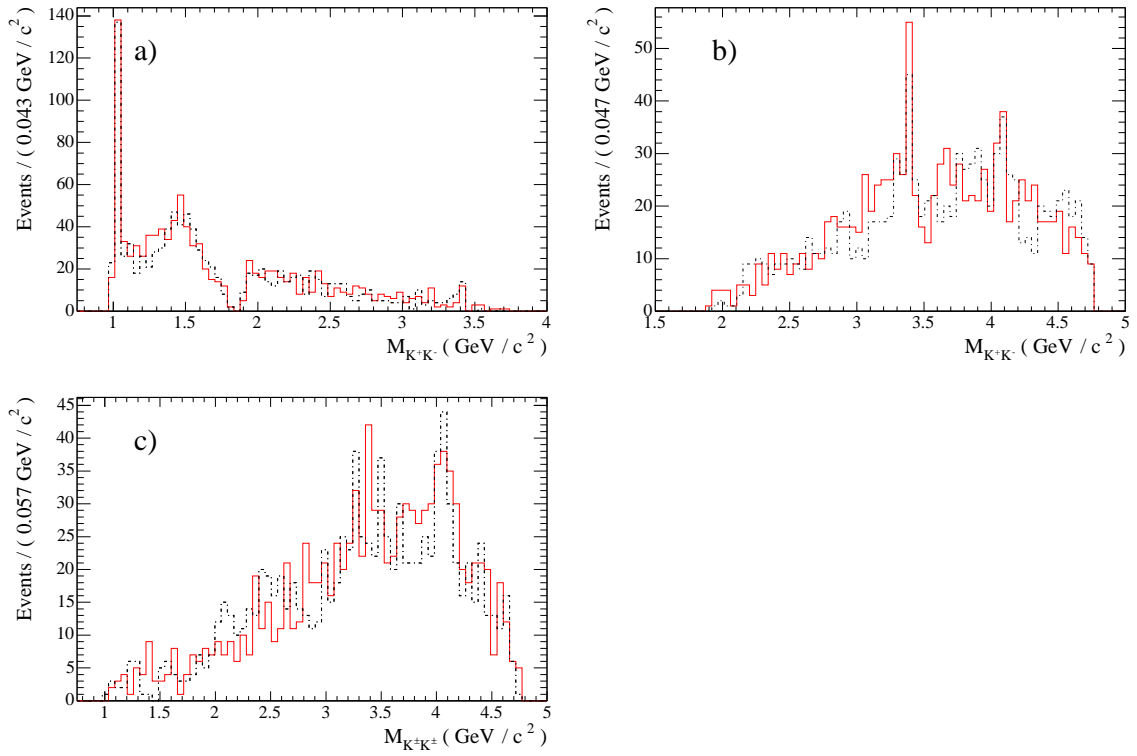
Figure 5.2: Projections of the three kaon mass pairs — a) K^+K^- lighter mass combination; b) K^+K^- higher mass combination; c) like signed kaon combination. In each plot the red line shows events from the B^+ sample, and the dashed black line shows events from the B^- sample.

Figure 5.2 shows the projections of the data in terms of the invariant masses of the three possible combinations of pairs of kaons — a) shows the lower mass combination of the unlike-signed kaons, b) shows the higher mass combination, and finally c) shows the like-signed kaon combination. For each of these plots the data are split into those events from the B^+ sample, shown as a solid red line, and those from the B^- sample, shown as a dashed black line. It can be seen that the gross structures in the two samples are consistent, and that differences arise between the samples as a result of statistical fluctuations.

5.3 Definition of Signal Box and Sideband

The stored $B^\pm \to K^\pm K^\pm K^\mp$ data have loose restrictions placed on m_{ES} and ΔE. The distribution of these events in the $\Delta E - m_{\text{ES}}$ plane is shown in figure 5.3. Further cuts on these variables are used to define a signal box, a sideband, and a signal strip.

The signal box is the region from which events are selected to be used in the final Dalitz plot fit. The sideband is used to characterise the shape of the continuum background. The signal strip comprises both the signal box and sideband, and the connecting region — it is used to estimate the fraction of continuum background that exists in the signal box, by extrapolation from the sideband.

These regions are defined by the following m_{ES} cuts:

- Signal box — $5.271 < m_{\text{ES}} < 5.287 \, \text{GeV}/c^2$.

- Sideband — $5.200 < m_{\text{ES}} < 5.260 \, \text{GeV}/c^2$.

- Signal Strip — $5.200 < m_{\text{ES}} < 5.287 \, \text{GeV}/c^2$.

The size of the signal box is approximately chosen to cover a range of $\pm 3\sigma$ in both m_{ES} and ΔE. Figure 5.3 shows the distribution of the selected data events for $B^\pm \to K^\pm K^\pm K^\mp$. In the figure the signal box is shown bounded by a blue solid line, and the sideband is shown bounded by a dashed red line. Only events lying within the signal strip are plotted.

94
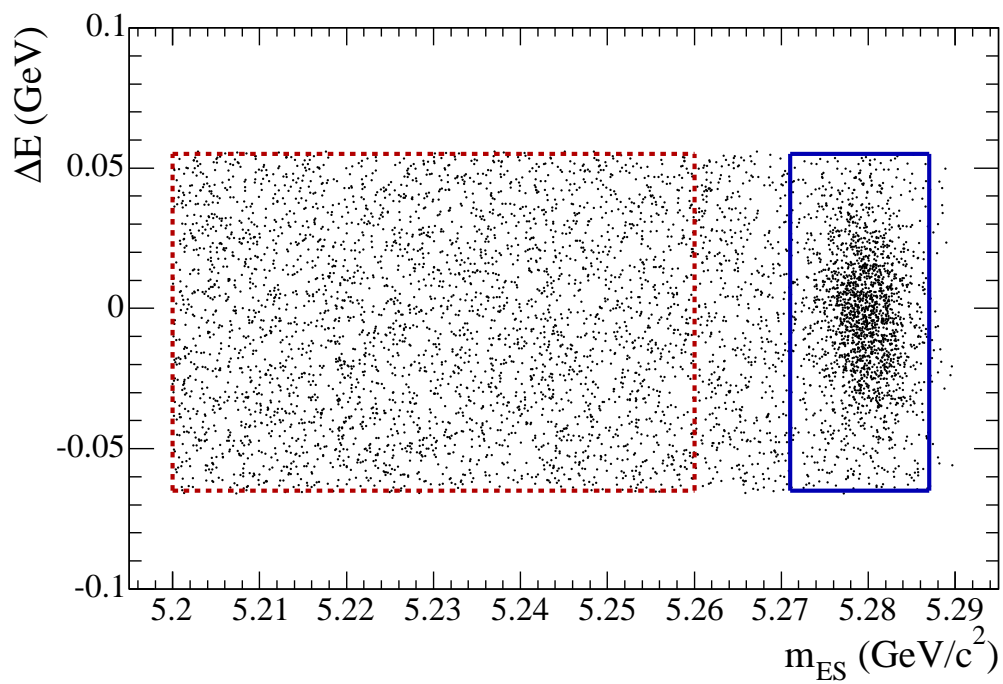
Figure 5.3: Distribution of events in the signal strip in the $\Delta E - m_{\mathrm{ES}}$ plane. Solid blue line — signal box; dashed red line — sideband.
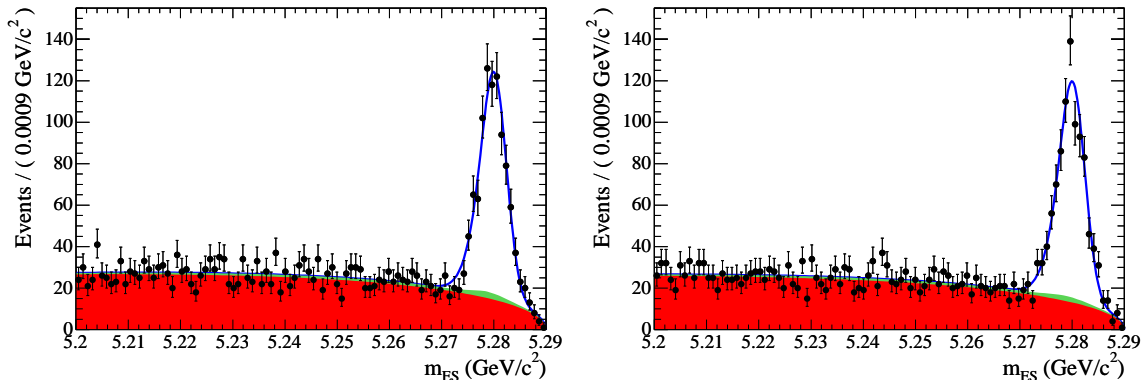
Figure 5.4: The projection in m_{ES} for signal strip events. The data are shown as solid points, the fit is shown as a blue line, and the solid red and green areas show the continuum and B-related backgrounds respectively. The two charge samples are shown separately: left hand subfigure — the B^+ sample; right hand subfigure — the B^- sample.

5.4 Fitting m_{ES} distribution to obtain Background fractions

The background fraction arising from B mesons is calculated from the number of events selected in a MC study, explained in section 5.6. This B background is included as a fixed component in the continuum background fit.

In order to calculate the fraction of continuum background, a fit is carried out to the distribution of all events in the m_{ES} projection of the signal strip. The fit is performed separately for the B^+ and B^- samples. These projections are shown in figure 5.4 with the fit results overlaid.

In the fit the signal contribution is modelled as a double Gaussian (the sum of two Gaussians, with a common mean) — signal MC is used to determine the mean and widths of this distribution. The background is modelled by an Argus function [63]:

$$f(x) = x\sqrt{1 - \left(\frac{x}{\zeta}\right)^2} \, e^{-\chi\left(\sqrt{1 - \left(\frac{x}{\zeta}\right)^2}\right)}, \tag{5.3}$$

96

where χ is a shape parameter, and ζ is the endpoint of the function, which in this fit is fixed to be the value of the beam energy ($\sqrt{s}/2$). In the fit the m_{ES} value is used as the x variable from the equation. The B-related background is modelled as the sum of an Argus function and a Gaussian function, the parameters of which are determined from the B background MC study, and these are kept fixed during the fit procedure.

During the fit the mean of the signal Gaussian, the Argus shape parameter of the continuum background, and the signal and continuum fractions are allowed to vary. The continuum fraction is then used in the Dalitz plot fit. The signal fraction is used to calculate the signal yield, which is used to calculate the overall branching fraction.

Table 5.1: Fractions of signal, continuum and B-related backgrounds calculated from fit to the m_{ES} distribution.

Event type	B^+ sample	B^- sample
Signal fraction (%)	72 ± 4	74 ± 4
$q\bar{q}$ fraction (%)	24 ± 2	23 ± 2
$B\bar{B}$ fraction (%)	3.3 ± 0.4	3.0 ± 0.3

Table 5.1 gives the fractions of signal, continuum, and B-related backgrounds that are calculated from the fit to the m_{ES} distribution, and the MC study.

5.5 Continuum Background

Continuum events are the dominant source of background in this analysis. It consists of those events arising from $e^+e^- \to q\bar{q}$ interactions where $q = u, d, s, c$. The large cross section (as stated in section 1.1) for these light quark events means they make up the vast majority of interactions occurring within the detector. Although they are sufficiently different to B decays that most can be cut out during event selection, enough remain to leave a sizeable background.

The most important difference between continuum and signal events is the shape of the event. For $B\bar{B}$ events the B mesons are created almost at rest in the centre of mass frame. The directions of the decay products cover the entire angular space and these events are called spherical events. For light quark continuum events the event topology will not be spherical, but will instead follow a $(1 + \cos^2 \theta)$ distribution, where the maxima occur along the beam line. In addition, as only a small fraction of the available energy is used in the creation of the new particles, the event will be observed as collimated jets.

In order to cut out most of these continuum events, use is made of topological variables. The B mass constraint (section 4.3.3) applied to continuum events makes them appear more signal like, and so the values of these variables from a fit without the mass constraint are used. In some of the definitions used a property is summed over all of the particles in an event, except for the B meson. This property is described as belonging to the Rest Of the Event (ROE).

The principal variables used are:

- Fisher discriminant, $\mathcal{F}$,

- $\cos \theta_T$.

Here $\cos \theta_T$ is the cosine of the thrust angle of the event. The thrust angle, θ_T, is the angle that exists between the thrust axis of the candidate B meson, and the thrust axis of ROE, which is calculated in the centre of mass frame. The thrust axis is the axis along which total longitudinal momentum is maximised.

The continuum event distribution peaks very strongly at $+1$ and -1, whereas the distribution for signal events is approximately uniform across the whole domain. The distributions of $\cos \theta_T$ for signal MC (solid blue line) and off-resonance data (dashed red line) are shown in Figure 5.5. Note this figure shows the distributions after a preliminary cut of 0.95 has been placed on the value (section 4.6). This variable is required to have an absolute value of no more than 0.9.
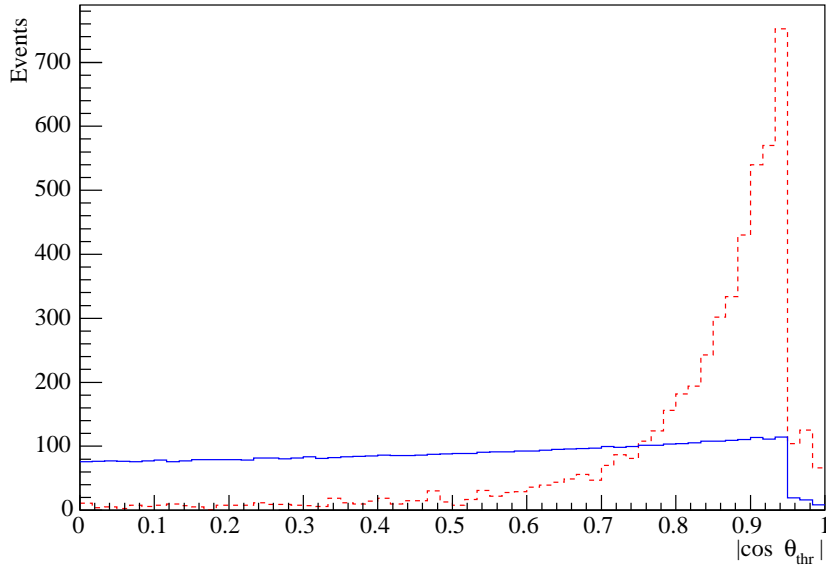
Figure 5.5: Distributions of $\cos\theta_T$ for $B^\pm \to K^\pm K^\pm K^\mp$ MC (solid blue line) and off-resonance data (dashed red line).

5.5.1 Fisher Discriminant, $\mathcal{F}$

A Fisher discriminant is a linear combination of a number of variables. It is used in cases where the individual variables have some discriminatory power, but the combined variable has a greater ability to discriminate between signal and continuum events. Rather than simply cutting on each variable, using the combination of variables can take advantage of any extra information, such as that arising from correlations between variables.

The definition of the Fisher Discriminant, $\mathcal{F}$ is:

$$\mathcal{F} = \sum_i \alpha_i x_i = \vec{\alpha}^T \vec{x}, \tag{5.4}$$

where x_i are the chosen event variables, and α_i are coefficients to be chosen.

The Fisher discriminant used in this analysis is composed of five separate variables. These are:

- Zeroth degree Legendre polynomial:

$$L_0 = \sum_i^{ROE} p_i \tag{5.5}$$

- Second degree Legendre polynomial:

$$L_2 = \sum_i^{ROE} p_i \times \frac{1}{2}(3\cos^2\theta_i - 1) \tag{5.6}$$

- $TFlv$, the flavour tagging algorithm output. This is primarily used to distinguish between B^0 and $\bar{B}^0$ mesons, and varies between 0 and 1, with higher values indicating better quality tags. Though this analysis does not use neutral B mesons, the algorithm is likely to give higher values for charged B meson events, than for continuum events.

- $\cos\theta_{Bmom}$, the angle between the z-axis and the momentum of the B candidate.

- $\cos\theta_{Bthr}$, the angle between the z-axis and the thrust axis of the B candidate.

When summing over ROE, for each track or cluster, p_i is the momentum, and θ_i is the polar angle.

In order to determine the values of the coefficients α_i samples of phase space signal Monte Carlo and off-peak data are used. The signal-background separation, D, is defined as:

$$D = \frac{(\bar{\mathcal{F}}_S - \bar{\mathcal{F}}_B)^2}{\sigma_S^2 + \sigma_B^2} \tag{5.7}$$

where $\bar{\mathcal{F}}_S$ is the mean of the Fisher variable for signal, and σ_S^2 is its variance. There are equivalent expressions for background contributions upon the substitution $S \to B$. These can be written in terms of the means, μ, of the component variables, x_i, and a covariance matrix, E_S, of the x variable distributions:

$$\bar{\mathcal{F}}_S = \vec{\alpha}^T \vec{\mu}_S, \tag{5.8}$$

$$\sigma_S^2 = \vec{\alpha}^T E_S \vec{\alpha}. \tag{5.9}$$

Then by defining $W = E_S + E_B$ and $\vec{d} = \vec{\mu}_S - \vec{\mu}_B$ the parameter D can be rewritten as:

$$D = \frac{\vec{\alpha}^T \vec{d} \vec{d}^T \vec{\alpha}}{\vec{\alpha}^T W \vec{\alpha}} \tag{5.10}$$

The optimal values of α_i can be determined by differentiating D with respect to α_i, and setting the derivative to zero. This yields:

$$\vec{\alpha} = W^{-1} \vec{d} \tag{5.11}$$

Figure 5.6 shows the distributions of the Fisher Discriminant for $B^\pm \to K^\pm K^\pm K^\mp$ MC, and for off-resonance data.
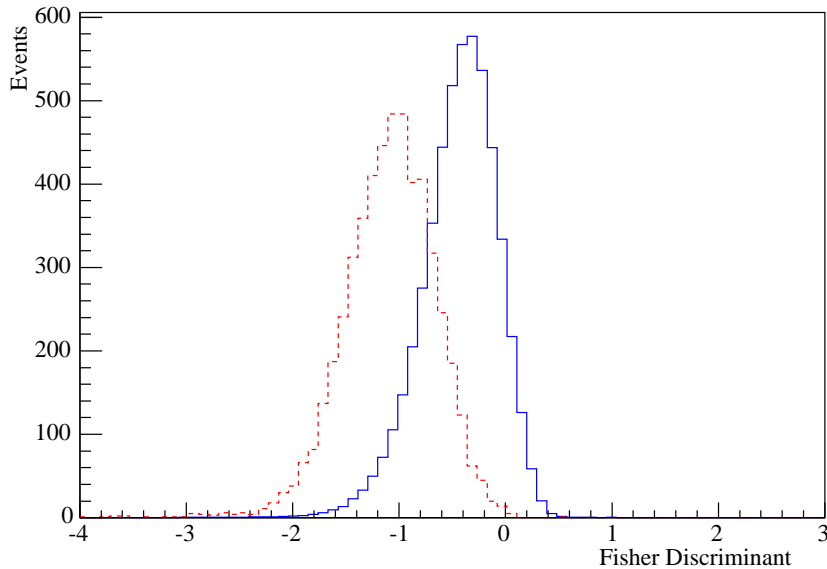
Figure 5.6: Distributions of the Fisher Discriminant, $\mathcal{F}$, for $B^\pm \to K^\pm K^\pm K^\mp$ MC (solid blue line) and off-resonance data (dashed red line).

The values of the cuts applied are optimised by maximising the value of $S/\sqrt{S + B}$, where S and B refer to the signal and background components respectively. The optimisation process follows the procedure outlined in [64]. Figure 5.7 shows the
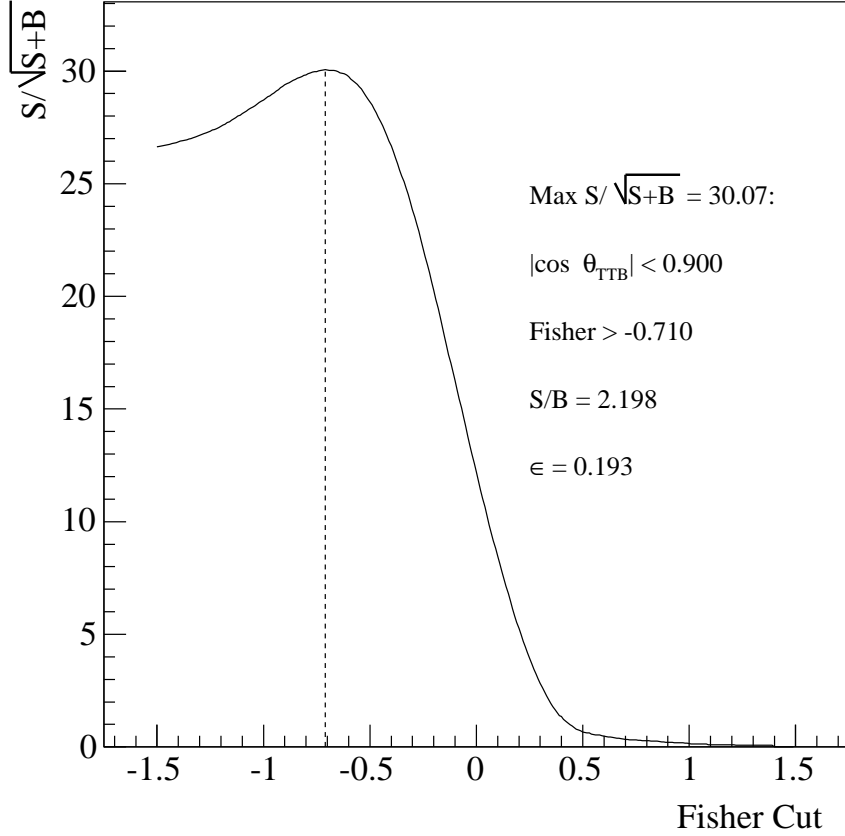
Figure 5.7: Optimisation of the Fisher Discriminant cut, by maximising $S/\sqrt{S+B}$.

variation in $S/\sqrt{S+B}$ as a function of the value of the Fisher Discriminant, that is used to decide the cut value.

5.5.2 Distribution of Continuum Background

The distribution of continuum backgrounds within the Dalitz plot space is determined using data from the sideband (defined in section 5.3), and data taken off-peak. The off-peak data should have no $e^+e^- \rightarrow \Upsilon(4S) \rightarrow B\overline{B}$ events in it. The sideband data will have these types of event, so the expected distribution of $B\overline{B}$ events in the sideband is
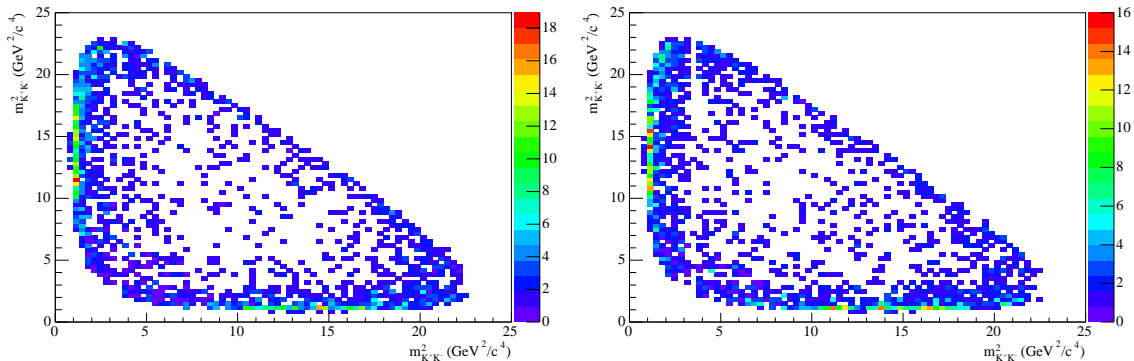
Figure 5.8: Dalitz plot distributions for continuum background events, from off-resonance and sideband data. The left hand plot shows the B^+ sample, and the right hand plot shows the B^- sample.

calculated, using the same method as detailed in section 5.6. This is then subtracted from the sideband data. The two data samples (off-resonance and $B\overline{B}$-subtracted sideband) have consistent distributions, and they are added together to give a larger statistical sample. The distributions of these events in the Dalitz plot is shown in figure 5.8 — the distributions for the B^+ and B^- samples are shown separately in the left and right hand plots respectively.

It can be noted that most of the continuum background is manifest around the edges of the Dalitz plot space and the centre of the plot is very sparsely populated. In addition it was expected that there should be a contribution from the $\phi(1020)$ resonance occurring within the continuum. However the width of this resonance is a lot less than the width of the bins used for the continuum histogram. Therefore the ϕ is not reproduced in the background shape. In order that the resonance should be correctly modelled use of a much finer binning was studied. The region including the ϕ is given a finer binning, whilst the rest of the plot uses the standard binning. This involves the ϕ region having a binning which is equivalent to a 5000×5000 binning across the entire plot.

103

Square Dalitz Plot

Even a binning as fine as this does not perfectly represent the resonance. In addition it is inefficient in the use of histograms. Instead a technique was applied using an alternative parametrisation [65] which had been tried in other *BABAR* analyses, here referred to as a square Dalitz plot (though since this parametrisation does not have a distribution that is uniform in phase space, this cannot truly be described as a Dalitz plot).

In the square Dalitz plot parametrisation the histogram is plotted in terms of two variables m' and θ'. These are defined as such:

$$
\begin{aligned}
m' &= \frac{1}{\pi}\cos^{-1}\left(2\frac{m_{++} - m_{++}[\text{min}]}{m_{++}[\text{max}] - m_{++}[\text{min}]} - 1\right)\\
\theta' &= \frac{1}{\pi}\theta_{++}.
\end{aligned}
\tag{5.12}
$$

Both of these variables can take values only between 0 and 1. m_{++} is the invariant mass value between the two Kaons of identical charge, which can take maximum and minimum values of $m_{++}[\text{max}] = m_B - m_K$ and $m_{++}[\text{min}] = 2m_K$, and θ_{++} is the helicity angle between one of the identically charged Kaons and the B momentum when measured in the rest frame of the identically charged Kaon pair. The transformation between the original and the square Dalitz plot coordinates can be defined via the Jacobian, J, as:

$$
dm_{13}^2 dm_{23}^2 = |J| dm' d\theta'.
\tag{5.13}
$$

The determinant, $|J|$, can then be written as:

$$
|J| = 4|p_1^*||p_2^*|m_{++}\frac{\partial m_{++}}{\partial m'}\frac{\partial \cos\theta_{++}}{\partial \theta'},
\tag{5.14}
$$

where p_1^* and p_2^* are the momenta of the two tracks of identical charge measured in the rest frame of the identically charged Kaon pair, and:

$$
\begin{aligned}
\frac{\partial m_{++}}{\partial m'} &= -\frac{\pi}{2}\sin(\pi m')(m_{++}[\text{max}] - m_{++}[\text{min}])\\
\frac{\partial \cos\theta_{++}}{\partial \theta'} &= -\pi\sin(\pi\theta').
\end{aligned}
\tag{5.15}
\tag{5.16}
$$

104
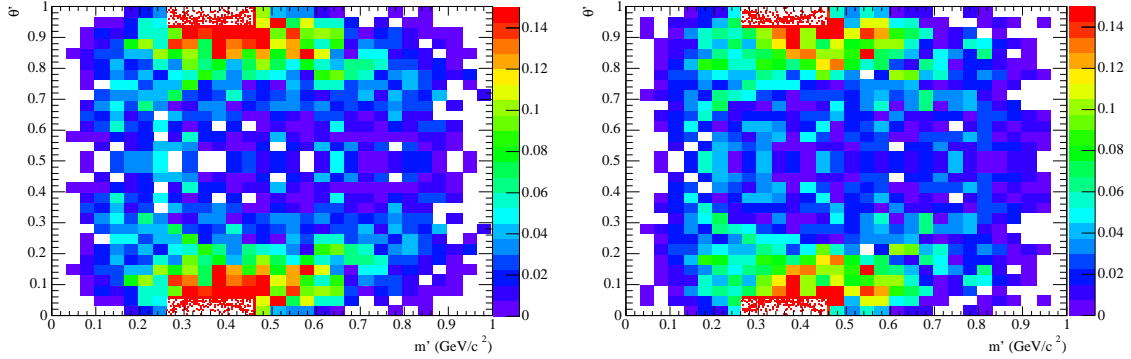
Figure 5.9: Square Dalitz plot distributions for $q\bar{q}$ background events. Left: B^+, right: B^-. The finely binned regions at the top and bottom of the plots contain the space occupied by the $\phi(1020)$ resonance.

The effect of this transformation is to expand the edges of the plot to take up a greater area, and to condense the centre of the plot to take up a lesser area. Thus the region of the plot where most of the continuum background occurs receives greater prominence in this parametrisation. It should also be noted that any resonant structure present in the plot will no longer occupy a straight line in the square Dalitz plot, but will instead form a curve. Further examples of this behaviour can be seen in the $B\bar{B}$ background histograms in section 5.6.

The $\phi(1020)$ Resonance in the Square Plot

Whilst this parametrisation does expand the edges of the Dalitz plot significantly, it still does not perfectly model the ϕ resonance in the continuum. Using a finer binning in the region that the ϕ occupies in the square plot was found to be more effective, and did not require the extreme binning regimes tested with the original Dalitz plot parametrisation. Figure 5.9 shows the distribution of continuum events in the square Dalitz plot space, where the two small curves at the top and bottom of the plot are the regions occupied by the $\phi(1020)$ resonance. This histogram modelled the $\phi(1020)$ in the continuum background well.

105

5.6 Backgrounds Arising from Decays of B mesons to Final States other than $K^\pm K^\pm K^\mp$

In addition to the continuum backgrounds arising from the production of light quarks, there is a second source of background that arises from the decays of B mesons to many final states that are different from the signal mode $B^\pm \to K^\pm K^\pm K^\mp$. These events share the spherical topology of signal events, but are likely to be shifted in m_{ES} and ΔE from true signal events.

One source of B related backgrounds is from decays of B mesons to four-body final states, where one of the four daughter particles has not been reconstructed and the event is thus mis-reconstructed as a three-body decay. In addition there are decays where one of the particles (often a pion) is misidentified as a kaon — such as the decay $B^\pm \to K^\pm K^\mp \pi^\pm$ being misidentified as $B^\pm \to K^\pm K^\pm K^\mp$.

In order to study the effects of these backgrounds, the $B^\pm \to K^\pm K^\pm K^\mp$ selection criteria are applied to generic MC events. These are MC events that have been produced to include all known decay modes of the B meson. All modes which have a non-negligible proportion of events reconstructed are considered for study. For each of these modes, a sample of exclusive MC is reconstructed to determine the expected numbers of events in the signal region and the sideband/signal strip. These MC events can also be plotted in the Dalitz plane to show the distribution of these events. Once all samples have been considered, the Dalitz distributions are summed together, such that each event is weighted to give the expected number of events in the signal box.

All the decay modes that were found to make a contribution to this background source are listed in tables 5.2 and 5.3. The first of these tables details those modes arising from charged B meson decays, and the second details those modes arising from neutral B meson decays, and includes the totals from all modes. The Dalitz distribution of the sum of all these modes can be seen in figure 5.10. The most prominent feature visible is the background due to the J/ψ, at $m^2_{K^+K^-} = 9.6\,\mathrm{GeV}^2/c^4$, where the J/ψ decays to K^+K^-.
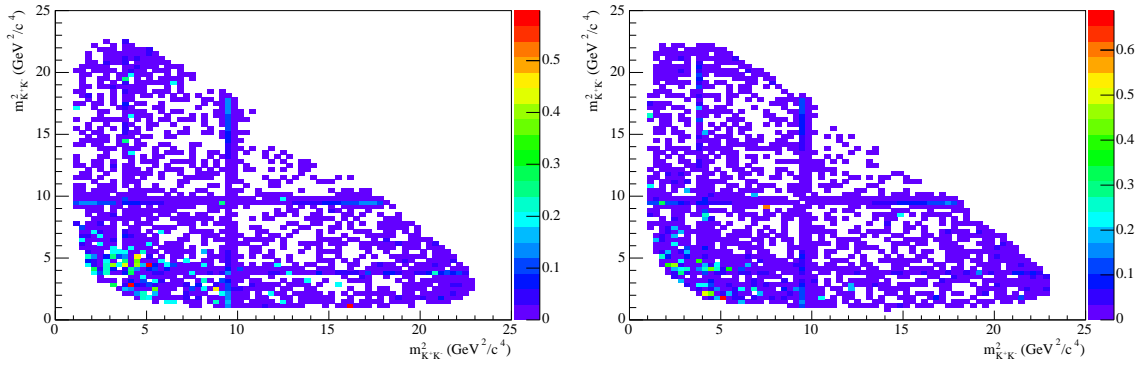
Figure 5.10: Dalitz plot distributions for $B\overline{B}$ background events. Left: B^+, right: B^-.
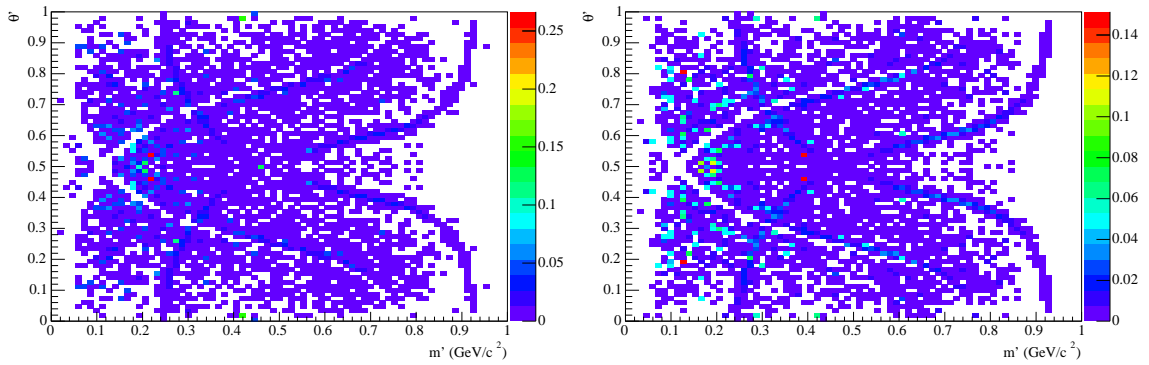
Figure 5.11: Square Dalitz plot distributions for $B\overline{B}$ background events. Left: B^+, right: B^-.

5.6.1 B backgrounds in the Square Dalitz Plot Parametrisation

As was the case with the continuum background, the background arising from B decays can also be plotted in the square Dalitz plot space. The centre of the conventional Dalitz plot is quite void of content, with the exception of the J/ψ, so this formalism is also appropriate here.

The square plots are shown in figure 5.11. The transformation of linear bands to curved bands can again be noted.

Table 5.2: B^+B^- background modes — detailing branching fractions, efficiencies and number of expected events.

Mode	BF (10^{-6})	Efficiency (%)		Number of Expected Events	
		Signal Strip	Signal Box	Signal Strip	Signal Box
$B^+ \to K^+K^-\pi^+$	< 6.3	0.4280 ± 0.0057	0.2384 ± 0.0043	6.3 ± 6.3	3.5 ± 3.5
$B^+ \to K^+\pi^-\pi^+$	4.9 ± 1.5	0.0134 ± 0.0010	0.00285 ± 0.00047	0.152 ± 0.048	0.032 ± 0.011
$B^+ \to \pi^+\pi^-\pi^+$	10.9 ± 3.7	0.00095 ± 0.00021	0.00072 ± 0.00018	0.0239 ± 0.0097	0.0182 ± 0.0077
$B^+ \to K_0^{*0}(1430)\pi^+;\ K_0^{*0}(1430) \to K^+\pi^-$	32.3 ± 3.1	0.0124 ± 0.0026	0.0051 ± 0.0017	0.93 ± 0.22	0.38 ± 0.13
$B^+ \to \overline{D}^0 K^+;\ \overline{D}^0 \to K^+K^-$	1.4 ± 0.2	0.581 ± 0.015	0.1776 ± 0.0084	1.94 ± 0.33	0.59 ± 0.10
$B^+ \to \overline{D}^0 K^+;\ \overline{D}^0 \to K^+\pi^-$	14.1 ± 2.3	0.448 ± 0.011	0.1669 ± 0.0068	14.6 ± 4.2	5.4 ± 1.6
$B^+ \to \overline{D}^0 K^+;\ \overline{D}^0 \to K^+\pi^-\pi^0$	48.1 ± 8.3	0.2063 ± 0.0090	0.0433 ± 0.0041	23.0 ± 4.1	4.82 ± 0.96
$B^+ \to \overline{D}^0 \pi^+;\ \overline{D}^0 \to K^+K^-$	20.5 ± 1.4	0.0150 ± 0.0087	0.0 ± 0.0	0.67 ± 0.39	0.0 ± 0.0
$B^+ \to \overline{D}^0 \pi^+;\ \overline{D}^0 \to K^+\pi^-$	189.2 ± 11.9	0.0139 ± 0.0025	0.0028 ± 0.0011	6.1 ± 1.2	1.22 ± 0.50
$B^+ \to \overline{D}^0 \pi^+;\ \overline{D}^0 \to K^+\pi^-\pi^0$	647.4 ± 54.8	0.0068 ± 0.0017	0.00161 ± 0.00080	10.2 ± 2.6	2.4 ± 1.2
$B^+ \to \overline{D}^{*0} K^+;\ \overline{D}^{*0} \to \overline{D}^0\pi^0;\ \overline{D}^0 \to K^+K^-$	0.87 ± 0.25	0.657 ± 0.047	0.103 ± 0.019	1.32 ± 0.39	0.208 ± 0.070
$B^+ \to \overline{D}^{*0} K^+;\ \overline{D}^{*0} \to \overline{D}^0\pi^0;\ \overline{D}^0 \to K^+\pi^-$	8.5 ± 3.1	0.435 ± 0.012	0.1361 ± 0.0069	8.5 ± 3.2	2.67 ± 0.99
$B^+ \to \overline{D}^{*0} K^+;\ \overline{D}^{*0} \to \overline{D}^0\pi^0;\ \overline{D}^0 \to K^+\pi^-\pi^0$	29.0 ± 8.4	0.1142 ± 0.0097	0.0142 ± 0.0034	7.7 ± 2.3	0.95 ± 0.36
$B^+ \to \overline{D}^{*0} K^+;\ \overline{D}^{*0} \to \overline{D}^0\gamma;\ \overline{D}^0 \to K^+K^-$	0.53 ± 0.16	0.626 ± 0.016	0.1328 ± 0.0071	0.81 ± 0.24	0.164 ± 0.049
$B^+ \to \overline{D}^{*0} K^+;\ \overline{D}^{*0} \to \overline{D}^0\gamma;\ \overline{D}^0 \to K^+\pi^-$	5.2 ± 1.9	0.462 ± 0.013	0.1430 ± 0.0074	5.6 ± 2.1	1.73 ± 0.65
$B^+ \to \overline{D}^{*0} K^+;\ \overline{D}^{*0} \to \overline{D}^0\gamma;\ \overline{D}^0 \to K^+\pi^-\pi^0$	17.8 ± 5.3	0.076 ± 0.014	0.0048 ± 0.0018	3.1 ± 1.1	0.39 ± 0.23
$B^+ \to \overline{D}^{*0} \pi^+;\ \overline{D}^{*0} \to \overline{D}^0\pi^0;\ \overline{D}^0 \to K^+K^-$	11.1 ± 1.2	0.0306 ± 0.0046	0.0034 ± 0.0012	0.79 ± 0.14	0.122 ± 0.048
$B^+ \to \overline{D}^{*0} \pi^+;\ \overline{D}^{*0} \to \overline{D}^0\pi^0;\ \overline{D}^0 \to K^+\pi^-$	108.2 ± 11.0	0.0159 ± 0.0026	0.00200 ± 0.00076	4.00 ± 0.77	0.86 ± 0.32
$B^+ \to \overline{D}^{*0} \pi^+;\ \overline{D}^{*0} \to \overline{D}^0\pi^0;\ \overline{D}^0 \to K^+\pi^-\pi^0$	370.2 ± 43.1	0.0051 ± 0.0012	0.0034 ± 0.0015	4.4 ± 1.2	1.72 ± 0.68
$B^+ \to \overline{D}^{*0} \pi^+;\ \overline{D}^{*0} \to \overline{D}^0\gamma;\ \overline{D}^0 \to K^+K^-$	6.82 ± 0.82	0.0224 ± 0.0039	0.0062 ± 0.0018	0.355 ± 0.075	0.054 ± 0.025
$B^+ \to \overline{D}^{*0} \pi^+;\ \overline{D}^{*0} \to \overline{D}^0\gamma;\ \overline{D}^0 \to K^+\pi^-$	66.6 ± 7.9	0.0182 ± 0.0031	0.00167 ± 0.00084	2.81 ± 0.58	0.96 ± 0.30
$B^+ \to \overline{D}^{*0} \pi^+;\ \overline{D}^{*0} \to \overline{D}^0\gamma;\ \overline{D}^0 \to K^+\pi^-\pi^0$	227.8 ± 29.8	0.0050 ± 0.0014	0.0017 ± 0.0017	2.65 ± 0.84	0.88 ± 0.46
$B^+ \to J/\psi\, K^+;\ J/\psi \to K^+K^-$	0.24 ± 0.03	19.987 ± 0.074	19.797 ± 0.074	11.0 ± 1.5	10.9 ± 1.5
$B^+ \to K_s^0 K^+;\ K_s^0 \to \pi^+\pi^-$	0.41 ± 0.41	0.0154 ± 0.0029	0.0044 ± 0.0016	0.015 ± 0.015	0.0042 ± 0.0042

Table 5.3: $B^0\overline{B}^0$ background modes, detailing branching fractions, efficiencies and number of expected events. The totals from both B^+B^- and $B^0\overline{B}^0$ are also reported.

Mode	BF	Efficiency (%)		Number of Expected Events	
	(10^{-6})	Signal Strip	Signal Box	Signal Strip	Signal Box
$B^0 \to D^-K^+$	200 ± 60	0.0915 ± 0.0061	0.0199 ± 0.0028	42 ± 13	9.2 ± 3.0
$B^0 \to D^{*-}K^+$	200 ± 50	0.0992 ± 0.0063	0.0247 ± 0.0032	46 ± 12	11.4 ± 3.2
$B^0 \to D^{*-}\pi^+$; $D^{*-} \to \overline{D}^0\pi^-$; $\overline{D}^0 \to X$	1868 ± 142	0.00154 ± 0.00019	0.000379 ± 0.000095	6.66 ± 0.97	1.63 ± 0.43
$B^0 \to D^{*-}\rho^+$; $D^{*-} \to \overline{D}^0\pi^-$; $\overline{D}^0 \to X$	4942 ± 102	0.00019 ± 0.00013	0.0 ± 0.0	2.0 ± 1.5	0.0 ± 0.0
$B^0 \to K^+K^-K^0_s$	12.4 ± 1.2	0.2136 ± 0.0098	0.0541 ± 0.0050	6.2 ± 1.3	1.57 ± 0.37
$B^0 \to K^+K^-\pi^0$	19.0 ± 9.5	0.194 ± 0.012	0.0333 ± 0.0051	8.5 ± 4.3	1.47 ± 0.77
$B^0 \to K^+\pi^-\pi^0$	36.6 ± 5.2	0.00707 ± 0.00055	0.00035 ± 0.00012	0.599 ± 0.098	0.029 ± 0.011
$B^0 \to K^+\pi^-$	18.2 ± 0.8	0.00043 ± 0.00015	0.000053 ± 0.000053	0.0180 ± 0.0064	0.0023 ± 0.0023
Total B^+B^- backgrounds				116 ± 10	40.0 ± 3.1
Total $B^0\overline{B}^0$ backgrounds				112 ± 18	25.4 ± 4.5
Total B backgrounds				229 ± 21	65.4 ± 6.5

5.7 $_s\mathcal{P}lots$

The technique known as $_s\mathcal{P}lots$ [66] is a useful tool for examining signal and background distributions separately. It can be used to plot the distribution of a species (e.g. signal or background) in a specified discriminating variable. It is an important feature of the $_s\mathcal{P}lot$ technique that the variable plotted cannot be one of those used in the fit. When this would be the case the fit has to be repeated with said variable excluded before $_s\mathcal{P}lots$ can be produced.

In this analysis the $_s\mathcal{P}lots$ are made during the m_{ES} fit, and used to plot the distributions in terms of the Dalitz plot invariant mass combinations, which are not used as discriminating variables at this stage of the analysis.

The $_s\mathcal{P}lot$ method gives each event used a weight, called an $_s\mathcal{W}eight$. A different $_s\mathcal{W}eight$ is given to each species, such that the sum of all the $_s\mathcal{W}eights$ across all the species gives the total number of events used. The $_s\mathcal{W}eights$ are calculated from the signal and background probability density functions used in the fit and their correlation matrix. This is discussed in detail in [66].

Figures 5.12 and 5.13 show the $_s\mathcal{P}lots$ for the B^+ and B^- samples, respectively. Sub-figures a), b), and c) show the $_s\mathcal{P}lots$ of the three invariant mass combinations, whereas sub-figure d) shows the $_s\mathcal{P}lot$ for the Dalitz plot, as a binned 2D histogram.

For the invariant mass projections, a comparison is provided with the background subtracted distributions. In these projections, the final signal box data sample is taken and has the background contribution (taken from the background distribution histograms normalised to the calculated number of background events in the signal box) subtracted from it bin by bin to form the histograms shown.

The $_s\mathcal{P}lots$ are used as an indicator of how well the modelling of the background (i.e. the background histogram distributions, and calculated fractions) is representing the actual backgrounds. The $_s\mathcal{P}lots$ and the background subtracted projections are
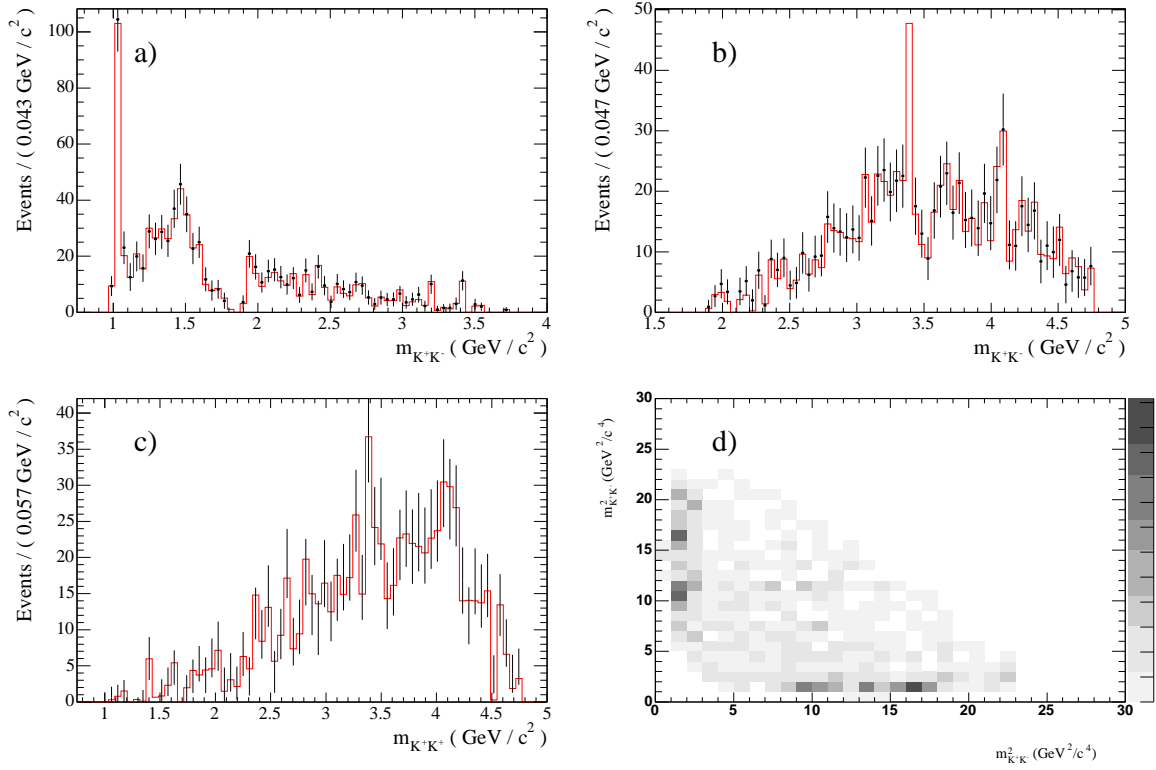
Figure 5.12: Background subtracted (red histogram) and $_s\mathcal{P}lot$ (black points) comparison for B^+ data. Sub-figure a) shows the K^+K^- mass spectrum for the lower mass combination, b) shows the K^+K^- higher mass combination, and c) shows the K^+K^+ spectrum. The $_s\mathcal{P}lot$ Dalitz plot distribution is shown in d).

in very good agreement, which is a useful validation of the background model.
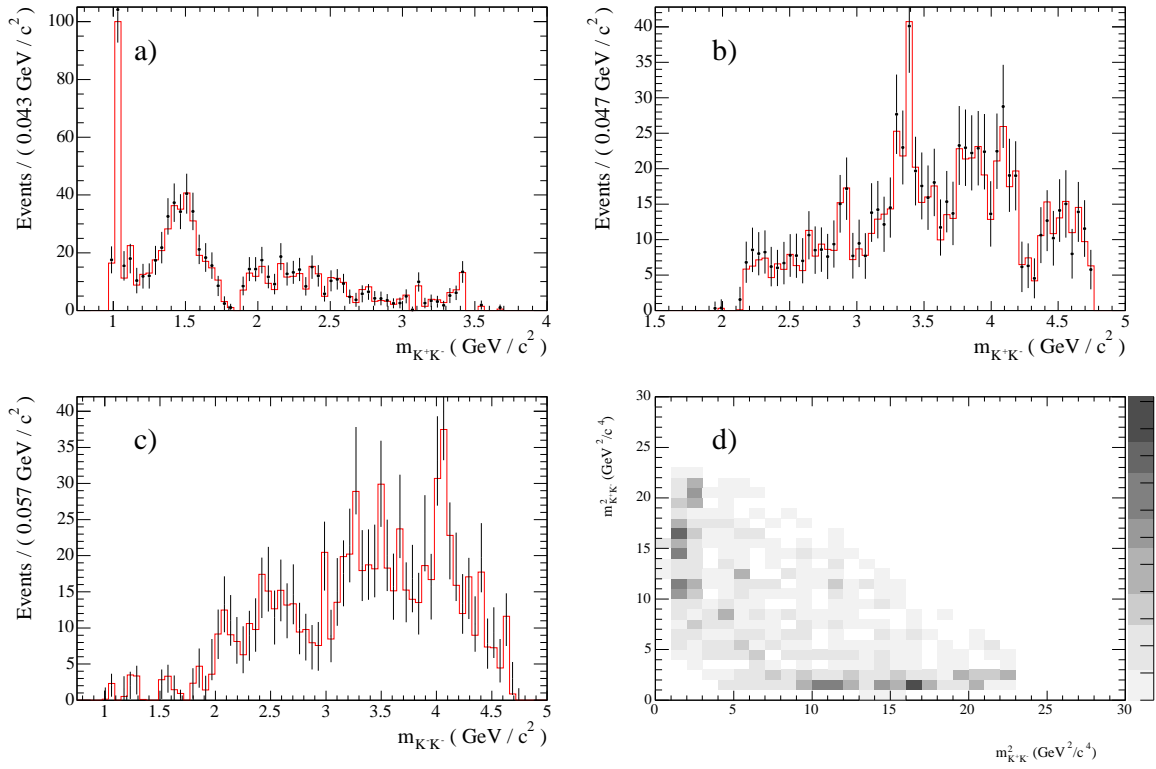
Figure 5.13: Background subtracted (red histogram) and $_s\mathcal{P}lot$ (black points) comparison for B^- data. Sub-figure a) shows the K^+K^- mass spectrum for the lower mass combination, b) shows the K^+K^- higher mass combination, and c) shows the K^-K^- spectrum. The $_s\mathcal{P}lot$ Dalitz plot distribution is shown in d).

5.8 Dalitz Plot Efficiency

It is important when fitting the data to take into account the efficiency of reconstruction of the individual events. Of all the actual events that take place within the *BABAR* detector not all will be reconstructed, and appear in the final data sample. The reconstruction efficiency, ε, can be described as:

$$\varepsilon = \frac{N_r}{N_t},\tag{5.17}$$

where N_t is the total number of events that are used in the calculation of the efficiency; and N_r is the total number that make up the final sample of events. This value is typically calculated using MC.

Further, it is not expected that the efficiency should be uniform across the whole of phase space allowed by the Dalitz plot, and therefore it is a function of the Dalitz plot coordinates — i.e. $\varepsilon = \varepsilon(x, y)$.

Variation of reconstruction efficiency across the plot is studied using a large sample of Monte Carlo events. A sample of MC was generated to simulate $B^{\pm} \to K^{\pm}K^{\pm}K^{\mp}$ events. They are uniformly generated in phase space and they will therefore uniformly populate the Dalitz plot space, due to the kinematics of a Dalitz plot (section 2.8). The sample consists of a total of 1.314×10^6 MC events.

This sample is then subjected to the same selection criteria as the data. However the veto (section 4.7) in the D region ($1.8\,\mathrm{GeV}/c^2$ to $1.9\,\mathrm{GeV}/c^2$) is not applied to the MC, to ensure that the efficiency variation near the veto region is not artificially modelled incorrectly.

In addition Monte Carlo events have truth information stored with them. The truth information contains the properties of the event from the MC generator, before any detector effects are modelled. This allows for the distinction between simulated events that have been correctly reconstructed, and those that have not (explained in more detail in section 5.9). Only events that have been correctly reconstructed are selected. The number of events passing these reconstruction criteria is 260,191.

In order to present the efficiency as a function of Dalitz plot position, the events

are used to populate two dimensional histograms. The whole MC sample is used to produce a denominator histogram, and the reconstructed events are placed into a numerator histogram. The histograms have a binning of 75×75 bins. Choice of binning is discussed more in section 5.10.

The quotient of these two histograms is taken on a bin by bin basis. The resulting histogram shows the variation in the efficiency across the whole Dalitz plot. This is shown in Figure 5.14, in the left hand sub-figure.

One additional factor has to be taken into account — some bins cross the kinematic boundary of the Dalitz plot. When this is the case it can occur that only a very small fraction of the bin includes the allowed phase space, and the bin may be very underpopulated, as compared to bins in the centre of the plot. Thus the effect of statistical fluctuations on these bins is greatly magnified. This could lead to bins with very small or very big (sometimes unphysical) efficiency values, where such variations are spurious.

In order to ameliorate this effect the histograms used to make the efficiency plot were scanned for the contents of each bin. In the case where a bin was underpopulated, then the bin was merged with a neighbouring bin. The efficiency of the "double bin" k formed from bins i and j is given by:

$$\varepsilon_k = \frac{N_i + N_j}{D_i + D_j} \tag{5.18}$$

where N is the number of events in the bin i or j of the numerator histogram, and D is the number of events in its counterpart in the denominator histogram.

Additionally the bin error on each of the bins that were combined is set to the error on the combined bin. This is relevant for the study of systematic errors.

The effect of this slight rebinning can be seen in figure 5.14, where the left hand plot shows the efficiency histogram with no low statistics correction, and the right hand plot shows the same histogram with the correction routine applied.

Figure 5.15 shows how the efficiency varies for the B^+ and B^- samples. The efficiency for the B^+ sample is shown in the left hand plot, and the efficiency of the
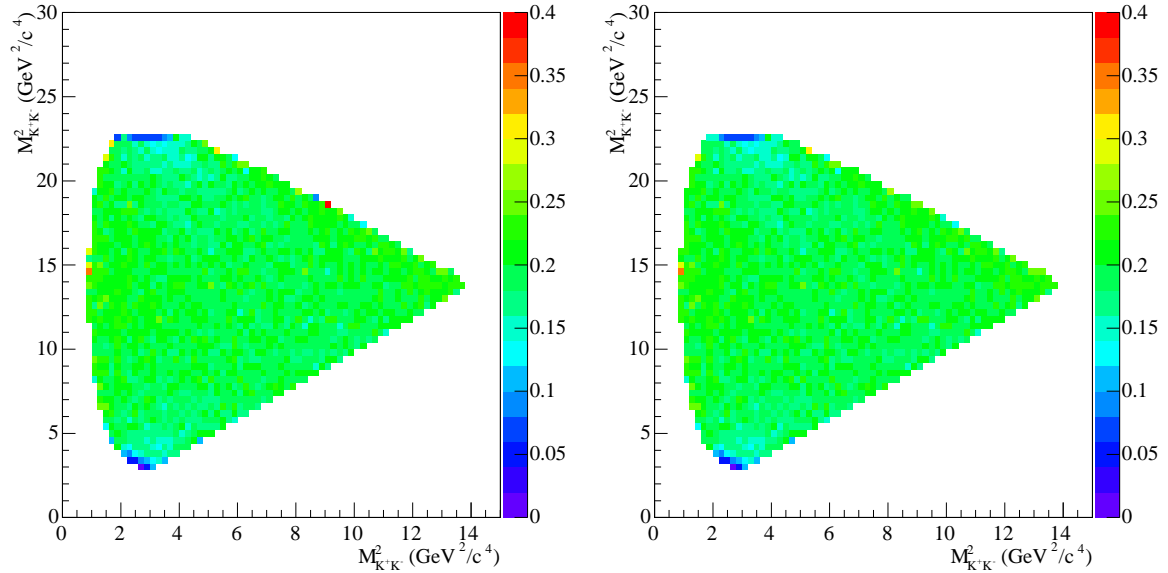
Figure 5.14: Efficiency variation across the Dalitz plot. The right hand plot has been corrected for low statistics bins.

B^- sample is shown in the right hand plot. There are no significant differences between the two charges, and so the combined charge histogram is used in the amplitude fit.

5.9 Self Cross Feed — `TrueB` or `!TrueB`?

Self Cross Feed (SCF) is the term applied to MC events that pass all the reconstruction selection criteria, but are incorrectly reconstructed. This can happen when two kaons arising from the decay of one B meson are combined with one kaon which is a daughter from the decay of the other B meson, to make a three kaon candidate, which is assumed to arise from a single B meson. If this is the case it is recorded in the MC file.

It is expected that the amount of SCF is small. This is investigated using a MC study. The same MC event sample is used as was used in the efficiency study, and this is subjected to exactly the same selection criteria, except that events which are incorrectly reconstructed are selected. (The variable in the stored file used to identify
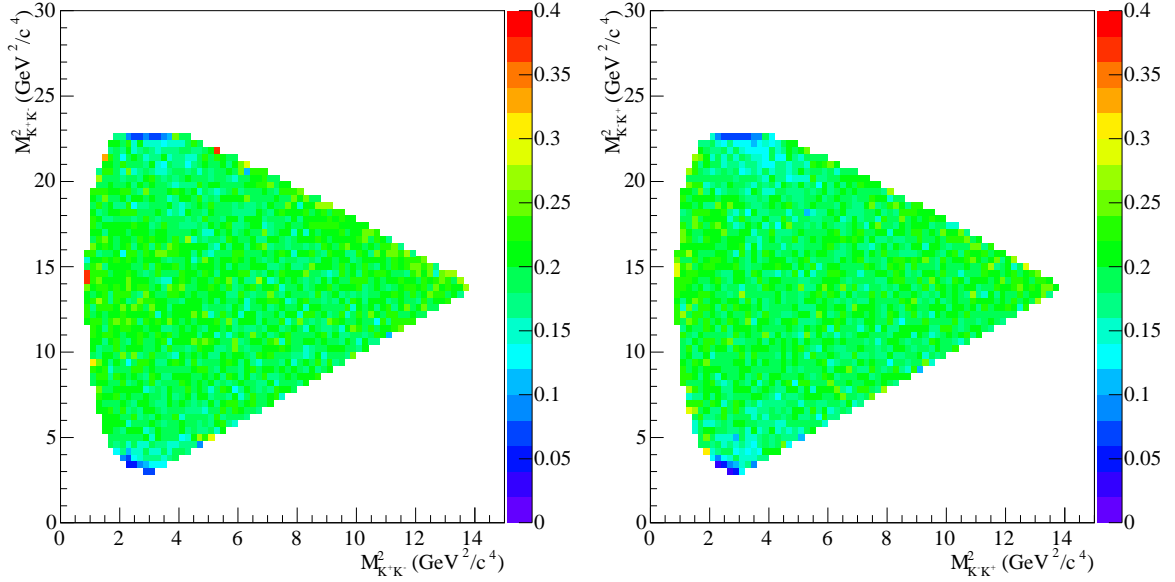
Figure 5.15: Efficiency variation across the Dalitz plot; the left hand plot shows the efficiency for the B^+ sample; the right hand plot shows the efficiency for the B^- sample.

which MC events are correctly reconstructed is named `TrueB`).

Of the 1.314×10^6 MC events, there were a total of $260,191$ that passed the selection criteria — out of these $1,619$ were found to be SCF. This is 0.6% of the total number of events passing, and so represents a very small fraction. SCF is therefore not included as a separate component in the Likelihood fit.

It can be noted that if the selection criteria are widened to the whole signal strip, as opposed to the signal box (these are defined in section 5.3), then the number of SCF events rises to 6,255, out of a total of 265,887 events that pass these criteria — this SCF sample is thus 2.3% of the signal strip events. A lot of self cross feed is therefore removed by the m_{ES} cut that defines the signal box.

In figure 5.16 the SCF efficiency is compared with the efficiency for truth matched events. These two plots have the same scale and same normalisation — the normalisation being the denominator histogram described in section 5.8. Thus a comparison

between corresponding bins in each histogram, also compares the raw number of events of SCF and truth-matched (non-SCF) events. It can be seen that the SCF is a very small fraction of the truth-matched events, even in the corners where the SCF is at its most prominent.

The distribution of SCF in the B^+ and B^- MC samples can be seen in figure 5.17. SCF is most prominent in the corners of the Dalitz plot, where there is one very low momentum Kaon, which could be less well reconstructed. It is possible that low momentum Kaons arising from the rest of the event could be included in the event reconstruction.
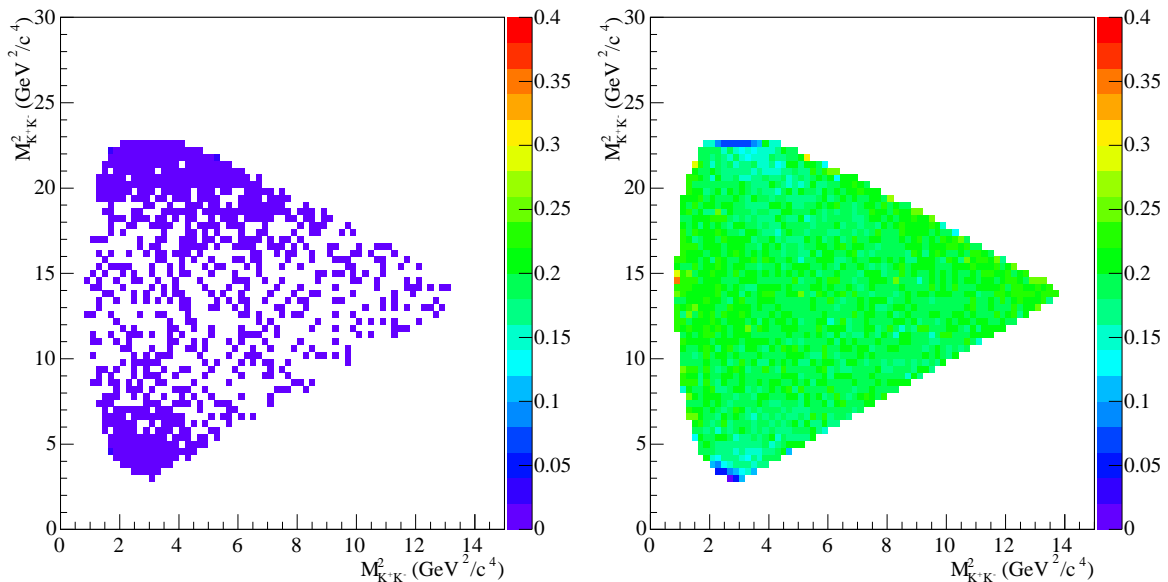
Figure 5.16: Dalitz distribution of SCF events (left), compared with truth-matched events (right). The colour scale shows the efficiency of an event being reconstructed. The scale has been set to be the same in the two diagrams, to allow comparison - the normalisation for both histograms is the total number of MC events used.
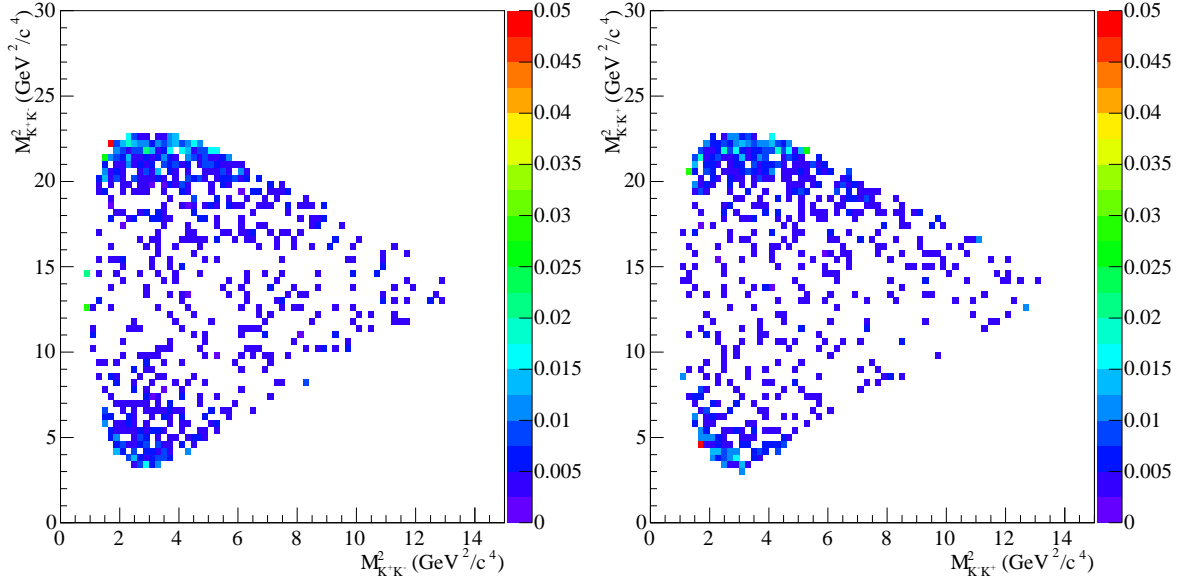
Figure 5.17: Dalitz plot distribution of SCF events; the left hand plot shows B^+ events, the right hand plot shows B^- events. The colour scale shows the efficiency for events to be reconstructed as SCF. The scale has been set to a lower level than that used in figure 5.16 to enhance the structure shown in the SCF distribution.

5.10 Migration

Migration of events is the movement of the position of events within the Dalitz plot space during the reconstruction process. This effect is studied using a MC event sample, where both the reconstructed Dalitz plot coordinates, and the true coordinates, where the simulated event was generated, are available. The distance moved is defined as:

$$d_{migration} = \sqrt{\left(m_{13}^{2(truth)} - m_{13}^{2(reco)}\right)^2 + \left(m_{23}^{2(truth)} - m_{23}^{2(reco)}\right)^2} \qquad (5.19)$$

The effect of Dalitz plot migration is two-fold. Firstly in terms of the underlying physics — if events move a long way during reconstruction then they will move in and out of the resonance bands, and more particularly the interference regions. This will diminish the ability of the fit to distinguish resonances, and fit the phases of the resonances.

Secondly when histograms are used in the fit to represent efficiency and backgrounds, each bin should reflect the properties of events that lie within it. If the migration is large, or the bin size is too small, then this may not be the case. The bin size should ideally be chosen so that it is larger than the migration effect, so that there is no significant bin to bin migration.
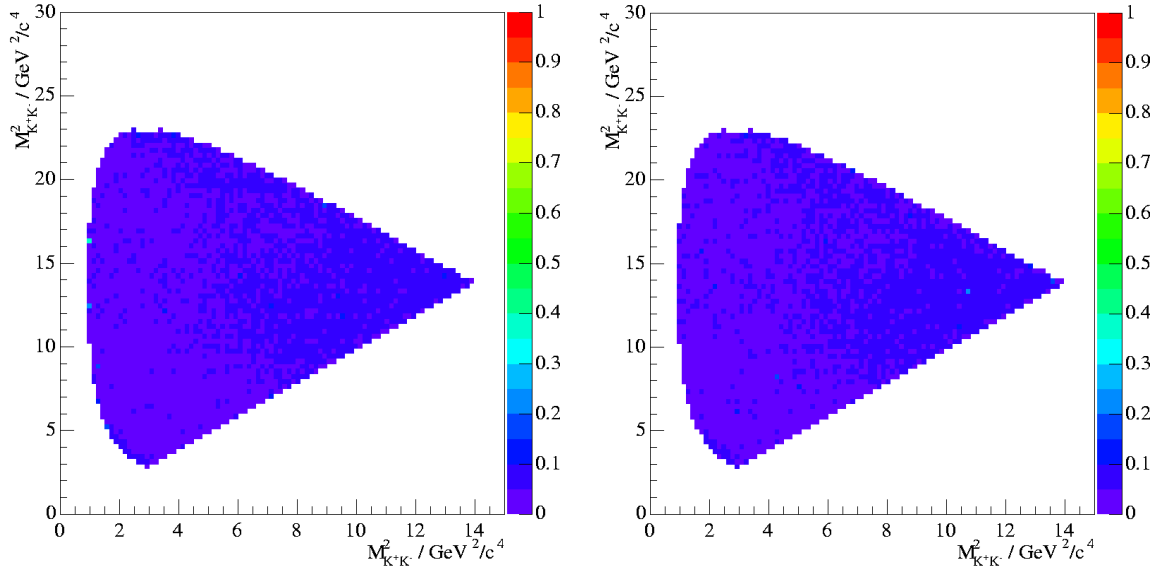
Figure 5.18: Migration of events within the Dalitz plot; the left hand plot shows inflow, the right hand plot shows outflow. The colour scale gives $\overline{d}_{migration}$ in units of GeV^2/c^4.

To study the migration effect the sample of 1.314×10^6 phase space $B^{\pm} \to K^{\pm}K^{\pm}K^{\mp}$ MC events is used. For each event the quantity $d_{migration}$ is calculated. There are two types of histogram plotted with this information:

- *Inflow*: In these histograms the migration distance is plotted at the coordinates where the event was reconstructed.

- *Outflow*: In these histograms the migration distance is plotted at the coordinates where the event was generated.

In both cases the total migration distance in each bin is divided by the number of events in that bin in order to give the actual quantity plotted in the bin as the mean

120
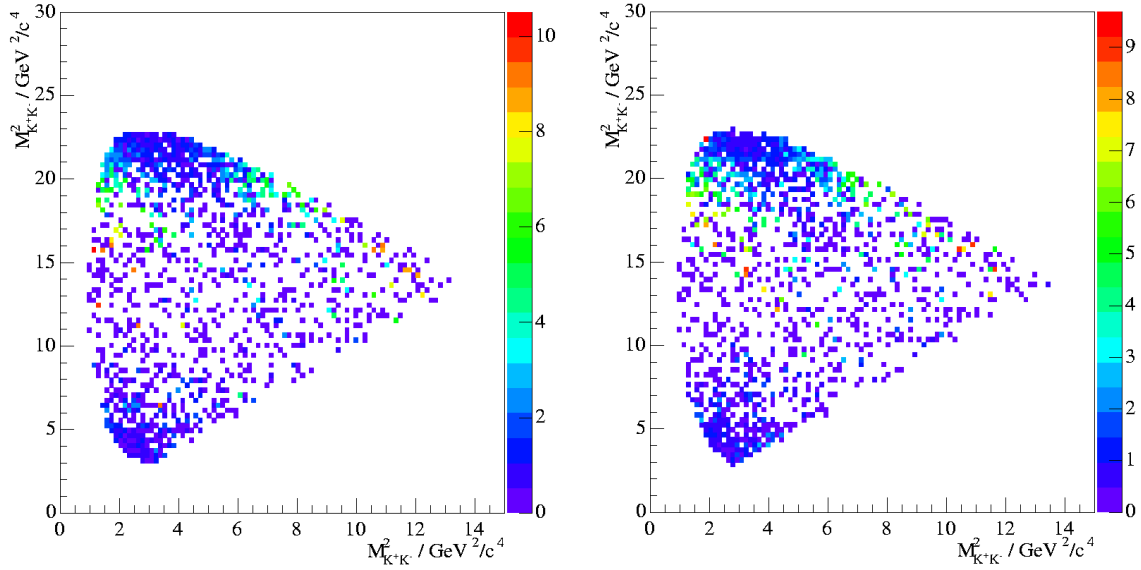
Figure 5.19: Migration of self cross feed events within the Dalitz plot; the left hand plot shows inflow, the right hand plot shows outflow. The colour scale gives $\overline{d}_{migration}$ in units of GeV^2/c^4.

migration distance per event. Figure 5.18 shows the migration for MC events, for both the positive and negative samples.

The level of migration is seen to be at a low level, and a lot smaller than the choice of 75×75 for the binning of most of the histograms chosen.

It is also possible to look at the migration of SCF events. This is shown in figure 5.19. The migration of self cross feed is higher than for truth matched MC events, and can be quite high for individual events, as would be expected for events which have been mis-reconstructed.

5.11 Multiple Solutions

It was noted early on in the development of the Dalitz plot fitting tools used in this analysis that the fitter did not necessarily converge on a unique solution for a given set of events (data or MC). This is due to local minima occurring in the multidimen-

121

sional likelihood-parameter space. These can have likelihood values only slightly worse than the global best likelihood. In order to ameliorate this complication a number of approaches were adopted which are used as standard in all the fits presented in this analysis.

Firstly the parameter values were allowed to vary over a greater range than was initially used. Specifically the magnitudes were allowed to be negative in the fit. This was due to a problem whereby the fitter could be close to a minimum of likelihood, but one of the magnitudes was very close to zero for a given iteration. The fitter would then attempt to vary this parameter, but would be unable to change it in the direction that would give a better likelihood due to the magnitude constraint. The fit, if it converged, would return a value for this magnitude that was approximately zero — the value would be of the order of the tolerance set for the fit.

Allowing negative magnitudes enables the fitter to converge on the actual minimum it is seeking. Since the magnitude is one part of a complex number, a negative magnitude solution is equivalent to a positive magnitude solution with a change in the phase by π. The constraint on the magnitude being positive was therefore made only after the fitter had returned its results, together with a change in phase if required.

A similar problem was encountered in fitting the phases. Since the fitter does not know that the phases are periodic, that is a phase of zero will give identical solutions to a phase of 2π, the fitter could get stuck at the phase boundary at 2π, and would not automatically change to a value close to zero in order to improve the likelihood. Constraining the phases to lie between zero and 2π (or $-\pi$ and π), could lead to incorrect solutions, and therefore the phase was not bounded in this way. Once the fit results were returned, the value of the phase was modified by multiples of 2π to ensure that the reported results would span the range $-\pi$ to π.

A second consideration was to perform the same fit many times, but each time to change the values to which the parameters were initially set. A random initial value was generated for each of the magnitudes and phases to be fitted. It was then found that a number of fit results may lie at a particular likelihood value, whilst others will

lie at a different likelihood value. The fit results that had the best likelihood value were selected. Investigation with toy MC (section 4.1.1) showed this approach to be valid in selecting the best solutions for a given generated sample.

Fits to the $B^{\pm} \to K^{\pm}K^{\pm}K^{\mp}$ Dalitz plot showed that there could be solutions only slightly worse in likelihood than the best solution. Fit results showing this phenomenon are shown in section 6.2.

5.12   Fitting for Additional Parameters

In addition to the magnitudes and phases, which are included as free parameters in the amplitude fit, there are other parameters which could in principle be determined in the fit, such as masses and widths of resonances. Where the normalisation of the integrals used in the fitting procedure (shown in equation 5.1) is dependent on these parameters, then to allow them to float in the fit would either require using integrals which are not correct, or recalculating the integrals at every iteration of the fit, which would be too intensive on computing time.

Instead an alternative procedure was adopted, in which the fit was carried out multiple times, each with a fixed value for the parameter, to span a range of values. This procedure was first implemented for fits using the Belle inspired non-resonant shape, given in equation (2.76), which has a single free parameter, α. Based on the value of $\alpha = 0.121 \pm 0.014$ (Solution 1) quoted by the Belle collaboration [27], this parameter was fixed to values at regular intervals between 0.1 and 0.2. A minimum in $-\ln\mathcal{L}$ occurred when fitting with α set to approximately 0.13 to 0.14. Further fits were carried out in a narrower range, from $\alpha = 0.12$ to 0.15, using a step size of 0.001. The range of values of $-\ln\mathcal{L}$ achieved is shown in figure 5.20, together with a curve showing a quadratic fit to the points.

The minimum is at $\alpha = 0.135$, and this is taken as the best value for α. To estimate the uncertainty, the values of α at which $-\ln\mathcal{L}$ is 0.5 above its minimum value are taken as the $\pm 1\sigma$ boundaries. This gives a final estimate of:
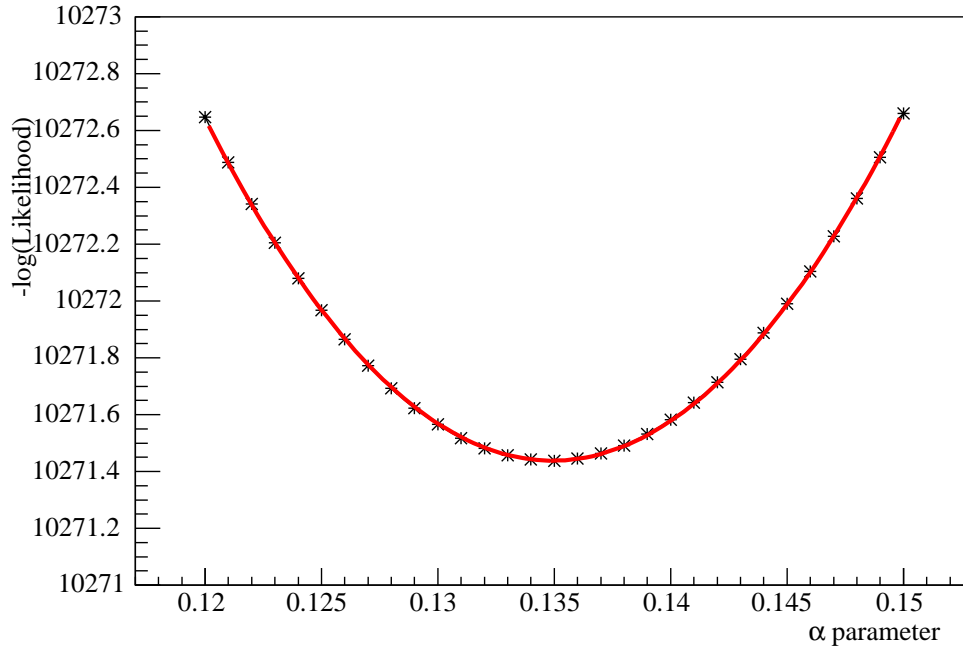
Figure 5.20: The variation of the fit likelihood as the parameter α is adjusted. The likelihood values returned from the fitter are plotted as points; the red curve is a quadratic fit to these points.

- $\alpha = 0.135 \pm 0.010$.

This method was also used to determine values of other parameters, notably the free parameter in the *BABAR* non-resonant model, given by equation (2.77), and the mass and width of the resonance labelled $(KK)_0^0$. Where results for such quantities are quoted in this document, both the central values and the uncertainties are estimated using the procedure described in this section. Where such values are quoted with asymmetric uncertainties, a quartic function was used in place of a quadratic function.

5.13 Resolution

This section describes an attempt at constructing a Dalitz plot fit that incorporates experimental resolution within the fitting routine itself. For reasons to be explained this method was not employed for the final fit, and no results reported outside this section make use of the fitting method detailed here.

5.13.1 Motivation for the Study of Resolution Effects

The main contribution to the inclusive $B^{\pm} \to K^{\pm}K^{\pm}K^{\mp}$ decay known before the analysis of the Dalitz plot for this mode, was that from $B^{\pm} \to \phi(1020)K^{\pm}$, $\phi \to K^{+}K^{-}$. This $\phi(1020)$ resonance has a width that is narrower than other resonances that had been studied using the `Laura++` framework in other charmless analyses. Following initial problems fitting to the $\phi(1020)$ resonance, resolution effects were studied, and a method of incorporating these effects into the fit was proposed.

It was subsequently found that the fit to the $\phi(1020)$ resonance was greatly improved as a consequence of the more sophisticated modelling of this resonance in the continuum background, as detailed in section 5.5. Studies showed that this resonance's shape was not in fact greatly affected by the experimental resolution, and so the default model was sufficient to return reliable results.

However this study also revealed that the resonance that was affected by the experimental resolution was the χ_{c0}. The methods tested to incorporate resolution into the fitting model did in fact improve the modelling of the χ_{c0} resonance.

This section will therefore concentrate on the effect of the alternative fitting regime tested on the χ_{c0} resonance, rather than the $\phi(1020)$ resonance, which was the initial motivation for this study.

5.13.2 Resolution Method

Method Overview

The method chosen to investigate the effects of resolution is based on a paper by D.M. Schmidt, R.J. Morrison, and M.S. Witherell entitled "A general method of estimating physical parameters from a distribution with acceptance and smearing effects" [67]. This paper presents a method for examining resolution effects, in cases where the effect can vary from a small effect up to a very large dominant effect, and so would be appropriate for use here where resolution effects are not expected to be a dominant factor. The method requires a large number of full MC events, and makes use of both the reconstructed information from the MC, as well as the MC truth information, that is the properties of the particles and the event that were generated by the MC package, before any simulation of detector resolution effects.

In addition to modelling resolution effects this method also takes into account "acceptance", which is analogous to the study of efficiency in this analysis. The result is that the efficiency histogram is not used in this method, and efficiency is incorporated into the fit via the fit values and a normalisation term.

The new fit method is achieved by formulating a modified version of `Laura++`, which calculates the value of the new likelihood defined in the next section, by using the default likelihood calculation of the unmodified `Laura++` package as input.

Method Details

This section details the way the method works, as described in the aforecited paper, with some items specific to this analysis replacing the more general terms from the paper.

Consider a distribution, $\Gamma(x, \mu)$, where both x and μ are multidimensional quantities representing a set of values — x represents physical quantities, which can be measured in the experiment, such as invariant masses, and μ represents parameters, which are to be determined from a maximum likelihood fit, such as magnitudes and

phases for resonant contributions.

When resolution effects are considered it is no longer possible to determine the underlying distribution $\Gamma(x, \mu)$, but rather a different distribution $F(\tilde{x}, \mu)$ is involved, where instead of x, the measured quantity is $\tilde{x}$, which is the physical value of x but smeared by the resolution effects.

It would then be possible to relate $F(\tilde{x}, \mu)$ to $\Gamma(x, \mu)$ via:

$$F(\tilde{x}, \mu) = A(\tilde{x}) \int S(\tilde{x}, x) \Gamma(x, \mu) dx \tag{5.20}$$

where $A(\tilde{x})$ and $S(\tilde{x}, x)$ are functions representing the acceptance and smearing effects respectively. These functions can be determined from MC study (as is done in the efficiency study described in section 5.8). However it can become very difficult and undesirable to attempt to parametrise the smearing effects in such a way, since the smearing function would depend on both the reconstructed and unreconstructed values. The method employed here adopts the alternative approach of using the MC events (which contain the smearing information) directly in the Likelihood fit.

The MC distribution should model $\Gamma(x, \mu)$ at the generator (truth information) level, and should model $F(\tilde{x}, \mu)$ in the observed/reconstructed events. A set of m MC events can be generated, and each individual event labelled y_j (to distinguish it from a data event x_i). Then the set of events $\{\tilde{y}_j, y_j\}$ can be recorded, so that the reconstructed MC values are associated with the truth information.

It is necessary to calculate a likelihood value for each data event in the fit, despite not forming an analytical construction for $F(\tilde{x}, \mu)$. To estimate this it is desirable to use a large sample size of MC events, and to have a small binning size if a histogram is to be formed. The function $\Gamma(x, \mu)$ can be factorised into two terms: $P(x)$ representing the phase space part, which can be flat, and $W(x, \mu)$, which is used to weight the events as described later.

The estimate is obtained by forming a small circular volume, V_i, centred around an event $\tilde{x}_i$ (the term volume is used here in line with the general terminology, despite the actual "volume" used being a 2-D area). All reconstructed MC events, $\tilde{y}_j$, that lie within this volume are established, and a weight is assigned to each MC event.

127
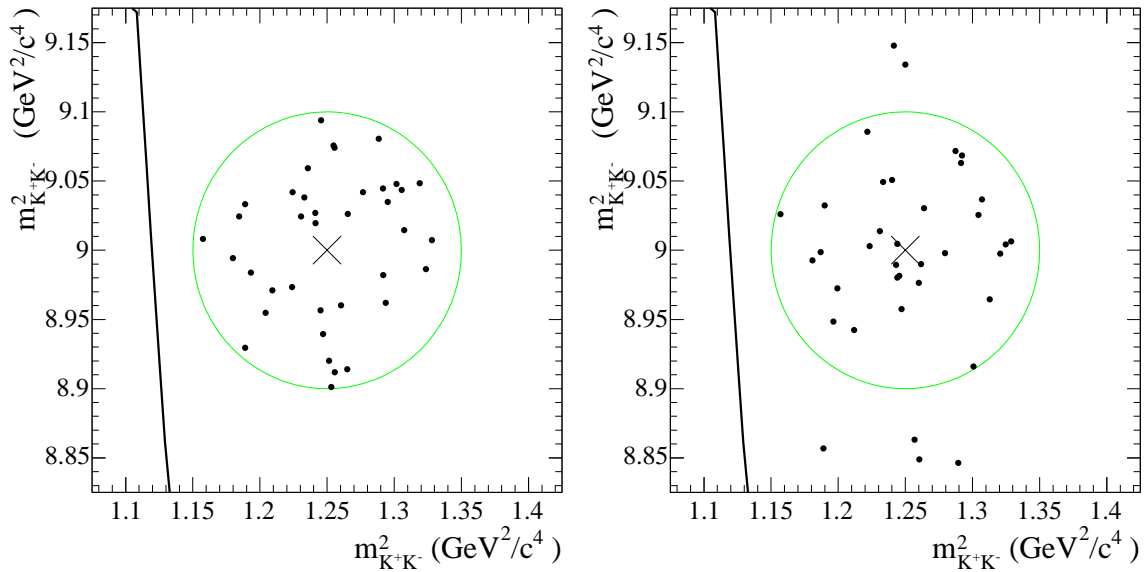
Figure 5.21: A volume V_i is shown as a green circle, centred around a data event shown as a cross. MC events are shown as solid points — on the left plotted at their reconstructed positions, and on the right at their MC truth positions. The black line is the Dalitz plot boundary.

An example of how a volume, V_i, is formed is shown in figure 5.21. The left-hand subfigure shows V_i as a green circle, centred on a data event shown by a cross. The points are the positions of all the MC events reconstructed within the volume. The righthand subfigure shows the same volume and data event. The points are the positions of the same MC events, but plotted by their MC truth information.

The weight $W(y_j, \mu)$ is calculated using the value of the MC data at the true position, rather than the reconstructed position, which is where the unfolding of the smearing information takes place. The sum of the weights of all the events reconstructed in V_i is then taken in the calculation of the likelihood. The form of $W(y_j, \mu)$ here is calculated using the Dalitz plot dynamics function that is used by the default `Laura++` package to formulate the unmodified likelihood (given by equation (5.1)).

Thus to calculate the likelihood of a set of n data events, $\{\tilde{x}_i\}$, using m MC events,

$\{\tilde{y}_j, y_j\}$, the following calculation is performed:

$$\ln \mathcal{L} = \sum_{i=1}^{n} \left(\frac{\sum_{\tilde{y}_j \ in \ V_i} W(y_j, \mu)}{C(\mu) V_i} \right) \tag{5.21}$$

where $C(\mu)$ is the normalisation condition:

$$C(\mu) = \sum_{j=1}^{m} W(y_j, \mu). \tag{5.22}$$

5.13.3   Phase Space Corrections

In making use of MC events to simulate smearing effects in this method it is assumed that the MC distribution is generated to be flat in phase space, which is true within the Dalitz plot kinematic boundary. However since no events were generated outside the Dalitz plot, this assumption breaks down for events lying close to the boundary, when the volume V_i intersects this boundary.

Where this is the case an allowance needs to be made, otherwise the likelihood for such events will be artificially low. Consider two similar events — one in which the volume around it lies wholly within the Dalitz plot, and one in which part of the volume lies outside the phase space boundary. If both events have similar kinematics and reconstruction efficiency, it would be expected that similar likelihood values would be obtained for each. However the likelihood term for the second event will be reduced in proportion to the fraction of the volume that lies outside the plot.

To address this issue two approaches were tested. The first approach was to calculate the size of the volume, V_i', lying within the kinematic boundary, and making the substitution $V_i \rightarrow V_i'$ in the denominator of the likelihood (equation 5.21).

The second approach was to increase the radius of the volume, such that the size of the new volume, V_i'' which is contained within the boundary, is equal to the default volume size — $V_i'' = V_i$. This has the advantage that a similar number of MC events are used for data events with similar efficiencies, ensuring that all these events have similar statistical significances. However this does result in some MC events further from the data event being included. Additionally this means that the event is no

longer central to the volume, but since part of the original volume is empty due to the boundary, the data event would effectively not have been central in any case.

Phase Space Correction Method

In order to make the correction to the volume to account for the reduction in phase space it is necessary to calculate the area contained within the Dalitz plot boundary.

The functional form of the Dalitz plot kinematic boundary is given by equations (2.61) and (2.62), for the lower and upper boundaries respectively, as for every value of the abscissa, there are two ordinate values.

To test whether the volume intersects the boundary, the boundary values are calculated at either edge of the volume, i.e. at the central abscissa $\pm$ the volume radius. This is done for both the upper and lower boundaries, but the following description refers to just one boundary.

It is possible to approximate the boundaries locally as a straight line. This is demonstated in figure 5.22. The two vertical straight lines lie at the values of the volume edges, defined in the previous paragraph. The values of the Dalitz plot boundary at these points are calculated, and joined by a straight line, which is shown in red in the figure. The volume is shown as a green circle, and the black line is the Dalitz plot boundary. The size of the volume here is far larger than would be used in practice, in order to allow the curvature to be seen. For a practical volume size no difference between the boundary and a straight line can be detected by eye.

The intersection between the straight line and the volume can then be found, if any. When no intersections are found the volume is adjudged to be wholly within the Dalitz plot, and no correction is required. Note that as all events lie within the Dalitz plot, the Dalitz plot boundary will always be convex as demonstrated in the figure, so this is a sufficient condition for rejecting events that need no correction.

If an intersection between the straight line and the volume is found then this can be used as an initial estimate of the intersection between the volume and the boundary. The calculated abscissa of each intersection with the straight line is used to calculate
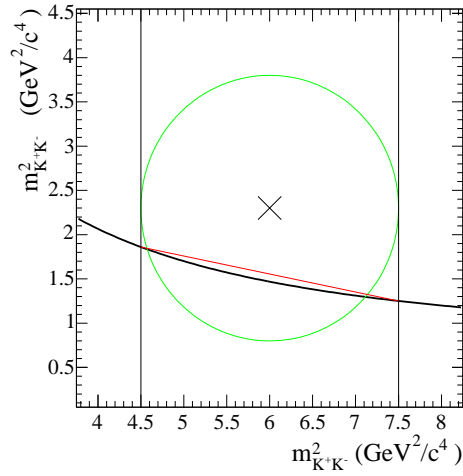
Figure 5.22: The Dalitz plot boundary (curved black line) can be approximated as a straight line (solid red line), by calculating the boundary value at the edges of the volume (green circle with edges shown as two vertical black lines), and joining these points.

the value of the ordinate on the boundary at this point. The value of the abscissa is then calculated on the circular edge of the volume, for this same ordinate. This new abscissa is used to calculate a new ordinate lying on the kinematic boundary, and the process can be iterated, until the positions of the calculated points both on the boundary and on the circle match to within a given tolerance.

Once the intersection has been found, the boundary can again be approximated as a straight line, and the area of the circle cut out by this straight line can be calculated from simple geometry. The area lying between this straight line and the Dalitz plot boundary is then evaluated using a Simpson's rule calculation, and added as a correction to give the final value for the area of the volume lying within the Dalitz plot.

In order to implement the second "$V_i'' = V_i$" method mentioned above, the volume radius is incremented, by multiplying by the square root of the quotient between the desired and obtained areas. This process is then iterated until the quotient is equal to

131
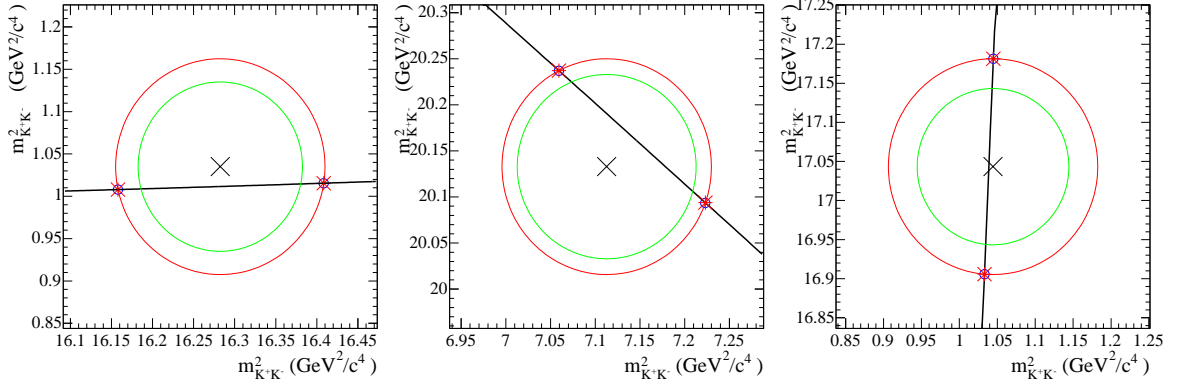
Figure 5.23: Example events with volumes formed around each event. The Dalitz plot boundary is shown, with intersections with the volume indicated. The area of the red circle within the Dalitz plot boundary is equal to the total area of the green circle.

one, to within a given tolerance.

This is demonstrated in figure 5.23, which shows some sample events, together with the volume constructed around them, the Dalitz plot boundary, and the calculated intersections. The green circles represent the default size of the volume, V_i, and the red circles represent the volume, V_i'', required to obtain the default area contained within the kinematic boundary.

5.13.4 Example of Use — Toy MC Generation

To demonstrate this method, the modified `Laura++` package is used to generate some toy MC events. Since the main resonance affected by the resolution is the χ_{c0}, the plots focus on this resonance. As a comparison, the same resonance is generated using the unmodified `Laura++` package, and additionally a full MC sample of $B^\pm \to \chi_{c0} K^\pm$, $\chi_{c0} \to K^+ K^-$ is used.

Figure 5.24 shows the invariant mass projections of the Dalitz plot in the region around the χ_{c0} mass. Subfigure a) shows toy MC events generated by the unmodified `Laura++` package; subfigure b) shows toy MC events generated by `Laura++` utilising the smearing method detailed in this section; and subfigure c) shows the full MC
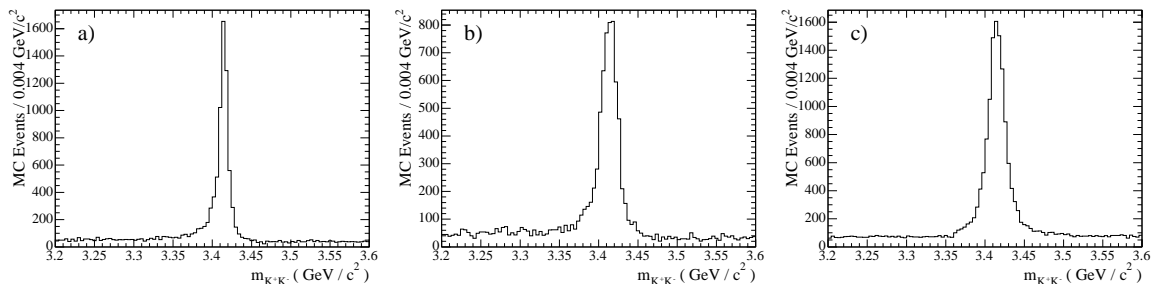
Figure 5.24: Three MC samples representing the χ_{c0} resonance — a) toy MC events generated by unmodified `Laura++`; b) toy MC events generated by the modified `Laura++`; c) Full MC events.

sample. Each of the plots contains a flat non-resonant component.

The width of the χ_{c0} in the full MC sample is greater than the natural width of this resonance. The default `Laura++` program only models the natural width — however the modified version of `Laura++` successfully models the increased width. There are some slight differences between the full MC and modified `Laura++` resonance shapes — the peak in the toy MC is slightly less sharply peaked than that in the full MC; and the tails show a slight difference, but the overall widths are very similar.

5.13.5   Resolution Method Conclusions

This method was successful in being able to model the resolution smearing of the χ_{c0} resonance. However, this method was not used in the final analysis for a number of reasons. Firstly the χ_{c0} resonance was not a major contribution to the $B^{\pm} \to K^{\pm}K^{\pm}K^{\mp}$ mode, and so in the final results it is included as only an upper limit.

Secondly the analysis requires a large amount of toy MC generation, in order to determine fit biases and systematic uncertainties, for example. Each of these toy MC studies takes a long time to generate. This modified smearing method introduces many extra calculations for each event. It can take up to a thousand times longer to generate the MC events required than using the unmodified `Laura++` package. As a result this method was found to be too computationally expensive to be used for a full analysis.

133

Chapter 6

Results

6.1 Component Model

The decay $B^{\pm} \to K^{\pm}K^{\pm}K^{\mp}$ can proceed via intermediate resonant particles. The only charmless resonance known a priori in the analysis was the $\phi(1020)$. By conducting a Dalitz plot analysis contributions from any other resonances could be sought. To best fit the data, a signal model was established consisting of resonant components that showed a significant impact in improving the likelihood fit.

To determine a signal model, established charmless resonances that can decay to two charged Kaons were considered. These included:

- $\phi(1020)$, $f_0(980)$, $f_0(1500)$, $f_2'(1525)$, $f_2(1270)$, $\phi(1680)$, $\phi_3(1850)$, $f_0(1710)$.

In addition there are a number of charmed resonances that can contribute, two of note are:

- χ_{c0}, $\overline{D}^0$.

The χ_{c0} has a width that is comparable with the widths of some charmless resonances, and was thus included in the signal model as an interfering component, with the chosen charmless resonances. Other charmed or charmonium resonances are considered in the background model, detailed in section 5.6.

In common with other charmless analyses the decays of D mesons are vetoed in the Dalitz plot. The width of the $\overline{D}^0$ is such that it is entirely dominated by experimental resolution, and thus no interference could be observed if it were to be included.

The initial signal model included the $\phi(1020)$, χ_{c0}, and a non-resonant $B^\pm \to K^\pm K^\pm K^\mp$ component. To this model extra resonances were added, and those that significantly improved the fit likelihood were retained, to form an improved model.

The final signal model consisted of 6 components, as follows:

- $B^\pm \to K^\pm K^\pm K^\mp$ (non-resonant),

- $B^\pm \to \phi(1020)K^\pm$,

- $B^\pm \to \chi_{c0}K^\pm$,

- $B^\pm \to f_0(980)K^\pm$,

- $B^\pm \to \phi(1680)K^\pm$,

- A scalar resonance of mass, $m \sim 1.5\,\mathrm{GeV}/c^2$.

The significance of each of these components can be seen by the detrimental effect on the likelihood fit, when they are not included. This is shown by omission tests (section 6.4). The $\phi(1680)$ is the least significant of the signal model resonances. Motivation for its inclusion is given in section 6.1.1. The effect upon the fit of resonances not included in the signal model is presented in addition tests (section 6.5).

The non-resonant component was modelled as uniform in phase space in the initial tests. Fits were also carried out using Belle's experimentally motivated non-resonant model, equation (2.76), and the model suggested within BABAR, equation (2.77). These each have a single free parameter, which was fitted using the scanning technique described in section 5.12. The distribution of each is shown in Figure 6.1 — each plot shows MC generated using the respective parametrisation, using the parameter value that best fits the data as input to the generation.
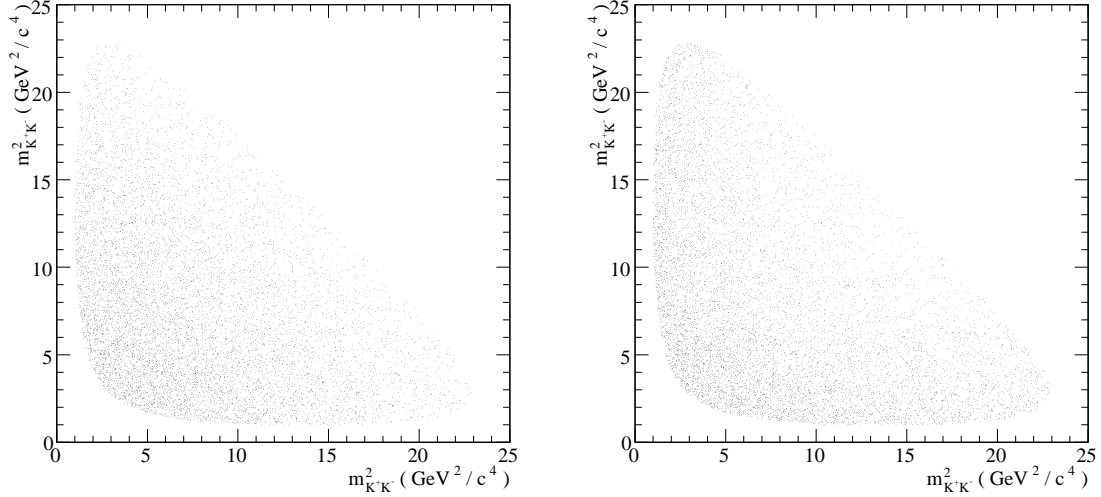
Figure 6.1: The distribution of non-resonant events, using MC generated from the "*BABAR*" and "Belle" models, shown on the left hand side, and right hand side, respectively.

Both models attempt to model the non-resonant amplitude decreasing slightly at higher invariant masses. These models give very significantly better results when used in place of a uniform phase space component. The "*BABAR*" model gave a better likelihood value, and more stable fit results (fewer multiple solutions, and more convergent fits). This model was chosen over the Belle model, and in all results shown in this thesis the non-resonant component is modelled using the *BABAR* model. The value estimated from the likelihood scan is:

- $\alpha = -0.799^{+0.038}_{-0.034}$.

The $f_0(980)$ is a resonance that was seen in the *BABAR* analysis of $B^\pm \to K^\pm \pi^\pm \pi^\mp$ [28], in which its decay to two charged pions is observed. It does also decay to two kaons, despite being below threshold for this process. For this reason it is modelled using a Flatté distribution, as described in section 2.9.3.

6.1.1 Resonant Structure at $\sim 1.5\,\mathrm{GeV}/c^2$

The resonant structure at $\sim 1.5\,\mathrm{GeV}/c^2$ was initially fitted as the $f_0(1500)$ resonance. This resonance was not included in the final signal model for several reasons.

The $f_0(1500)$ decays to two pions with a branching fraction approximately four times that to two kaons [1]. It would be expected that any signal for this resonance in $B^\pm \to K^\pm K^\pm K^\mp$ would imply that this resonance would also be seen in the decay $B^\pm \to K^\pm \pi^\pm \pi^\mp$, however no evidence of this resonance is seen in the BABAR analysis of this mode [28].

Other analyses of $B^\pm \to K^\pm K^\pm K^\mp$ (discussed fully in section 7.2) have also seen this resonant structure, and have not identified it with the $f_0(1500)$. Instead the mass and width of the resonance are fitted as free parameters. Assignment of this resonance as the $a_0(1450)$ is excluded by comparisons with the mode $B^\pm \to K^\pm K^\mp K^0_S$, as described in section 7.2.

The spin of the resonance was investigated by looking at the angular distribution of the events across the band in the Dalitz plot. If the resonance were spin 0, the angular distribution would be flat. Higher spins lead to more complex structures as given in section 2.8. The helicity distribution for events with invariant mass $1.3 < m_{K^+K^-} < 1.7\,\mathrm{GeV}/c^2$ is consistent with being flat, though it is possible that there could be a linear dependence - this would be the case if there were interference between a spin 0 resonance and a spin 1 resonance. This partly motivates the inclusion of the $\phi(1680)$ resonance in the fit.

The approach adopted is to fit the resonant structure as a scalar resonance, and to fit the mass and the width using the parameter scanning technique outlined in section 5.12. The values of these parameters are estimated to be:

- mass $= (1.523^{+0.028}_{-0.020})\,\mathrm{GeV}/c^2$,

- width $= (175^{+32}_{-27})\,\mathrm{MeV}/c^2$.

In this document this scalar resonance is referred to as $(KK)^0_0$.

6.2 Multiple Solutions for the $B^\pm \to K^\pm K^\pm K^\mp$ Data Samples

When fitting the events in the $B^\pm \to K^\pm K^\pm K^\mp$ Dalitz plot multiple solutions were observed. The most important feature was that a set of solutions only slightly worse in likelihood value gave very different results in terms of the physical parameters.

There were two particular resonance components that were affected by multiple solutions. Firstly the χ_{c0} — in this case two distinct values were seen for the magnitude/fit fraction, however both solutions were relatively small as was expected for this resonance.

The second resonance that would display multiple solutions was the $(KK)^0_0$. In this case the difference between the two solutions was large. Because constructive and destructive interference can occur in a Dalitz plot then it cannot be assumed that the total of the fit fractions for all the individual components will sum to 100%.

One of the solutions gave a total fit fraction of around 100%, whereas the other gave a fit fraction in the region of 150% to 200%. The favoured solution in terms of better likelihood was always the one which gave the lower fit fraction, however the likelihood difference between the two solution regimes was not significant enough definitively to exclude the higher fraction regime.

It can also be noted that where a scalar resonance interferes with a flat scalar component (non-resonant), then it can be shown that there exist degenerate solutions with different magnitudes and phases [41]. For a vector resonance (or higher) this degeneracy is lifted.

In tables 6.1 and 6.2 the leading solutions from fitting to the B^+ and B^- data sets, respectively, are shown. It can be noted that both multiple solution regimes described above are seen in each of the charge separated data sets.

The lower fraction solutions are the favoured solutions for both data sets, and it is these that are primarily used in this analysis, and quoted in the summary tables in section 7.1. Further discussion of separation of multiple solutions with an enhanced

Table 6.1: Summary of leading solutions when fitting to the B^+ sample.

Parameter	B^+ Solution 1	B^+ Solution 2	B^+ Solution 3
-log(Likelihood)	5193.8	5195.2	5200.6
Fraction of total fits (%)	30	19	10
NR Mag	1.0 (FIXED)	1.0 (FIXED)	1.0 (FIXED)
NR Phase	0.0 (FIXED)	0.0 (FIXED)	0.0 (FIXED)
NR Fraction (%)	56.63 ± 3.52	51.89 ± 5.58	62.11 ± 9.98
χ_{c0} Mag	0.32 ± 0.04	0.24 ± 0.05	0.21 ± 0.05
χ_{c0} Phase	0.58 ± 0.21	-0.35 ± 0.33	-0.75 ± 0.31
χ_{c0} Fraction (%)	5.87 ± 1.37	3.11 ± 1.21	2.62 ± 1.22
$\phi(1020)$ Mag	0.44 ± 0.04	0.47 ± 0.06	0.42 ± 0.04
$\phi(1020)$ Phase	-3.02 ± 0.25	-2.96 ± 0.46	-2.82 ± 0.32
$\phi(1020)$ Fraction (%)	11.08 ± 2.07	11.38 ± 2.76	11.04 ± 2.70
$f_0(980)$ Mag	0.67 ± 0.08	0.65 ± 0.15	0.70 ± 0.09
$f_0(980)$ Phase	2.14 ± 0.23	2.28 ± 0.41	2.34 ± 0.24
$f_0(980)$ Fraction (%)	25.04 ± 4.88	21.64 ± 7.92	30.75 ± 8.04
$(KK)_0^0$ Mag	0.44 ± 0.05	0.42 ± 0.05	1.12 ± 0.09
$(KK)_0^0$ Phase	-0.84 ± 0.19	-0.83 ± 0.26	0.65 ± 0.14
$(KK)_0^0$ Fraction (%)	10.73 ± 2.22	9.09 ± 2.19	77.22 ± 14.62
$\phi(1680)$ Mag	0.12 ± 0.05	0.12 ± 0.05	0.02 ± 0.07
$\phi(1680)$ Phase	-0.25 ± 0.52	-0.29 ± 0.50	-0.02 ± 3.49
$\phi(1680)$ Fraction (%)	0.78 ± 0.66	0.69 ± 0.62	0.03 ± 0.19
Total Fraction (%)	110.1	97.8	183.8

data set is also included in section 7.4.

139

Table 6.2: Summary of leading solutions when fitting to the B^- sample.

Parameter	B^- Solution 1	B^- Solution 2	B^- Solution 3	B^- Solution 4
-log(Likelihood)	4910.7	4913.0	4914.3	4914.3
Fraction of total fits (%)	31	17	2	5
NR Mag	1.0 (FIXED)	1.0 (FIXED)	1.0 (FIXED)	1.0 (FIXED)
NR Phase	0.0 (FIXED)	0.0 (FIXED)	0.0 (FIXED)	0.0 (FIXED)
NR Fraction (%)	52.52 ± 3.69	50.96 ± 3.35	86.78 ± 9.17	52.76 ± 9.12
χ_{c0} Mag	0.25 ± 0.04	0.36 ± 0.05	0.18 ± 0.03	0.34 ± 0.04
χ_{c0} Phase	-0.56 ± 0.26	0.65 ± 0.22	-1.00 ± 0.51	0.53 ± 0.20
χ_{c0} Fraction (%)	3.35 ± 1.06	6.72 ± 1.67	2.87 ± 0.92	6.25 ± 1.81
$\phi(1020)$ Mag	0.50 ± 0.05	0.51 ± 0.05	0.38 ± 0.04	0.50 ± 0.05
$\phi(1020)$ Phase	2.88 ± 0.23	3.06 ± 0.25	-0.03 ± 0.29	-2.60 ± 0.33
$\phi(1020)$ Fraction (%)	12.95 ± 2.48	13.08 ± 2.52	12.45 ± 2.38	13.10 ± 3.28
$f_0(980)$ Mag	0.74 ± 0.07	0.69 ± 0.08	0.42 ± 0.06	0.68 ± 0.10
$f_0(980)$ Phase	1.88 ± 0.19	2.03 ± 0.23	0.12 ± 0.22	2.49 ± 0.29
$f_0(980)$ Fraction (%)	28.92 ± 4.95	24.01 ± 4.80	15.24 ± 4.92	24.19 ± 7.31
$(KK)^0_0$ Mag	0.41 ± 0.05	0.41 ± 0.05	0.79 ± 0.07	1.20 ± 0.10
$(KK)^0_0$ Phase	-1.48 ± 0.23	-1.28 ± 0.23	1.54 ± 0.13	0.81 ± 0.16
$(KK)^0_0$ Fraction (%)	8.87 ± 1.88	8.41 ± 1.85	54.02 ± 7.04	76.17 ± 15.29
$\phi(1680)$ Mag	0.21 ± 0.05	0.22 ± 0.05	0.11 ± 0.04	0.16 ± 0.06
$\phi(1680)$ Phase	-1.19 ± 0.30	-1.12 ± 0.29	2.93 ± 0.53	1.63 ± 0.51
$\phi(1680)$ Fraction (%)	2.28 ± 0.99	2.49 ± 1.05	1.11 ± 0.81	1.40 ± 1.12
Total Fraction (%)	108.9	105.7	172.5	173.9

6.3 Fit Results

The multiple solution results presented in the previous section show that for both the B^+ and B^- samples the two leading solutions are very similar for all parameters,

except for the phase and fraction of the χ_{c0} resonance. The two different χ_{c0} solutions match up well between the two data samples. The solution with the lower fit fraction is designated as χ_{c0} solution A, and the higher fit fraction solution is designated as χ_{c0} solution B. For all other parameters the mean value of each parameter between the two fits is taken. These results are given in Table 6.3.

The table also includes the average efficiency across the Dalitz plot. This is calculated during the fit, and is weighted by the position of events within the plot:

$$\bar{\varepsilon} = \frac{\int \int_{DP} |\sum_j a_j g_j(x,y)|^2 \varepsilon(x,y) dx dy}{\int \int_{DP} |\sum_j a_j g_j(x,y)|^2 dx dy}, \tag{6.1}$$

where the definition of terms is the same as that used in the likelihood equation (5.1).

Figure 6.2 shows the fit results in invariant mass projections. The output from the fits is used as input for toy MC generation. The MC events number ten times as many as the data events, in order to reduce statistical fluctuations. This MC is used to show the fit result in the figure, where it is shown as a solid blue line. The data events are shown as black points. The red and black histograms show the amount of continuum and B-related backgrounds, respectively. The plots on the left hand side show the B^+ sample, and those on the right hand side show the B^- sample. The top two plots show the projection for the lower mass K^+K^- invariant mass combination, while the middle plots show the projection of the higher mass K^+K^- invariant mass combination. The bottom two plots show the projection of the like-signed kaon invariant mass.

Table 6.3: The mean fit results for the two most likely solutions in the B^+ and B^- samples. The two χ_{c0} results are shown, but the total fraction uses the mean χ_{c0} fraction. The first uncertainty is statistical, the second is systematic, calculated using the methods given in sections 6.6.1 and 6.7 respectively.

Component	B^+ Fit	B^- Fit
NR Fraction (%)	$54.3 \pm 9.5 \pm 3.0$	$51.7 \pm 9.0 \pm 4.1$
NR Phase	0.0 (FIXED)	0.0 (FIXED)
$\phi(1020)$ Fraction (%)	$11.2 \pm 1.4 \pm 0.43$	$13.0 \pm 1.7 \pm 0.43$
$\phi(1020)$ Phase	$-2.99 \pm 0.46 \pm 0.11$	$2.97 \pm 0.25 \pm 0.13$
$f_0(980)$ Fraction (%)	$23.3 \pm 8.7 \pm 3.8$	$26.5 \pm 7.7 \pm 3.8$
$f_0(980)$ Phase	$2.21 \pm 0.41 \pm 0.12$	$1.96 \pm 0.23 \pm 0.15$
$(KK)_0^0$ Fraction (%)	$9.9 \pm 3.0 \pm 1.8$	$8.6 \pm 2.5 \pm 1.8$
$(KK)_0^0$ Phase	$-0.84 \pm 0.19 \pm 0.09$	$-1.38 \pm 0.23 \pm 0.20$
χ_{c0} A Fraction (%)	$3.1 \pm 0.92 \pm 0.55$	$3.4 \pm 0.77 \pm 0.14$
χ_{c0} A Phase	$-0.35 \pm 0.33 \pm 0.21$	$-0.56 \pm 0.26 \pm 0.04$
χ_{c0} B Fraction (%)	$5.9 \pm 1.2 \pm 0.64$	$6.7 \pm 1.3 \pm 0.34$
χ_{c0} B Phase	$0.58 \pm 0.21 \pm 0.21$	$0.65 \pm 0.22 \pm 0.06$
χ_{c0} Mean Fraction (%)	$4.5 \pm 1.2 \pm 0.64$	$5.0 \pm 1.3 \pm 0.34$
$\phi(1680)$ Fraction	$0.74 \pm 0.83 \pm 2.1$	$2.4 \pm 1.2 \pm 0.34$
$\phi(1680)$ Phase	$-0.27 \pm 0.52 \pm 1.0$	$-1.16 \pm 0.30 \pm 0.23$
Total Fraction (%)	104.0	107.3
Average Efficiency (%)	$19.17 \pm 0.40 \pm 0.08$	$19.02 \pm 0.33 \pm 0.11$
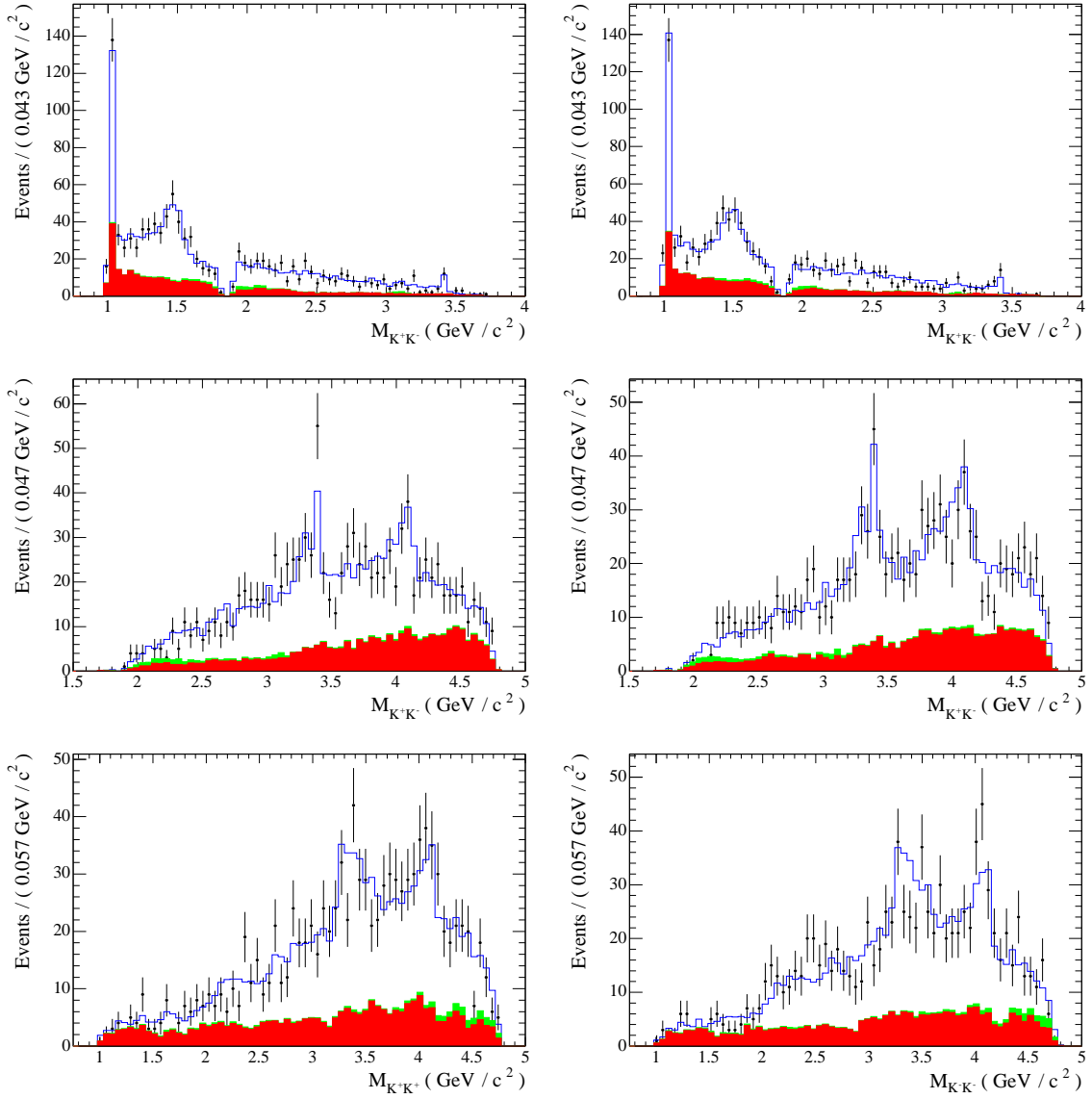
Figure 6.2: Invariant mass projection plots, showing the fit results (obtained from high statistics toy MC sample) as a solid blue line, data as black points, continuum background as a red histogram, and B-related background as a green histogram. The left hand plots are for the B^+ sample, and the right hand plots are for the B^- sample. The top plots show the lower mass K^+K^- mass combination, the middle plots show the higher mass K^+K^- mass combination, and the bottom plots show the like-signed kaon mass combination.

6.4 Omission Tests

To determine which components to include in the signal model (described in section 6.1), the data sets were fitted using different resonant contributions. Where the fit was significantly improved by including a resonance, in comparison to exactly the same fit but omitting this resonance, then the resonance was included in the model. Adding additional resonances increases the number of free parameters in the fit by two, and thus will lead to a slight improvement in the fit, as measured by the change in the $-\ln\mathcal{L}$ value for the fit. Major resonant contributions will lead to a much larger change in $-\ln\mathcal{L}$, however. The following tests demonstrate how the omission of the resonances in the signal model can lead to a deleterious effect on the fit.

Tables 6.4 and 6.5 show the results of omitting each of the chosen components in turn from the signal model, including the change in $-\ln\mathcal{L}$ for the fit. Because one magnitude and one phase have to be kept fixed during the fit, when the non-resonant component is omitted, the $\phi(1020)$ parameters are fixed instead.

The removal of the non-resonant component has the most significant detrimental effect on the fit. This component is also affected by the omission of other fit components (with the exception of the $\phi(1680)$) — as the non-resonant distribution overlaps every other component in the plot it follows that it would be sensitive to the presence of these other components.

The $\phi(1020)$ is a very distinct feature on the Dalitz plot, and occupies a very narrow band. As such its parameters are quite stable to the removal of other components. When it is removed, there is no other resonance that can model its sharp peak, but the fitter attempts to use the $f_0(980)$ to model this.

6.5   Addition Tests

These tests are carried out using a similar method to that used for the omission tests. In these tests the full signal model is used, with the addition of one resonance in turn, that was considered as a potential signal component. The addition of these resonances produces a slight improvement in the $-\ln\mathcal{L}$ value for the fit, due to the increase in the number of available fit parameters, but none of them produces the large difference in $-\ln\mathcal{L}$ seen in the omission tests for the major signal components.

The resonances that were included in these tests were the $f_2(1270)$, $f_2'(1525)$, and the $f_0(1710)$. The $\phi_3(1850)$ was not included as it lies within the D veto region. The $f_0(1370)$ is not well established in terms of its properties; its mass is quoted as 1200 to 1500 MeV/c^2, and its width is given as 200 to 500 MeV/c^2 [1]. Since the nominal signal model includes a scalar resonance, in the region of 1500 MeV/c^2, for which the mass and width are fitted rather than taken from established values, no advantage was gained in adding this resonance to the model. Some further comments on the $f_0(1370)$ can be found in section 7.2.

The results of including the additional resonances in the fit are shown in table 6.6 for the B^+ sample, and in table 6.7 for the B^- sample. These resonances do not give a compelling improvement to the fit, and they do not have a significant effect on the nominal resonances.

For each of these additional resonances tested an upper limit on its branching fraction is determined, as detailed in section 6.8.

Table 6.4: Omission test results for the fit to the B^+ sample. (All errors are statistical only and come from the `Minuit` fit.)

	Nominal	No Non-resonant	No χ_{c0}	No $\phi(1020)$	No $f_0(980)$	No $(KK)_0^0$	No $\phi(1680)$
$-\ln\mathcal{L} + \ln\mathcal{L}(\text{Nominal})$	0	135.5	25.5	77.3	15.5	31.5	2.5
Non-resonant Fraction (%)	54.25 ± 5.70	—	69.79 ± 4.77	70.20 ± 7.75	80.86 ± 2.79	33.09 ± 6.40	52.49 ± 5.28
Non-resonant Magnitude	1.00 FIXED	—	1.00 FIXED	1.00 FIXED	1.00 FIXED	1.00 FIXED	1.00 FIXED
Non-resonant Phase	0.00 FIXED	—	0.00 FIXED	0.00 FIXED	0.00 FIXED	0.00 FIXED	0.00 FIXED
χ_{c0} Fraction (%)	4.49 ± 1.37	5.78 ± 1.46	—	4.37 ± 1.61	4.64 ± 1.08	4.46 ± 1.67	4.53 ± 1.37
χ_{c0} Magnitude	0.28 ± 0.05	0.36 ± 0.04	—	0.25 ± 0.04	0.24 ± 0.03	0.37 ± 0.06	0.29 ± 0.05
χ_{c0} Phase	$+0.12 \pm 0.33$	$+1.26 \pm 0.29$	—	-0.13 ± 0.58	$+0.45 \pm 0.67$	$+0.24 \pm 0.36$	$+0.14 \pm 0.32$
$\phi(1020)$ Fraction (%)	11.23 ± 2.82	9.86 ± 1.29	11.38 ± 2.12	—	13.48 ± 1.58	10.70 ± 2.61	11.46 ± 2.49
$\phi(1020)$ Magnitude	0.46 ± 0.06	0.46 FIXED	0.40 ± 0.04	—	0.41 ± 0.03	0.57 ± 0.05	0.47 ± 0.05
$\phi(1020)$ Phase	-2.99 ± 0.47	-2.99 FIXED	$+3.13 \pm 0.25$	—	-1.75 ± 0.14	-2.36 ± 0.33	-2.94 ± 0.39
$f_0(980)$ Fraction (%)	23.34 ± 8.09	49.85 ± 5.08	28.89 ± 5.63	64.75 ± 8.90	—	18.33 ± 5.05	21.52 ± 6.73
$f_0(980)$ Magnitude	0.66 ± 0.15	1.04 ± 0.09	0.64 ± 0.07	0.96 ± 0.06	—	0.75 ± 0.14	0.64 ± 0.14
$f_0(980)$ Phase	$+2.21 \pm 0.42$	$+1.32 \pm 0.16$	$+1.99 \pm 0.20$	$+1.62 \pm 0.15$	—	-3.02 ± 0.41	$+2.29 \pm 0.38$
$(KK)_0^0$ Fraction (%)	9.91 ± 2.21	13.93 ± 2.78	11.34 ± 2.39	11.53 ± 2.72	13.78 ± 2.24	—	9.35 ± 2.06
$(KK)_0^0$ Magnitude	0.43 ± 0.05	0.55 ± 0.06	0.40 ± 0.04	0.41 ± 0.05	0.42 ± 0.03	—	0.42 ± 0.05
$(KK)_0^0$ Phase	-0.84 ± 0.27	$+1.61 \pm 0.20$	-0.83 ± 0.18	-1.36 ± 0.22	-0.19 ± 0.13	—	-0.86 ± 0.23
$\phi(1680)$ Fraction (%)	0.74 ± 0.66	0.50 ± 0.57	0.67 ± 0.62	1.82 ± 1.06	0.60 ± 0.57	0.66 ± 0.59	—
$\phi(1680)$ Magnitude	0.12 ± 0.05	0.11 ± 0.06	0.10 ± 0.05	0.16 ± 0.05	0.09 ± 0.04	0.14 ± 0.06	—
$\phi(1680)$ Phase	-0.27 ± 0.52	0.55 ± 0.61	-0.30 ± 0.56	-1.16 ± 0.36	-0.04 ± 0.64	-0.76 ± 0.46	—

Table 6.5: Omission test results for the fit to the B^- sample. (All errors are statistical only and come from the `Minuit` fit).

	Nominal	No Non-resonant	No χ_{c0}	No $\phi(1020)$	No $f_0(980)$	No $(KK)_0^0$	No $\phi(1680)$
$-\ln\mathcal{L} + \ln\mathcal{L}(\text{Nominal})$	0	103.4	36.2	98.9	24.0	30.7	10.9
Non-resonant Fraction (%)	51.75 ± 3.69	—	64.79 ± 4.51	71.49 ± 9.26	70.75 ± 2.27	34.89 ± 4.12	46.28 ± 3.50
Non-resonant Magnitude	1.00 FIXED	—	1.00 FIXED	1.00 FIXED	1.00 FIXED	1.00 FIXED	1.00 FIXED
Non-resonant Phase	0.00 FIXED	—	0.00 FIXED	0.00 FIXED	0.00 FIXED	0.00 FIXED	0.00 FIXED
χ_{c0} Fraction (%)	5.04 ± 1.67	5.54 ± 1.38	—	4.89 ± 1.82	5.18 ± 1.26	5.06 ± 1.63	5.01 ± 1.71
χ_{c0} Magnitude	0.31 ± 0.05	0.36 ± 0.04	—	0.26 ± 0.04	0.27 ± 0.03	0.38 ± 0.05	0.33 ± 0.05
χ_{c0} Phase	$+0.05 \pm 0.27$	$+0.52 \pm 0.30$	—	-0.22 ± 0.27	$+0.48 \pm 0.30$	$+0.11 \pm 0.29$	$+0.03 \pm 0.27$
$\phi(1020)$ Fraction (%)	13.02 ± 2.52	11.49 ± 1.35	13.05 ± 2.34	—	15.80 ± 1.75	12.38 ± 2.35	13.83 ± 2.58
$\phi(1020)$ Magnitude	0.51 ± 0.05	0.51 FIXED	0.45 ± 0.04	—	0.48 ± 0.03	0.60 ± 0.05	0.55 ± 0.05
$\phi(1020)$ Phase	$+2.97 \pm 0.25$	+2.97 FIXED	$+2.85 \pm 0.22$	—	-2.01 ± 0.14	-2.88 ± 0.26	$+3.00 \pm 0.24$
$f_0(980)$ Fraction (%)	26.47 ± 4.96	43.79 ± 4.74	31.47 ± 5.22	72.61 ± 10.56	—	23.23 ± 4.12	24.53 ± 5.06
$f_0(980)$ Magnitude	0.72 ± 0.08	1.00 ± 0.08	0.70 ± 0.06	1.01 ± 0.06	—	0.82 ± 0.11	0.73 ± 0.10
$f_0(980)$ Phase	$+1.96 \pm 0.23$	-0.965 ± 0.17	$+1.80 \pm 0.17$	$+1.36 \pm 0.12$	—	$+2.74 \pm 0.28$	$+2.07 \pm 0.25$
$(KK)_0^0$ Fraction (%)	8.64 ± 1.88	17.48 ± 3.09	8.68 ± 1.87	10.13 ± 2.45	11.29 ± 1.92	—	8.57 ± 1.88
$(KK)_0^0$ Magnitude	0.41 ± 0.05	0.63 ± 0.06	0.37 ± 0.04	0.38 ± 0.05	0.40 ± 0.04	—	0.43 ± 0.05
$(KK)_0^0$ Phase	-1.38 ± 0.23	$+1.16 \pm 0.20$	-1.40 ± 0.22	-2.09 ± 0.27	-0.53 ± 0.15	—	-1.47 ± 0.26
$\phi(1680)$ Fraction (%)	2.39 ± 1.05	1.75 ± 1.04	2.26 ± 0.97	4.54 ± 1.63	2.22 ± 1.07	2.68 ± 1.13	—
$\phi(1680)$ Magnitude	0.22 ± 0.05	0.20 ± 0.05	0.19 ± 0.04	0.26 ± 0.04	0.18 ± 0.04	0.28 ± 0.06	—
$\phi(1680)$ Phase	-1.16 ± 0.30	-0.48 ± 0.40	-1.22 ± 0.30	-1.86 ± 0.23	-0.59 ± 0.32	-1.23 ± 0.28	—

Table 6.6: Addition test results for the fit to the B^+ sample. (All errors are statistical only and come from the `Minuit` fit).

	Nominal	Add $f_2(1270)$	Add $f_2'(1525)$	Add $f_0(1710)$
$-\ln\mathcal{L} + \ln\mathcal{L}(\text{Nominal})$	0	-0.2	-1.1	-5.0
Non-resonant Fraction (%)	54.25 ± 5.70	52.98 ± 5.43	53.39 ± 5.63	53.76 ± 5.31
Non-resonant Magnitude	1.00 FIXED	1.00 FIXED	1.00 FIXED	1.00 FIXED
Non-resonant Phase	0.00 FIXED	0.00 FIXED	0.00 FIXED	0.00 FIXED
χ_{c0} Fraction (%)	4.49 ± 1.37	4.52 ± 1.40	4.54 ± 1.39	4.54 ± 1.47
χ_{c0} Magnitude	0.28 ± 0.05	0.29 ± 0.05	0.29 ± 0.05	0.29 ± 0.05
χ_{c0} Phase	$+0.12 \pm 0.33$	$+0.12 \pm 0.33$	$+0.14 \pm 0.33$	$+0.09 \pm 0.36$
$\phi(1020)$ Fraction (%)	11.23 ± 2.82	11.29 ± 2.65	11.34 ± 2.64	11.17 ± 2.64
$\phi(1020)$ Magnitude	0.46 ± 0.06	0.47 ± 0.05	0.47 ± 0.05	0.46 ± 0.05
$\phi(1020)$ Phase	-2.99 ± 0.47	-2.94 ± 0.44	-2.93 ± 0.44	-3.00 ± 0.36
$f_0(980)$ Fraction (%)	23.34 ± 8.09	22.24 ± 7.14	22.14 ± 7.32	24.53 ± 6.32
$f_0(980)$ Magnitude	0.66 ± 0.15	0.65 ± 0.14	0.64 ± 0.15	0.68 ± 0.12
$f_0(980)$ Phase	$+2.21 \pm 0.42$	$+2.26 \pm 0.41$	$+2.27 \pm 0.41$	$+2.30 \pm 0.34$
$(KK)_0^0$ Fraction (%)	9.91 ± 2.21	9.72 ± 2.22	9.70 ± 2.34	8.34 ± 2.89
$(KK)_0^0$ Magnitude	0.43 ± 0.05	0.43 ± 0.05	0.43 ± 0.05	0.39 ± 0.07
$(KK)_0^0$ Phase	-0.84 ± 0.27	-0.83 ± 0.25	-0.78 ± 0.26	-0.83 ± 0.31
$\phi(1680)$ Fraction (%)	0.74 ± 0.66	0.75 ± 0.68	0.82 ± 0.72	2.80 ± 1.38
$\phi(1680)$ Magnitude	0.12 ± 0.05	0.12 ± 0.05	0.13 ± 0.05	0.23 ± 0.06
$\phi(1680)$ Phase	-0.27 ± 0.52	-0.23 ± 0.54	-0.16 ± 0.55	$+0.77 \pm 0.32$
Additional Fraction (%)	—	0.05 ± 0.28	0.13 ± 0.27	4.81 ± 2.80
Additional Magnitude	—	0.03 ± 0.07	0.05 ± 0.05	0.30 ± 0.08
Additional Phase	—	-0.42 ± 3.71	$+0.95 \pm 0.99$	$+1.31 \pm 0.28$

Table 6.7: Addition test results for the fit to the B^- sample. (All errors are statistical only and come from the `Minuit` fit).

	Nominal	Add $f_2(1270)$	Add $f_2'(1525)$	Add $f_0(1710)$
$-\ln\mathcal{L} + \ln\mathcal{L}(\text{Nominal})$	0	-2.7	-4.9	-1.5
Non-resonant Fraction (%)	51.75 ± 3.69	55.03 ± 4.10	48.82 ± 3.35	49.17 ± 5.17
Non-resonant Magnitude	1.00 FIXED	1.00 FIXED	1.00 FIXED	1.00 FIXED
Non-resonant Phase	0.00 FIXED	0.00 FIXED	0.00 FIXED	0.00 FIXED
χ_{c0} Fraction (%)	5.04 ± 1.67	5.03 ± 1.67	5.04 ± 1.71	5.08 ± 1.86
χ_{c0} Magnitude	0.31 ± 0.05	0.30 ± 0.04	0.32 ± 0.05	0.32 ± 0.05
χ_{c0} Phase	$+0.05 \pm 0.27$	$+0.05 \pm 0.27$	$+0.06 \pm 0.27$	$+0.04 \pm 0.27$
$\phi(1020)$ Fraction (%)	13.02 ± 2.52	12.90 ± 2.53	13.18 ± 2.56	13.03 ± 2.91
$\phi(1020)$ Magnitude	0.51 ± 0.05	0.49 ± 0.05	0.52 ± 0.05	0.52 ± 0.06
$\phi(1020)$ Phase	$+2.97 \pm 0.25$	$+2.91 \pm 0.25$	$+3.12 \pm 0.27$	$+3.04 \pm 0.24$
$f_0(980)$ Fraction (%)	26.47 ± 4.96	27.57 ± 5.08	23.34 ± 4.85	25.23 ± 5.35
$f_0(980)$ Magnitude	0.72 ± 0.08	0.71 ± 0.08	0.69 ± 0.09	0.72 ± 0.08
$f_0(980)$ Phase	$+1.96 \pm 0.23$	$+1.90 \pm 0.23$	$+2.07 \pm 0.27$	$+2.08 \pm 0.24$
$(KK)_0^0$ Fraction (%)	8.64 ± 1.88	9.03 ± 1.92	8.75 ± 1.91	7.08 ± 2.63
$(KK)_0^0$ Magnitude	0.41 ± 0.05	0.41 ± 0.05	0.42 ± 0.05	0.38 ± 0.08
$(KK)_0^0$ Phase	-1.38 ± 0.23	-1.37 ± 0.22	-1.23 ± 0.24	-1.56 ± 0.30
$\phi(1680)$ Fraction (%)	2.39 ± 1.05	2.32 ± 1.02	2.21 ± 1.04	2.45 ± 1.16
$\phi(1680)$ Magnitude	0.22 ± 0.05	0.21 ± 0.05	0.22 ± 0.05	0.22 ± 0.05
$\phi(1680)$ Phase	-1.16 ± 0.30	-1.19 ± 0.30	-0.93 ± 0.33	-1.12 ± 0.33
Additional Fraction (%)	—	0.34 ± 0.34	1.43 ± 1.01	1.10 ± 1.41
Additional Magnitude	—	0.08 ± 0.04	0.17 ± 0.06	0.15 ± 0.09
Additional Phase	—	-2.93 ± 1.18	-0.52 ± 0.29	$+0.98 \pm 0.53$

6.6   Fit Bias Study

To determine whether any potential biases exist in the reported fit results, a study was carried out using toy MC. The results from the fit to data were taken, and used as inputs to the MC generation function of the Laura++ package. The generated MC was then fitted in the same manner as used to fit the data. This was repeated on multiple toy MC samples, each containing a number of events equalling that in the data sample. The fit results were then combined to form a distribution for each of the parameters included in the fit.

A "pull" value, ζ_p^i for is defined as:

$$\zeta_p^i = \frac{\mu_g^i - \mu_f^i}{\sigma_f^i} \tag{6.2}$$

where μ_g^i is the generator value used for parameter i, μ_f^i is the fitted value of the same parameter, and σ_f^i is the fitter's uncertainty on the parameter.

If there is no fit bias present then the distribution of pull values for each contribution/parameter should follow a Gaussian distribution with mean 0 and standard deviation 1.

The pull distributions for the parameters included in the fit are summarised in table 6.8 for MC based on both the B^+ and the B^- samples.

It can be seen that some of the magnitudes and phases do show some deviation from the expected Gaussian distribution. This was investigated, and was attributed to the effect of the $f_0(980)$ in the fit, as smaller deviations were observed when tests were carried out omitting this resonance. Other fitting scenarios were tested, for example: using a greater number of events or using more toy experiments, but no significant reduction in fit biases was observed.

Ideally all possible fit biases should be eliminated, but where this is not possible, then their effects are included as a systematic uncertainty. The difference between the generated and fitted values of a parameter is incorporated into the systematic uncertainty quoted for that parameter in the final results.

Table 6.8: Magnitude and Phase pulls from toy MC generated from the best fit.

	B^+		B^-	
	Pull mean	Pull width	Pull mean	Pull width
$f_0(980)$ Magnitude	0.249 ± 0.053	1.069 ± 0.046	0.235 ± 0.047	0.926 ± 0.039
$f_0(980)$ Phase	-0.263 ± 0.059	1.134 ± 0.052	-0.299 ± 0.045	1.014 ± 0.032
$\phi(1020)$ Magnitude	-0.155 ± 0.050	1.007 ± 0.040	-0.147 ± 0.052	1.007 ± 0.045
$\phi(1020)$ Phase	-0.293 ± 0.047	1.061 ± 0.034	-0.178 ± 0.045	1.002 ± 0.031
$(KK)_0^0$ Magnitude	0.119 ± 0.044	0.974 ± 0.031	0.167 ± 0.043	0.956 ± 0.030
$(KK)_0^0$ Phase	-0.005 ± 0.051	1.015 ± 0.047	-0.022 ± 0.044	0.974 ± 0.031
$\phi(1680)$ Magnitude	0.262 ± 0.040	0.879 ± 0.028	0.091 ± 0.045	0.996 ± 0.032
$\phi(1680)$ Phase	-0.098 ± 0.051	1.034 ± 0.048	-0.110 ± 0.046	1.030 ± 0.030
χ_{c0} Magnitude	-0.225 ± 0.050	0.996 ± 0.049	0.043 ± 0.046	1.016 ± 0.032
χ_{c0} Phase	-0.096 ± 0.047	1.051 ± 0.033	-0.023 ± 0.046	1.010 ± 0.030

6.6.1 Statistical Uncertainty

The uncertainty on the fit outputs from `Minuit` may not be a reliable source for the statistical uncertainties on these parameters, due to fit biases, multiple solutions, and other factors. Instead samples of toy MC events are generated, with inputs based on the results from the fits to data. For each fit parameter, the distribution from fitting to the toy MC samples is produced, and the width of the distribution is taken as the statistical uncertainty on that parameter. This technique has been used in previous analyses using the `Laura++` framework.

Tables 6.9 and 6.10 include the means and widths for parameters of the B^+ and B^- samples respectively.

6.7 Systematic Uncertainties

To estimate the systematic uncertainties on the fit results, a number of possible sources are investigated. In this section the systematic uncertainties associated with the his-

Table 6.9: B^+ Fit fraction means and widths from toy MC study using the nominal fit results.

	B^+ Best Fit		B^+ 2nd Best Fit	
	Mean	Width	Mean	Width
Non-resonant Fit Fraction (%)	58.09 ± 0.49	9.54 ± 0.44	53.70 ± 0.42	8.22 ± 0.40
$f_0(980)$ Fit Fraction (%)	27.93 ± 0.41	8.07 ± 0.41	24.39 ± 0.45	8.64 ± 0.44
$\phi(1020)$ Fit Fraction (%)	10.773 ± 0.074	1.437 ± 0.068	11.183 ± 0.072	1.401 ± 0.070
$(KK)_0^0$ Fit Fraction (%)	11.48 ± 0.15	3.01 ± 0.13	9.93 ± 0.15	2.85 ± 0.13
$\phi(1680)$ Fit Fraction (%)	0.924 ± 0.040	0.679 ± 0.053	0.687 ± 0.082	0.827 ± 0.081
χ_{c0} Fit Fraction (%)	5.532 ± 0.065	1.235 ± 0.062	3.116 ± 0.052	0.923 ± 0.053

Table 6.10: B^- Fit Fraction means and widths from toy MC study using the nominal fit results.

	B^- Best Fit		B^- 2nd Best Fit	
	Mean	Width	Mean	Width
Non-resonant Fit Fraction (%)	52.25 ± 0.47	8.61 ± 0.51	52.26 ± 0.46	9.04 ± 0.45
$f_0(980)$ Fit Fraction (%)	30.01 ± 0.40	7.38 ± 0.37	26.78 ± 0.40	7.65 ± 0.41
$\phi(1020)$ Fit Fraction (%)	12.757 ± 0.093	1.691 ± 0.086	13.025 ± 0.068	1.349 ± 0.068
$(KK)_0^0$ Fit Fraction (%)	8.87 ± 0.12	2.15 ± 0.12	9.71 ± 0.14	2.48 ± 0.14
$\phi(1680)$ Fit Fraction (%)	2.557 ± 0.062	1.160 ± 0.053	2.784 ± 0.062	1.171 ± 0.057
χ_{c0} Fit Fraction (%)	3.372 ± 0.039	0.765 ± 0.039	6.406 ± 0.064	1.262 ± 0.065

tograms and the calculated background fractions are studied. Five systematics associated with the fit inputs are studied here:

- the use of the efficiency histogram;

- the use of the continuum background histogram;

- the use of the $B\overline{B}$ background histogram;

- the calculated fraction of continuum background;

- the calculated fraction of $B\overline{B}$ background;

To investigate the systematic uncertainties associated with using histograms in the likelihood fit an approach is adopted in which the fit is performed multiple times with different possible histograms. For each variant histogram the value in each bin is fluctuated within the Gaussian uncertainty of that bin. A set of 100 variant histograms is produced for each of the histogram systematics studied, and each is fitted as for the nominal fit. These 100 results are combined to produce a distribution in fit fractions and phases. The systematic uncertainty on each of these parameters is assigned as the root mean square (RMS) of its distribution.

For the background fraction uncertainties the procedure is very similar. The fraction is fluctuated within its Gaussian uncertainty, and fits carried out using 100 different fractions. The RMS of the obtained distributions are again assigned as systematic uncertainties.

Table 6.11 shows the values obtained for the systematic uncertainties for each of the fit fractions and phases in the fit. Also shown is the systematic uncertainty on the average efficiency returned by the fit — these values are used in the determination of the uncertainty of the inclusive branching fraction in section 6.10.3. The table is divided into double columns — the left hand column displays the obtained RMS values using the B^+ sample, and the right hand column displays the RMS values from using the B^- sample.

The first double column gives the RMS value for each sample when the efficiency histogram is fluctuated, the second double column gives this information for the fluctuation of the continuum background histogram, and the third double column for the fluctuation of the fraction of continuum background. The fourth and fifth double columns report the RMS values for the fluctuation of the B related background histogram, and the B-related background fraction respectively.

There are an additional two sources of uncertainty that were also considered. These were the fit bias, and model dependency. For the fit bias, the uncertainty is taken to

be the difference between the value of a parameter in the nominal fit, and the mean value for that parameter obtained in the fit bias tests of section 6.6. The uncertainty due the model dependence is calculated based on the observed values from fits where an extra resonance is added, as described in section 6.5. The uncertainty is taken to be the largest deviation from the nominal value for each parameter. The uncertainties calculated from each of these sources are shown in Table 6.12.

Table 6.11: Systematic uncertainties from the amplitude fit.

Uncertainty Source	ε histogram		$q\bar{q}$ histogram		$q\bar{q}$ fraction		$B\bar{B}$ histogram		$B\bar{B}$ fraction		Total	
Data Sample	B^+	B^-	B^+	B^-	B^+	B^-	B^+	B^-	B^+	B^-	B^+	B^-
Non resonant fit fraction (%)	0.314	0.610	2.020	0.632	0.336	0.934	0.291	0.380	0.281	0.283	2.111	1.367
Non resonant phase	Fixed	Fixed	Fixed	Fixed	Fixed	Fixed	Fixed	Fixed	Fixed	Fixed	Fixed	Fixed
χ_{c0} fit fraction	0.043	0.048	0.540	0.036	0.021	0.030	0.024	0.041	0.035	0.014	0.544	0.080
χ_{c0} phase	0.011	0.007	0.204	0.010	0.003	0.004	0.014	0.010	0.003	0.003	0.205	0.017
$\phi(1020)$ fit fraction	0.279	0.244	0.150	0.192	0.018	0.008	0.044	0.213	0.052	0.031	0.325	0.378
$\phi(1020)$ phase	0.016	0.015	0.076	0.013	0.005	0.012	0.013	0.018	0.010	0.007	0.080	0.030
$f_0(980)$ fit fraction	0.550	0.497	1.993	0.524	0.032	0.346	0.387	0.477	0.336	0.221	2.133	0.958
$f_0(980)$ phase	0.010	0.013	0.061	0.018	0.005	0.019	0.011	0.011	0.009	0.008	0.064	0.032
$(KK)_0^0$ fit fraction	0.163	0.247	0.517	0.209	0.052	0.237	0.091	0.102	0.117	0.198	0.564	0.459
$(KK)_0^0$ phase	0.012	0.012	0.064	0.017	0.003	0.004	0.020	0.013	0.003	0.004	0.068	0.025
$\phi(1680)$ fit fraction	0.057	0.042	0.224	0.035	0.010	0.017	0.074	0.033	0.059	0.021	0.250	0.069
$\phi(1680)$ phase	0.016	0.022	0.070	0.025	0.004	0.017	0.033	0.020	0.006	0.002	0.079	0.042
Average efficiency	0.062	0.063	0.017	0.020	0.000	0.001	0.007	0.005	0.007	0.007	0.065	0.067

Table 6.12: Systematic uncertainties from the amplitude fit. The sub-total includes the fit bias and model dependency. The total includes these, and the histogram and fraction fluctuations.

Uncertainty Source	Fit bias		Model dependence		Sub-total		Total	
Data Sample	B^+	B^-	B^+	B^-	B^+	B^-	B^+	B^-
Non resonant fit fraction	1.635	0.785	1.280	3.745	2.076	3.826	2.961	4.063
Non resonant phase	Fixed	Fixed	Fixed	Fixed	Fixed	Fixed	Fixed	Fixed
χ_{c0} fit fraction	0.172	0.168	0.100	0.036	0.199	0.172	0.573	0.211
χ_{c0} phase	0.015	0.027	0.040	0.010	0.043	0.029	0.208	0.053
$\phi(1020)$ fit fraction	0.252	0.124	0.110	0.160	0.275	0.202	0.425	0.429
$\phi(1020)$ phase	0.053	0.049	0.076	0.115	0.093	0.125	0.133	0.128
$f_0(980)$ fit fraction	2.820	1.930	1.430	3.130	3.162	3.677	3.814	3.800
$f_0(980)$ phase	0.047	0.037	0.130	0.018	0.138	0.041	0.120	0.139
$(KK)^0_0$ fit fraction	0.795	0.650	1.570	1.560	1.760	1.690	1.848	1.751
$(KK)^0_0$ phase	0.007	0.012	0.060	0.195	0.060	0.195	0.091	0.197
$\phi(1680)$ fit fraction	0.074	0.286	2.060	0.175	2.061	0.335	2.076	0.342
$\phi(1680)$ phase	0.020	0.041	1.035	0.225	1.035	0.229	1.038	0.233
Average efficiency	0.010	0.020	0.045	0.080	0.046	0.082	0.080	0.106

6.8   Upper Limits

The χ_{c0} and $\phi(1680)$ are the least significant components of the nominal signal model, and together with the resonances that were included in the addition tests (section 6.5) upper limits are calculated on the fit fraction of each resonance.

Upper Limits can be calculated using the form of the Likelihood equation:

$$\frac{\int_0^{x_{ul}} \mathcal{L}dx}{\int_0^\infty \mathcal{L}dx} = 0.90, \tag{6.3}$$

where x is a parameter, and x_{ul} is the upper limit on this parameter. The 0.90 indicates that the upper limit would be at a 90% confidence level. This formula does not take into account systematic uncertainties however.

In order to incorporate the systematic effects into the upper limit, a Monte Carlo simulation is used instead. A total of 100 MC samples are generated for each resonance for which an upper limit is to be determined. The input parameters used for the MC simulation are the magnitudes and phases obtained from the addition tests for each of the additional resonances, and from the main fit for the two resonances that were included in the signal model.

In each sample the background and efficiency systematic effects (namely the efficiency histogram, the continuum background histogram, the continuum background fraction, the $B\overline{B}$ background histogram, and the $B\overline{B}$ background fraction) are fluctuated. This is performed in the same manner as used in the systematic uncertainty determination (section 6.7), except that all five sources are fluctuated for each and every MC sample, rather than studying each in turn. Fit bias is not included as an additional component, as it will already be present in the fit. Model dependency is included as including these extra resonances is the source of this uncertainty.

The generated MC is fitted in the standard manner used in this analysis, and the results are combined to form parameter and $-\ln\mathcal{L}$ distributions. The fit results are subjected to a cut on the $-\ln\mathcal{L}$ distribution, such that the least likely 10% of the fits are removed. Of the remaining 90% of the fit results, the highest fit fraction for each

resonance is taken to be its fit fraction upper limit at 90% confidence level.

For each of the resonances, this test is performed using the values from both the B^+ and the B^- samples. When an overall upper limit is shown in the summary tables, the higher of the two values obtained is used. Table 6.13 shows the upper limits for each of the resonances investigated.

Table 6.13: 90% confidence level fit fraction upper limits.

	B^- Sample	B^+ Sample
χ_{c0} Fit Fraction (%)	7.8	8.2
$\phi(1680)$ Fit Fraction (%)	4.2	3.8
$f_2'(1525)$ Fit Fraction (%)	2.8	3.2
$f_2(1270)$ Fit Fraction (%)	6.7	2.5
$f_0(1710)$ Fit Fraction (%)	6.0	9.5

6.9 CP Asymmetries

The CP asymmetry, A_{CP}, is defined by equation 2.25. It gives a measure of the amount of direct CP violation in a decay, corresponding to a difference in the decay rates for the two CP conjugate decay modes, $B^+ \to K^+K^+K^-$ and $B^- \to K^-K^-K^+$.

Values of A_{CP} are determined for the four most significant contributions to the signal model. Due to the large uncertainties on the fractions of the two other contributions, it would not be possible to exclude any significant range of possible A_{CP}, and thus they are not treated here.

To determine the values of A_{CP} for each resonance, the fit results for that resonance in the B^+ and B^- samples are taken together with the uncertainty on the fit results. To determine the uncertainty on each A_{CP} value, the error on each of the B^+ and B^- values are combined with the partial derivatives of equation 2.25 with respect to A_f and $\bar{A}_{\bar{f}}$ to give the combined uncertainty on A_{CP}. This method is performed separately for

the statistical and systematic uncertainties. Sources of systematic uncertainties which are common to both samples, such as the efficiency histogram, are not considered in this calculation.

The asymmetry on the inclusive branching fraction for $B^\pm \to K^\pm K^\pm K^\mp$ is obtained in a similar fashion, using the signal yields in the B^+ and B^- samples. The five asymmetry values calculated are given in table 6.14.

Table 6.14: Calculated values of the A_{CP} parameter. The first uncertainty is statistical, and the second is systematic.

Mode	A_{CP} (%)
$B^\pm \to K^\pm K^\pm K^\mp$ inclusive	$0.0 \pm 3.0 \pm 4.2$
$B^\pm \to K^\pm K^\pm K^\mp$ non-resonant	$-2.2 \pm 12 \pm 4.9$
$B^\pm \to \phi(1020)K^\pm;\ \phi(1020) \to K^+K^-$	$5.4 \pm 7.9 \pm 3.7$
$B^\pm \to f_0(980)K^\pm;\ f_0(980) \to K^+K^-$	$6.4 \pm 21 \pm 11$
$B \to (KK)_0^0 K^\pm;\ (KK)_0^0 \to K^+K^-$	$11 \pm 18 \pm 10$

The results show no significant asymmetries for any of the modes studied, all lying within one standard deviation of the hypothesis $A_{CP} = 0$, which corresponds to no direct CP violation.

6.10   Inclusive Branching Fraction

The inclusive branching fraction is obtained from the following formula:

$$\mathcal{B}(B^\pm \to K^\pm K^\pm K^\mp) = \frac{N_{sig}}{\bar{\varepsilon}\varepsilon_c N_{B\bar{B}}} \qquad (6.4)$$

where N_{sig} is the number of signal events, $N_{B\bar{B}}$ is the total number of events containing a $B\bar{B}$ pair recorded by BABAR, $\bar{\varepsilon}$ is the weighted efficiency returned by the Dalitz

plot fit, and ε_c is the efficiency correction, that takes into account the difference in reconstruction efficiencies between data and Monte Carlo samples.

The total inclusive branching fraction is calculated to be $\mathcal{B}(B^\pm \to K^\pm K^\pm K^\mp) = 35.1 \times 10^{-6}$. To determine the systematic uncertainty on this value, the uncertainties attributed to each of the quantities in equation 6.4 are investigated in sections 6.10.1 to 6.10.4. The total calculated uncertainty is given in Table 6.16.

6.10.1   Uncertainty on $N_{B\bar{B}}$

The number of events containing a $B\bar{B}$ pair is determined by a BABAR working group, and the uncertainty on this value is calculated to be 1.1% [47]. The number of $B\bar{B}$ pairs is calculated by studying the number of multihadronic events, and the number of dimuon events, in both on and off-resonance data. In off-resonance data, all multi-hadronic events arise from continuum (light quark etc.) events, whereas on-resonance data also have the contribution from B meson decays. The two numbers are scaled, so that they represent the same luminosity, and the difference between the two is used as the number of $B\bar{B}$ pairs. The luminosity is calculated from the number of dimuon events in each sample.

The assumption is made that 50% of the decays of the $\Upsilon(4S)$ are to B^+B^- pairs, and the other 50% are to $B^0\bar{B}^0$ pairs. Experimental measurements have not found any significant deviation from this ratio [68].

6.10.2   Uncertainty on N_{sig}

In order to determine the uncertainty on N_{sig} the fit to m_{ES} is repeated with the expected B-related background in the fit increased or decreased by 1σ, the standard deviation on this background which was determined when it was modelled (section 5.6).

The variation in the signal yield is seen to be approximately symmetric about the nominal value. From these results a systematic uncertainty of 0.2% is assigned to this

quantity.

6.10.3 Uncertainty on $\bar{\varepsilon}$

The uncertainty on the average weighted efficiency, $\bar{\varepsilon}$, is determined from three sources:

- Firstly there is the uncertainty from the Dalitz plot fit. This is calculated from toy MC studies, where samples are generated and fitted, and the weighted efficiencies from each experiment are collated. The RMS value of the efficiency distribution was found to be 0.5% for both the B^+ and B^- samples, which is taken as the systematic uncertainty.

- The variation in efficiency due to the uncertainty in the efficiency and background histograms, background fractions, fit bias, and model dependency was examined during the fluctuation tests detailed in section 6.7 — Tables 6.11 and 6.12 include the RMS values of the efficiency distributions in each of the tests. Summing these uncertainties gives a combined uncertainty of 0.4% for the B^+ sample, and 0.5% for the B^- sample. For both samples the dominant contribution to this uncertainty was the fluctuation of the efficiency histogram.

- The final contribution to this uncertainty arises from corrections to PID and tracking. The method follows that used in [64]. The tracking uncertainty follows a standard procedure outlined by the tracking task force [69] [70]. A systematic uncertainty of 0.8% is assigned per track, and these are added coherently to give a total tracking uncertainty of 2.4%. The PID correction is found to be 1% per track per selector applied. Since each track has 2 selectors applied (Kaon selector and electron selector), this gives an uncertainty of 1.4% per track. These are then added coherently to give a total PID uncertainty of 4.2%.

6.10.4 Uncertainty on ε_c

The variable ε_c represents a correction arising from the difference in reconstruction efficiency between experimental data and that observed in MC simulation. The mode

161

$B^+ \to \overline{D}^0 \pi^+$, where $\overline{D}^0 \to K^+ \pi^-$ is chosen to examine this because it has a branching fraction of $(1.89 \pm 0.12) \times 10^{-4}$, and is topologically and kinematically similar to the signal mode. The potentially more useful mode $B^+ \to \overline{D}^0 K^+$, with $\overline{D}^0 \to K^+ K^-$, which has an identical final state to the signal, has a branching fraction of only $(1.4 \pm 0.2) \times 10^{-6}$, and so there are insufficient events to allow control studies to be performed.

Two sets of events are used in this investigation. The first is the experimental data, which are only taken in a small invariant mass range centred on the $\overline{D}^0$ mass. This is not in the final form that is used for the main analysis, but is instead that obtained before applying the final selection cuts. The second set of events is full MC simulation for the mode $B^+ \to \overline{D}^0 \pi^+$, $\overline{D}^0 \to K^+ \pi^-$. For each of these sets of events, the `CharmlessFitter` package (described in section 4.7), is used to apply each of the final cuts on $\cos \theta_T$, the Fisher discriminant, m_{ES}, and ΔE, in turn, and the efficiency for each cut is determined. For the MC the fraction of events remaining after each cut is used to determine the efficiency. For the data, the cut is applied, and then the remaining events are subjected to a fit to the m_{ES} distribution to determine the signal yield arising from each cut — the ratio these signal yields, before and after the cut, is used to determine the efficiency.

Thus the efficiency is calculated in both data and MC, and the ratio of these efficiencies is used to obtain the data/MC efficiency correction for each cut. The results are listed in table 6.15, together with the overall correction, and the statistical uncertainties on these quantities, determined from combining the uncertainty on the number of events in each of the data and MC samples.

It should be noted that a separate fit is carried out to the data at each stage, and that the reported number is the signal yield from the fit, rather than the raw number of events after each cut. These fitted yields have an associated uncertainty, and so can fluctuate upwards after a cut. The most likely cause of this eventuality is when a cut removes a very small number of events of which the majority are background.

Table 6.15: Data/MC efficiency corrections.

Requirement	Data Before	Data After	Data Efficiency	MC Before	MC After	MC Efficiency	Correction	Uncertainty	Fractional Uncertainty
$\cos\theta_T$	14293	13206	0.924	76770	71435	0.931	0.992	0.013	0.013
Fisher	13206	10794	0.817	71435	59261	0.830	0.984	0.014	0.014
m_{ES}	10794	10814	1.001	59261	59252	1.000	1.001	0.015	0.015
ΔE	10814	10363	0.958	59252	57387	0.969	0.989	0.015	0.015
Total							0.965	0.029	0.030

Table 6.16: The total systematic uncertainty on the branching fraction.

Source of uncertainty	Uncertainty (%)
$N_{B\bar{B}}$	1.1
N_{sig}	0.2
$\bar{\varepsilon}$ (DP fit)	0.5
$\bar{\varepsilon}$ (histogram etc.)	0.5
$\bar{\varepsilon}$ (PID)	4.2
$\bar{\varepsilon}$ (Tracking)	2.4
ε_c	3.0
Total	5.8

Chapter 7

Conclusions and Summary

7.1 Summary of Results

A summary of the results obtained in this analysis is given here. For branching fractions and asymmetry measurements, the fit fractions reported in chapter 5 have been multiplied by the inclusive branching fraction to arrive at the exclusive branching fraction for each mode. The uncertainty on each of these exclusive measurements is obtained by combining the uncertainty on the fit fraction with the uncertainty on the inclusive branching fraction.

Table 7.1 reports the exclusive branching fractions and CP asymmetries of the four most prominent contributions to the Dalitz plot. It also includes the inclusive branching fraction for $B^{\pm} \to K^{\pm}K^{\pm}K^{\mp}$, and the calculated asymmetry for the whole Dalitz plot of this mode. Table 7.2 includes the calculated upper limits for the less significant resonances.

In addition to these results, three parameters were estimated using parameter scans, as described in section 5.12. These were the mass and width of the scalar resonance $(KK)_0^0$, and the free parameter, α in the non-resonant parametrisation of equation 2.77. The values determined were:

- $(KK)_0^0$ mass: $m = (1.523^{+0.028}_{-0.020})\,\mathrm{GeV}/c^2$.

- $(KK)_0^0$ width: $\Gamma = (175^{+32}_{-27})\,\mathrm{MeV}/c^2$.

- Non resonant: $\alpha = -0.799^{+0.038}_{-0.034}$.

Table 7.1: Summary of measurements of branching fractions (averaged over charge conjugate states) and CP asymmetries. The first error is statistical, and the second is systematic.

Mode	$\mathcal{B}$(Mode) (10^{-6})	A_{CP} (%)
$B^{\pm} \to K^{\pm}K^{\pm}K^{\mp}$ Total	$35.1 \pm 1.3 \pm 2.1$	$0.0 \pm 3.0 \pm 4.2$
$B^{\pm} \to K^{\pm}K^{\pm}K^{\mp}$ non–resonant	$18.6 \pm 3.4 \pm 1.8$	$-2.4 \pm 13 \pm 4.7$
$B^{\pm} \to \phi(1020)K^{\pm}, \phi(1020) \to K^+K^-$	$4.3 \pm 0.6 \pm 0.3$	$7.4 \pm 8.0 \pm 2.5$
$B^{\pm} \to f_0(980)K^{\pm}, f_0(980) \to K^+K^-$	$8.7 \pm 3.1 \pm 1.4$	$6.3 \pm 21 \pm 11$
$B^{\pm} \to (KK)_0^0 K^{\pm}, (KK)_0^0 \to K^+K^-$	$3.3 \pm 1.1 \pm 0.7$	$-6.8 \pm 25 \pm 14$

Table 7.2: Summary of measurements of central values and upper limits of branching fractions (averaged over charge conjugate states) for less significant components. The first error is statistical, and the second is systematic.

Mode	$\mathcal{B}$(Mode) (10^{-6})	90% CL Upper Limit (10^{-6})
$B^{\pm} \to \chi_{c0}K^{\pm}, \chi_{c0} \to K^+K^-$	$1.7 \pm 0.5 \pm 0.1$	< 2.9
$B^{\pm} \to \phi(1680)K^{\pm}, \phi(1680) \to K^+K^-$	$0.6 \pm 0.4 \pm 0.2$	< 1.5
$B^{\pm} \to f_2(1270)K^{\pm}, f_2(1270) \to K^+K^-$	$-$	< 1.1
$B^{\pm} \to f_2'(1525)K^{\pm}, f_2'(1525) \to K^+K^-$	$-$	< 2.4
$B^{\pm} \to f_0(1710)K^{\pm}, f_0(1710) \to K^+K^-$	$-$	< 3.3

7.2 Comparison of Results with other Analyses of $B^\pm \to K^\pm K^\pm K^\mp$

This section compares the results of this analysis with other analyses of $B^\pm \to K^\pm K^\pm K^\mp$, which have been carried out by both the *BABAR* and Belle collaborations.

7.2.1 *BABAR* Results

The *BABAR* paper [26] details an analysis which was carried out concurrently with and on the same dataset as the analysis reported in this document. This analysis was used as cross check on the published analysis.

The major difference in the analysis techniques is that the published analysis is a binned analysis, as opposed to an unbinned analysis in this thesis. That analysis also includes the $f_0(1710)$ in the signal model, and does not include the $\phi(1680)$; both of these resonances are minor contributions to the plot.

The results are largely consistent with the results of this document. The $(KK)_0^0$ (referred to as $X_0(1550)$) fraction is markedly different. This is due to the complications of multiple solutions as described in section 5.11. Both analyses observe multiple solutions for the $(KK)_0^0$ component fraction, one of which is of the order of 10% and the other a much higher value. However, while this analysis favours the lower solution, the published analysis favours the higher solution, though both observe the other solution, but with a lower likelihood in their respective fits. The mass and width of the $X_0(1500)$ are quoted as $m_{X_0} = 1.539 \pm 0.020\,\mathrm{GeV}/c^2$ and $\Gamma_{X_0} = 0.257 \pm 0.033\,\mathrm{GeV}/c^2$. The mass is consistent with that measured in this analysis, though the width is somewhat larger.

The total measured branching fraction (including the χ_{c0}) is $\mathcal{B}(B^\pm \to K^\pm K^\pm K^\mp) = (35.2 \pm 0.9 \pm 1.6) \times 10^{-6}$, which is in very good agreement with that measured in this analysis (section 6.10). Excluding the χ_{c0} to quote a purely charmless branching fraction gives $\mathcal{B}(B^\pm \to K^\pm K^\pm K^\mp) = (33.5 \pm 0.9 \pm 1.6) \times 10^{-6}$. Subtracting the χ_{c0} component from the inclusive branching fraction measured in this thesis gives

$\mathcal{B}(B^{\pm} \to K^{\pm}K^{\pm}K^{\mp}) = (33.4 \pm 1.3 \pm 2.1) \times 10^{-6}$, also in good agreement.

7.2.2 Belle Results

The Belle collaboration presented results for $B^{\pm} \to K^{\pm}K^{\pm}K^{\mp}$ [27] using $140\,\text{fb}^{-1}$ of data taken at a centre of mass energy corresponding to the $\Upsilon(4S)$ mass, and $8.3\,\text{fb}^{-1}$ of data taken off resonance. They have two fit regimes, these being $KKK - A_J$ and $KKK - B_J$, where J is the spin of the resonance observed at $\sim 1.5\,\text{GeV}/c^2$, which they call the $f_X(1500)$. The $KKK - A_J$ models do not include a non-resonant component, and are disfavoured compared to the $KKK - B_J$ models which do. The non-resonant component is not flat, but instead a number of parametrisations are tried; the chosen non-resonant parametrisation is discussed in section 2.9.4.

Different values of J are tested, but the favoured model is the $KKK - B_0$ model. This model contains multiple solutions of the type noted previously, measuring the $f_X(1500)$ fractions as $(63.4\pm6.9)\%$ (Solution 1) and $(8.21\pm1.94)\%$ (Solution 2). There is also the uncertainty in the χ_{c0} fraction, but it is a relatively minor contribution.

The mass and width of the $f_X(1500)$ are measured to be $m_{f_X} = (1.524 \pm 0.014)\,\text{GeV}/c^2$ or $(1.491 \pm 0.018)\,\text{GeV}/c^2$, and $\Gamma_{f_X} = (0.136 \pm 0.023)\,\text{GeV}/c^2$ or $(0.145 \pm 0.029)\,\text{GeV}/c^2$, where the two values correspond to the two solutions given above. The mass results are in agreement with that estimated in this thesis, and the width results are slightly lower.

Belle place an upper limit on $\mathcal{B}(B^{\pm} \to f_0(980)K^{\pm}, f_0(980) \to K^+K^-) < 2.9\times10^{-6}$. The Belle analysis uses measurements of the Flatté parametrisation from the E791 collaboration [71], which has a much lower coupling of the $f_0(980)$ to two kaons than the BES parameters used in this analysis, and thus a much lower branching fraction is expected. Different Flatté parametrisations are discussed in section 7.3.

The charmless branching fraction (not including χ_{c0}) is measured to be $(30.6 \pm 1.2 \pm 2.3) \times 10^{-6}$, which is slightly lower than that measured by the *BABAR* Dalitz analyses.

7.2.3 Comparison of $B^\pm \to \phi(1020)K^\pm$ Results

The decay $B^\pm \to \phi(1020)K^\pm$ is the only charmless mode contributing to $B^\pm \to K^\pm K^\pm K^\mp$, that has been measured in quasi-two-body (non Dalitz plot) analyses. The PDG value for this mode is $\mathcal{B}(B^\pm \to \phi(1020)K^\pm) = (9.3\pm1.0)\times10^{-6}$ [1], and also gives the branching fraction $\mathcal{B}(\phi(1020) \to K^+K^-) = (49.1 \pm 0.6)\%$. This thesis finds a branching fraction of $\mathcal{B}(B^\pm \to \phi(1020)K^\pm, \phi(1020) \to K^+K^-) = (4.3 \pm 0.6 \pm 0.3)\times10^{-6}$. The same branching fraction is calculated to be $(4.14\pm0.32\pm0.33)\times10^{-6}$ in the published $BABAR$ paper, and $(4.72 \pm 0.45 \pm 0.35^{+0.39}_{-0.22})\times10^{-6}$ in the Belle paper. The three sources of uncertainty given are: statistical, systematic, and model dependency. All of these branching fractions are in good agreement.

7.3 Conclusions and Discussion

This thesis documents the Dalitz plot analysis of the mode $B^\pm \to K^\pm K^\pm K^\mp$. The signal is modelled as six components, one of which is a non-resonant component, and the other five resonant components. Branching fractions are measured, with upper limits being placed on the two least significant components and also on three additional resonances.

The analysis is not able to unambiguously identify the resonant structure at $\sim 1.5\,\mathrm{GeV}/c^2$ in the K^+K^- spectrum. In line with similar analyses, the mass and width of this resonance are fitted, with reasonable agreement between analyses. Identifying this resonance as the $a_0(1450)$ is disfavoured by observations of the mode $B^0 \to K^+K^-K^0_S$ (section 2.6.4). The analysis of the mode $B^\pm \to K^\pm\pi^\pm\pi^\mp$ does not see a similar resonance in its $\pi^+\pi^-$ spectrum, which suggests that the resonance is not the $f_0(1500)$, as this resonance has a branching fraction to $\pi\pi$ that is approximately four times that to $K\overline{K}$ [1].

It is possible that the $f_0(1500)$ could interfere with other scalar resonances in such a way that a resonant structure is observed in $B^\pm \to K^\pm K^\pm K^\mp$, but not in

$B^\pm \to K^\pm \pi^\pm \pi^\mp$. Interference schemes involving light scalar glueballs have been suggested (section 2.7.1). Scalar resonances can be quite broad, and overlap with each other in invariant mass spectra, obfuscating each spectrum, and making identification of individual states experimentally challenging. The existence of some states (such as the σ or $f_0(600)$) remains controversial.

Some experiments, such as that described in section 2.7, have seen some evidence for a scalar state with approximately the same mass as the $f_2'(1525)$ in the $K\overline{K}$ mass spectrum. However such a state has never been well established.

Analyses with a greater quantity of data will be needed to reveal more information about this resonance, and perhaps confirm or exclude one of the above suggestions as to its nature.

The observation of the $f_0(980)$ also presents some questions. The nature of this resonance is unknown, with traditional quark model $q\overline{q}$ assignments suggested, as well as four quark $qq\overline{q}\overline{q}$, and $K\overline{K}$ molecule possibilities. Current predictions and experimental results are unable to distinguish between these possibilities (section 2.7.1).

The decay of $f_0(980)$ is modelled using the Flatté lineshape (section 2.9.3). This accounts for the coupled channel nature of the resonance. Because the mass is less than the threshold for creation of $K\overline{K}$, the $f_0(980)$ does not show a conventional resonant structure, but instead appears as only a "resonance tail".

The parameters of the Flatté distribution have been determined by other experiments, and have been tested in the mode $B^\pm \to K^\pm \pi^\pm \pi^\mp$ [28], as the $B^\pm \to K^\pm K^\pm K^\mp$ mode does not have enough data to discriminate significantly. The parameters from the BES collaboration have been adopted here and by other BABAR analyses, and have been recommended by the BABAR Dalitz Task Force [72]. The use of different Flatté parameters from other experiments leads to very different results, as can be noted from the comparison between BABAR and Belle results for this mode given in section 7.2. Assigning a model dependency systematic uncertainty to the $B^\pm \to f_0(980)K^\pm$, $f_0(980) \to K^+K^-$ branching fraction to account for this was not seen as useful, since such an uncertainty would be almost as large as the measurement itself.

The only meaningful comparisons that can be made are with other measurements that also use the BES parameters.

The non-resonant component is modelled by a simple parametrisation, involving only a single free parameter, in this and the other Dalitz analyses of $B^\pm \to K^\pm K^\pm K^\mp$. These analyses agree that the non-resonant component is not consistent with being distributed uniformly in phase space, instead they favour an increase in non-resonant contributions at lower invariant masses. Theoretical predictions of non-resonant distributions have been examined, such as [73] [74]. Some of these attempt to model the non-resonant component by taking into account the presence of virtual resonances outside the Dalitz plot, such as B^* mesons. Such models have an increase at higher invariant masses, and are not consistent with the observed experimental data.

Whatever the form of the non-resonant component, it will interfere with all resonant components of the Dalitz plot. It is difficult to separate scalar resonances from the non-resonant contribution, particularly given the interference between them. Unless the nature of scalar resonances present in $B^\pm \to K^\pm K^\pm K^\mp$ can be better established, the form of the non-resonant component of this mode will be subject to large uncertainties. Any comparison of its form with theoretical predictions is thus subject to these uncertainties.

7.4   Future Analyses

The `Laura++` package has been used in a number of analyses, including this one. New analyses are being undertaken using the same framework, incorporating supplementary features that allow more information to be obtained. The `Laura++` fitting routine will be able to fit both B^+ and B^- samples simultaneously. In analyses of neutral B decay modes, such as $B^0 \to \pi^+\pi^-K^0_s$, it is not possible to separate B^0 and $\overline{B}^0$ events, as is done for B^+ and B^- events, but instead the other B decay in the event must be used for flavour tagging. Thus a simultaneous time-dependent fit has to be performed

to extract CP information. This will mean that quantities such as A_{CP} will be a fit output, rather than being calculated from the results of the fits to two separate samples.

Incorporating extra variables, such as m_{ES}, into the combined fit would also provide a reduction in the systematic uncertainties due to the simultaneous extraction of signal and background yields. Self Cross Feed will also be incorporated as a separate component into fits. The fit may allow for the fitting of separate weak and strong phases (section 2.4) for each resonance, given sufficient data to separate them.

The *BABAR* experiment is continuing to take data, and has an objective of taking $1\mathrm{ab}^{-1}$ by the end of its running. Such a dataset would represent a four to five-fold increase on the quantity of data used in this analysis. The goals of an analysis using such a data sample would include establishing the resonant content of the Dalitz plot with more precision than was possible in this analysis. In addition to a decrease in the statistical uncertainty, the implementation of some of the extensions to the `Laura++` fitter detailed above, together with improved background modelling from the larger data sample, would reduce the systematic uncertainties upon the results.

In this analysis, model dependency is not fully incorporated as a systematic uncertainty. This is due to the doubt as to the composition of the signal model, and the nature of some of the resonances, and the non-resonant component. To include a model dependency uncertainty for these factors would lead to results that make no quantitative statement about the possible composition. Instead the results are presented for a particular model, which can be amended or improved upon in future analyses.

The mode $B^{\pm} \to K^{\pm}K^{\pm}K^{\mp}$ is observed to have a much higher non-resonant fraction than related $B \to hhh$ modes. With many more data, leading to an improved signal model, it may be possible to start testing theoretical predictions of the form of the non-resonant component, that cannot be tested in similar charmless analyses.

With an increased data set, a major goal would be to observe CP-violation in this mode. Combined with other experimental results, this could further constrain

the parameters of The Unitarity Triangle, and lead to a greater understanding of CP-violation within (and perhaps beyond) the Standard Model.

Appendix A

Glossary

AWG	Analysis Working Group
BABAR	A $B\overline{B}$ experiment
DAQ	Data Acquisition
DCH	Drift Chamber
DCT	Drift Chamber Trigger
DRC *or* DIRC	Detector of Internally Reflected Cherenkov radiation
DOCA	Distance Of Closest Approach
DQG	Data Quality Group
ER	Event Reconstruction
EMC	Electromagnetic Calorimeter
EMT	Electromagnetic Calorimeter Trigger
FCTS	Fast Control and Timing System
FEE	Front End Electronics
FSR	Final State Radiation
GLT	Global Level Trigger
HER	High Energy Ring
IFR	Instrumented Flux Return
IFT	Instrumented Flux Return Trigger

IR	Interaction Region
L1T	Level 1 Trigger
L3T	Level 3 Trigger
Linac	Linear Accelerator
LER	Low Energy Ring
LST	Limited Streamer Tube
MC	Monte Carlo
OPR	Online Prompt Reconstruction
PC	Prompt Calibration
PEP-II	Positron Electron Project II
PID	Particle Identification
PMT	PhotoMultiplier Tube
RPC	Resistive Plate Chamber
ROE	Rest Of Event
SCF	Self Cross Feed
SVT	Silicon Vertex Tracker
TLA	Three Letter Acronym
TOT	Time Over Threshold
θ_T	The thrust angle of an event

Bibliography

[1] S. Eidelman et al. Review of particle physics. *Phys. Lett.*, B592:1, 2004.

[2] S. Eidelman et al. Review of particle physics. *Phys. Lett.*, B592:37, 2004.

[3] P.W. Higgs. *Phys. Rev. Lett.*, 12:132, 1964.

[4] A.D. Sakharov. *Pisma Zh. Eksp. Teor. Fiz.*, 5:32, 1967.

[5] A. Riotto. Theories of baryogenesis. arXiv:hep-ph/9807454.

[6] C.S. Wu, E. Ambler, R.W. Hayward, D.D. Hoppes, and R.P. Hudson. *Phys. Rev.*, 105:1413–1414, 1957.

[7] J. S. Schwinger. *Proc. Nat. Acad. Sci.*, 44:223–228, 1958.

[8] J. H. Christenson, J. W. Cronin, V. L. Fitch, and R. Turlay. *Phys. Rev. Lett.*, 13:138–140, 1964.

[9] B. Aubert et al. *Phys. Rev. Lett.*, 87:091801, 2001.

[10] N. Cabibbo. *Phys. Rev. Lett.*, 10:531, 1963.

[11] M. Kobayashi and T. Maskawa. *Prog. Theor. Phys.*, 49:652–657, 1973.

[12] Ling-Lie Chau and Wai-Yee Keung. *Phys. Rev. Lett.*, 53:1802, 1984.

[13] L. Wolfenstein. *Phys. Rev. Lett.*, 51:1945, 1983.

[14] S. Eidelman et al. Review of particle physics. *Phys. Lett.*, B592:130, 2004. equation (11.2).

[15] J. Charles et al. *Eur. Phys. J.*, C41:1–131, 2005. Updated results and plots available at: http://ckmfitter.in2p3.fr.

[16] http://www.slac.stanford.edu/xorg/ckmfitter/plots_fpcp06/ rhoeta_withs2abgam.eps.gz.

[17] http://www.slac.stanford.edu/xorg/ckmfitter/plots_fpcp06/ rhoeta_withs2abgam_small.eps.gz.

[18] arXiv:hep-ex/0609040.

[19] http://www.slac.stanford.edu/xorg/hfag/.

[20] C. Jarlskog. *Phys. Rev. Lett.*, 55:1039, 1985.

[21] S. Eidelman et al. Review of particle physics. *Phys. Lett.*, B592:138, 2004.

[22] B. Aubert et al. *Phys. Rev. Lett.*, 91:051801, 2003.

[23] B. Aubert et al. *Phys. Rev. Lett.*, 87:151801, 2001.

[24] B. Aubert et al. *Phys. Rev.*, D69:011102, 2004.

[25] B. Aubert et al. *Phys. Rev.*, D69:071103, 2004.

[26] B. Aubert et al. *Phys. Rev.*, D74:032003, 2006.

[27] A. Garmash et al. *Phys. Rev.*, D71:092003, 2005.

[28] B. Aubert et al. *Phys. Rev.*, D72:072003, 2005.

[29] M. Ablikim et al. *Phys. Lett.*, B598:149–158, 2004.

[30] B. Aubert et al. 2006. arXiv:hep-ex/0607112.

[31] D. Aston et al. *Nucl. Phys.*, B301:525–553, 1988.

[32] A. Furman, R. Kamiński, L. Leśniak, and B. Loiseau. arXiv:hep-ph/0504116.

[33] Hai-Yang Cheng, Chun-Khiang Chua, and Kwei-Chou Yang. arXiv:hep-ph/0508104.

[34] P. Minkowski and W. Ochs. arXiv:hep-ph/0404194.

[35] S. Eidelman et al. Review of particle physics. *Phys. Lett.*, B592:299, 2004.

[36] C. Zemach. *Phys. Rev.*, 133:B1201, 1964.

[37] C. Zemach. *Phys. Rev.*, 140:B97, 1965.

[38] F. Halzen and D.M. Martin. *Quarks and Leptons.* John Wiley & Sons, 1984.

[39] J. Blatt and V. E. Weisskopf. *Theoretical Nuclear Physics.* J. Wiley (New York), 1952.

[40] S.M. Flatté. *Phys. Lett.*, B63:224, 1976.

[41] A. Dvoretskii. *BABAR* Analysis Document #643.

[42] http://www.slac.stanford.edu/history/highlights.shtml.

[43] http://www2.slac.stanford.edu/vvc/experiments/pep.html.

[44] P. F. Harrison and H. R. Quinn. Papers from Workshop on Physics at an Asymmetric B Factory (BaBar Collaboration Meeting), Rome, Italy, 11-14 Nov 1996, Princeton, NJ, 17-20 Mar 1997, Orsay, France, 16-19 Jun 1997 and Pasadena, CA, 22-24 Sep 1997.

[45] http://www.slac.stanford.edu/BFROOT/www/Detector/Operations/Operations.html.

[46] B. Aubert et al. *Nucl. Instrum. Meth.*, A479:1–116, 2002.

[47] C. Hearty. *BABAR* Analysis Document 134.

[48] http://www.slac.stanford.edu/BFROOT/www/Physics/Tools/generators/ EvtGen/EvtGen.html.

[49] D. J. Lange and A. Ryd. *BABAR* Analysis Document # 522.

[50] T. Sjostrand. *Comput. Phys. Commun*, 82:74, 1994.

[51] S. Agostinelli et al. *Nucl. Instrum. Meth.*, A506:250, 2003.

[52] M. Carpinelli and F. Martinez-Vidal. *BABAR* Analysis Document #102.

[53] http://www.slac.stanford.edu/BFROOT/www/Physics/Tools/Pid/pid.html.

[54] G. Mancinelli and S. Spanier. *BABAR* Analysis Document #116.

[55] http://www.slac.stanford.edu/BFROOT/www/Physics/Analysis/AWG/ chrmls_hadronic/ThreeBody/Software/NonCharm3BodyUser_cm2.html.

[56] http://root.cern.ch.

[57] http://babar-hn.slac.stanford.edu:5090/cgi-bin/internal/cvsweb.cgi/ CharmlessFitter/README.

[58] roofit.sourceforge.net/.

[59] http://www.slac.stanford.edu/BFROOT/www/Physics/Analysis/AWG/ chrmls_hadronic/ThreeBody/Software/Laura++/index.html.

[60] J.J. Back. *BABAR* Analysis Document #806.

[61] F. James and M. Roos. *Comput. Phys. Commun.*, 10:343–367, 1975.

[62] http://wwwasdoc.web.cern.ch/wwwasdoc/minuit/minmain.html.

[63] H. Albrecht et al. *Z. Phys.*, C48:543–552, 1990.

[64] J.J. Back. *BABAR* Analysis Document #303.

[65] W. M. Dunwoodie. http://www.slac.stanford.edu/ wmd/bbkinematics/.

[66] M. Pivk and F. R. Le Diberder. *Nucl. Instrum. Meth.*, A555:356–369, 2005.

[67] D. M. Schmidt, R. J. Morrison, and M. S. Witherell. *Nucl. Instrum. Meth.*, A328:547–552, 1993.

[68] B. Aubert et al. *Phys. Rev. Lett.*, 95:042001, 2005.

[69] http://www.slac.stanford.edu/www/Physics/TrackEfficTaskForce/ TrackingTaskForce.html.

[70] E. Varnes et al. *BABAR* Analysis document #157.

[71] E. M. Aitala et al. *Phys. Rev. Lett.*, 86:765–769, 2001.

[72] http://www.slac.stanford.edu/BFROOT/www/Physics/Analysis/AWG/ Charm/Dalitz2005/.

[73] B. Bajc, S. Fajfer, R. J. Oakes, T. N. Pham, and S. Prelovsek. *Phys. Lett.*, B447:313–320, 1999.

[74] D. V. Bugg. *Phys. Lett.*, B572:1–7, 2003.